The distribution of star formation rates during the assembly of NGC 1399 as deduced from its globular clusters

Christine Schulz

München 2017

The distribution of star formation rates during the assembly of NGC 1399 as deduced from its globular clusters

Christine Schulz

Dissertation
an der Fakultät für Physik
der Ludwig-Maximilians-Universität
München

vorgelegt von
Christine Schulz
aus Saran

München 2017

Erstgutachter: Prof. Dr. Andreas Burkert
Zweitgutachter: PD Dr. Markus Kissler-Patig
Datum der Abgabe: 17. August 2017
Datum der mündlichen Prüfung: 26. Oktober 2017

Table of Contents

Table of Contents vi

List of Figures vii

List of Tables ix

Zusammenfassung xi

Abstract xiii

1 Introduction 1
- 1.1 Star clusters and their formation . . . 1
- 1.2 Ultra-compact dwarf galaxies . . . 4
- 1.3 NGC 1399 in the center of the Fornax cluster and its rich globular cluster system . . . 7
- 1.4 Aim of the present thesis . . . 13
- 1.5 Outline of the present thesis . . . 18

2 Underlying framework 19
- 2.1 Improving optimal sampling . . . 19
- 2.2 Embedded cluster mass function (ECMF) . . . 24
- 2.3 The concept of the integrated galactic embedded cluster mass function (IGECMF) . . . 28
- 2.4 From the ECMF to the IGECMF – an exemplification . . . 29
- 2.5 Determining the star formation duration δt using the SFR–$M_{\rm ecl,max}$ relation . . . 32

3 Distribution of star formation rates during the rapid assembly of NGC 1399 as deduced from its globular cluster system **39**
3.1 Observed GC and UCD samples in Fornax 40
3.2 Correction of the observed GC/UCD sample 44
3.3 Replication and Decomposition of the GC/UCD sample 51
3.4 Distribution of necessary SFRs 58
3.5 Discussion 61
3.5.1 Assumptions 62
3.5.2 Results 63
3.5.3 Formation of NGC 1399 and its GC/UCD system 67

4 Distribution of star formation rates during the rapid assembly of NGC 1399 as deduced from its red and blue globular clusters **71**
4.1 New spectroscopic and photometric surveys 72
4.1.1 VIMOS spectroscopy 72
4.1.2 Fornax Deep Survey (FDS) 72
4.2 Compilation of the spectroscopic GC/UCD sample 75
4.2.1 Matching of all available data 75
4.2.2 Selection of the final GC/UCD sample 76
4.3 Compilation of the photometric GC/UCD sample 81
4.4 Mass determination 84
4.5 Combination of the photometric and spectroscopic sample 88
4.6 Correction of the mass functions of red and blue GCs/UCDs . . . 89
4.7 Decomposition of the red and blue GC/UCD mass functions into individual SC populations 92
4.8 Distribution of necessary SFRs 95
4.9 Discussion 98
4.9.1 Assumptions 100
4.9.2 Results 101
4.9.3 Formation of NGC 1399 and its red and blue GC/UCD system 104

5 Conclusions and Outlook **109**
5.1 Findings regarding the red and blue GCs/UCDs around NGC 1399 109
5.2 Strenghts of the presented approach 115
5.3 Possible improvements of the presented method 117
5.4 Outlook 120

Bibliography **127**

List of Figures

1.1 Luminosity-size relation for stellar systems. 6
1.2 Central region of the Fornax galaxy cluster. 9
1.3 The giant elliptical NGC 1399 in the center of the Fornax galaxy cluster. 11
1.4 "Madau plot": evolution of the SFR as a function of redshift. . . . 17

2.1 Sketch: how star formation activities shape the IGECMF 30
2.2 SFR–$M_{\rm ecl,max}$ relation 33
2.3 Duration of one SC formation epoch, δt, and the reduced $\chi^2_{\rm red}$ as a function of β 35

3.1 Cumulative mass functions of the spectroscopic and the photometric sample. 43
3.2 Present-day and natal cumulative mass functions of the combined GC/UCD sample. 49
3.3 Sketch: how the observed GC/UCD cumulative mass distribution is decomposed into individual SC populations. 52
3.4 Natal and replicated GC/UCD cumulative mass functions for the standard approach. 54
3.5 Comparison of the natal and the replicated GC/UCD cumulative mass functions for all approaches. 57
3.6 Cumulative number of SC formation epochs as a function of the SFR for all approaches. 60

4.1 Spatial distribution of photometric objects in the Fornax galaxy cluster. 73
4.2 3D plot $g-r$ vs. $g-i$ vs. $r-i$ for the spectroscopic GC/UCD sample. 78

4.3 3D plot $u-g$ vs. $u-r$ vs. $u-i$ for the spectroscopic GC/UCD sample. 79
4.4 2D color distribution of GCs/UCDs after rotating the plane of data points from the spectroscopic sample from Fig. 4.2. 80
4.5 2D color distribution of GCs/UCDs for the photometric sample. . 83
4.6 Cumulative present-day spectroscopic and photometric, as well as the combined and natal mass functions for red and blue GCs/UCDs. 86
4.7 Cumulative present-day mass functions of red and blue GC/UCD based on the spectroscopic sample for different evolutionary models and different ages. 87
4.8 Cumulative natal and replicated GC/UCD mass functions of the blue sample, red sample, and red sample without UCD3 for $\beta = 2.0$. 94
4.9 Cumulative number of SC formation epochs as a function of the SFR for the blue, and red GCs/UCDs as well as the red GCs/UCDs after excluding UCD3. 97

5.1 Cumulative present-day mass function of the four metal-poor GCs around the Fornax dwarf spheroidal galaxy and the replicated mass functions as a function of β. 123

List of Tables

2.1 Duration of one SC formation epoch, δt, as a function of β 36

3.1 Determination of the ambient density based on different mass models to estimate the lifetime of a 10^4 $M_\odot$ SC based on different conversion relations as a function of the radius. 48

3.2 Total number of SC formation epochs, the total SC formation time, and the total stellar mass formed during that time for all approaches based on all GCs/UCDs irrespective of their color. . . 66

4.1 Parameters $a_{\rm ev}$, $b_{\rm ev}$, and $c_{\rm ev}$ for the red and blue GCs/UCDs. 90

4.2 Total number of SC formation epochs, the total SC formation time, and the total stellar mass formed during that time for all approaches based on red and blue GCs/UCDs. 99

5.1 The total stellar mass, and the stellar mass of the first and second SC population, generated to match the mass distribution of the four metal-poor GCs around the Fornax dwarf as a function of β. . 124

Zusammenfassung

Die elliptische Riesengalaxie NGC 1399 im Zentrum des Fornax Galaxienhaufens besitzt zahlreiche Kugelsternhaufen (globular clusters, GCs) und ultra-kompakte Zwerggalaxien (ultra-compact dwarf galaxies, UCDs). UCDs und GCs haben viele Gemeinsamkeiten, weshalb ich in meiner Arbeit voraussetze, dass sich die meisten UCDs wie Sternhaufen (star clusters, SCs) gebildet haben. Ich benutze die Massenfunktion der GCs und UCDs um Rückschlüsse über vergangene Sternbildungsaktivitäten zu ziehen.

Aus den photometrischen Eigenschaften jedes untersuchten GC/UCD wurde seine Masse abgeleitet, woraus sich die heutige Massenfunktion aller GCs/UCDs ergeben hat. Um die Massenfunktion aller GCs/UCDs zum Zeitpunkt ihrer Bildung zu bestimmen, wurde die Masse jedes GC/UCD korrigiert. Dabei wurde der Massenverlust durch stellare Entwicklung und durch die Bewegung im Gezeitenfeld der Heimatgalaxie berücksichtigt. Außerdem wurden aus der korrigierten Massenfunktion Objekte entfernt, die keine SCs sind.

Meiner Arbeit liegt die Annahme zugrunde, dass die GCs/UCDs aus vielen einzelnen SC Populationen bestehen, die zu verschiedenen Zeiten entstanden sind. Für die Massenverteilung jeder SC Population wird ein Potenzgesetz mit der Steigung $-\beta$ bis zum stellaren oberen Massenlimit, $M_{\rm max}$, angenommen, welches von der Sternbildungsrate (star formation rate, SFR) abhängt. Ich zerlege die korrigierte GC/UCD Massenfunktion in einzelne SC Populationen und wandle das $M_{\rm max}$ jeder SC Population in eine SFR um. Diese Methodik wird einmal auf die gesamte GC/UCD Massenfunktion und einmal auf die Massenfunktion der roten, metallreichen und der blauen, metallarmen GC/UCD angewendet. Die resultierenden SFR Verteilungen legen offen, unter welchen Bedingungen sich alle GCs/UCDs ebenso wie die roten und blauen GCs/UCDs gebildet haben.

Unter Berücksichtigung der heutigen Masse und des Alter von NGC 1399 und ihrer GCs/UCDs beschreibt das theoretische Modell die Bildung von GCs/UCDs für $\beta < 2.3$ konsistent, was mit der Beobachtung von typischerweise $\beta \approx 2.0$ in jungen SCs übereinstimmt. Die abgeleiteten Maximalwerte für die SFRs liegen zwischen etwa 200 und 2 000 $M_{\odot}{\rm yr}^{-1}$, wobei blaue GCs/UCDs geringere SFRs benötigen als rote GCs/UCDs, da sie generell weniger Masse besitzen. Alles zusammen erlaubt die Interpretation, dass sich die roten GCs/UCDs zusammen mit dem Spheroid von NGC 1399 in einem relativ kurzen, intensiven Starburst gebildet haben, während die blauen GCs/UCDs weniger hohe SFRs benötigen und sich unabhängig von NGC 1399 gebildet haben könnten und möglicherweise akkretiert wurden.

Abstract

The giant elliptical NGC 1399 in the center of the Fornax galaxy cluster possesses a rich system of globular clusters (GCs) and ultra-compact dwarf galaxies (UCDs). UCDs share many properties with GCs which is why I assumed in my thesis that most of them are the result of star cluster (SC) formation processes and used the mass function of GCs and UCDs to draw conclusions about their past star formation activities.

Based on the photometric properties of each GC/UCD in the sample its mass was deduced, from which the present-day mass function of all GCs/UCDs was obtained. To derive the natal mass function of all GCs/UCDs, the mass of each GC/UCD was corrected for the loss of mass due to stellar evolution and due to the tidal field of the host galaxy. Also, non-SC objects were excluded from the natal GC/UCD mass function.

I assume that the GCs/UCDs are an accumulation of many individual SC populations that formed during different formation epochs. The SC masses of each population are distributed according to the embedded cluster mass function, a pure power law with the slope $-\beta$ up to the stellar upper mass limit, $M_{\rm max}$, which depends on the star formation rate (SFR). After decomposing the natal GC/UCD mass function into individual SC populations, I convert $M_{\rm max}$ of each SC population to an SFR. This approach was applied to the overall GC/UCD mass function and to a red, metal-rich, and a blue, metal-poor, GC/UCD sample. The resulting SFR distributions reveal under which conditions the whole sample as well as the red and blue GC/UCD sample formed.

Accounting for the present day stellar mass and the age of NGC 1399 and its GCs/UCDs, the framework offers a consistent description for the formation of GCs/UCDs for $\beta < 2.3$. This agrees very well with the observation of young SCs where $\beta \approx 2.0$ is usually found. Realistic peak SFRs lie between roughly 200 and 2 000 $M_{\odot}{\rm yr}^{-1}$ and it emerges that blue GCs/UCDs generally require lower SFRs than red GCs/UCDs since they are generally less massive. Considering all available constraints allows the interpretation that red GCs/UCDs formed together with the spheroid of NGC 1399 in a relatively short, intense starburst early on, while blue GCs/UCDs require lower SFRs and could have formed independent of NGC 1399, possibly as an accreted population.

Chapter 1

Introduction

This thesis concentrates on the question under which conditions globular clusters (GCs) and ultra-compact dwarf galaxies (UCDs) around central galaxies of galaxy clusters formed and which constraints this sets on the formation of their host galaxy. In the following, I explain first what type of objects GCs and UCDs are and what is known about their formation (Chaps. 1.1 and 1.2). Then, I consider the environment in which the GCs and UCDs I am interested in are found: these are the giant central cluster galaxy NGC 1399 and the surrounding Fornax galaxy cluster (Chap. 1.3). Afterwards, I introduce my approach and explain why the GC/UCD system around NGC 1399 is an ideal target and why the quantity star formation rate (SFR) is a useful measure to quantify the formation process of star clusters (Chap. 1.4). Finally, I give an overview of how this thesis is structured in Chap. 1.5.

1.1 Star clusters and their formation

Star clusters (SCs) are groups of stars that form coevally out of the same giant molecular cloud and have radii of typically less than 10 pc. They are considered to be the fundamental building blocks of galaxies because most – if not all – stars form in SCs. Historically, two distinct types of SCs were differentiated because both types were known from the Milky Way (MW): open clusters and globular clusters. They were considered to be fundamentally different without any overlap in mass and age since they show no similarities apart from their similar sizes – and the fact that they contain an assembly of stars. However, the discovery of so-called young massive star clusters in external galaxies revealed that their properties agree

with either one or the other type of SCs and they are therefore believed to be the interlink between open clusters and globular clusters. In the following, these three types of SCs are reviewed separately.

Open Clusters
Open Clusters (OCs) contain typically between only a few and up to thousands of stars and have a mass from less than 100 $M_\odot$ to more than 10^4 $M_\odot$. In spiral galaxies, they are confined to the galactic plane, and are almost always located within spiral arms while in irregular galaxies, they can be found throughout the galaxy but are always connected to gaseous regions. Generally, OCs are only found in places where star formation is taking place and their concentration is highest where the molecular gas density is highest. The lack of molecular gas and therefore the absence of star formation explains why OCs have not been found in elliptical galaxies. They are mostly young objects with ages up to a few 10 Myr. Relatively speaking, they are not very densely populated and thus not very tightly gravitationally bound so that over time, they disperse relatively quickly, building up the field star population of the galaxy. The latter process is accelerated by the gravitational influence of other massive objects in their vicinity like giant molecular clouds or other star clusters. This is the reason why OCs with young ages are observed predominantly. Even if a OC dissolves and the member stars are not bound to each other any more, some of these stars will continue to move broadly in the same direction which is why these stars are referred to as a stellar association or a moving group. Well-known OCs in the MW are for instance the Pleiades or the Hyades which are visible with the naked eye.

Globular clusters
Globular clusters (GCs) are spherical groups of stars with between a few thousands and up to several millions of stars and their mass ranges from 10^3 $M_\odot$ to several 10^6 $M_\odot$. As compared to OCs, they have a much higher number of stars within approximately the same volume and are therefore much stronger gravitationally bound. Generally, GCs are located in the bulge or in the halo of a galaxy and orbit their host galaxy as a satellite. GCs are not found in the disk of galaxies which allows them to survive over much longer timescales as compared to OCs; typically, their age is above 10 Gyr. The presence of GCs is a very typical property for galaxies – even some dwarf galaxies have their own GCs. This suggests that the formation of GCs is closely related to the formation of their parent galaxies. There are several properties of GC systems that are correlated to their host

galaxies: for instance, the number of GCs scales with the luminosity and thus the mass of the host such that brighter and thus more massive galaxies possess a larger number of GCs. Also, the number of GCs depends on the morphology of the parent galaxy: per unit luminosity, ellipticals have more GCs than spirals (e.g., Harris 1991; Elmegreen 1999).

Young massive star clusters

Young massive star clusters (YMCs) have similarities with both, OCs and GCs, since they are as young as OCs but as massive as GCs. They have also been called super star clusters (SSCs) in which the prefix "super" hints at the fact that they are much brighter than OCs because they contain much more stars – in particular OB stars which are notably bright – and therefore more mass than OCs. Typical masses reach up to more than 10^6 $M_\odot$ – rather similar to GCs – but they are still relatively young objects with ages from around 10 Myr and up to a few Gyr – rather similar to OCs (e.g., Bastian et al. 2006; Kissler-Patig et al. 2006). Thus, YMCs might be the more massive versions of OCs. YMCs are observed in various dwarf and spiral galaxies with molecular gas; their common feature is a massive burst of star formation induced by gravitational interactions or mergers of the involved galaxies. The most prominent example are probably the Antennae galaxies but YMCs are also observed in the Large and Small Magellanic Clouds. Since YMCs are roughly as tightly bound as GCs are it is not surprising that they can still be observed at older ages than OCs: they can survive the surrounding tidal field over much longer timescales while OCs dissolve relatively quickly because of their low mass. Even more, it is suspected that their lifetimes could reach the age of GCs which is why they might be precursors of GCs. Indeed, it has been argued that at least the most massive YMCs might survive over a Hubble time and evolve into GC-type objects (e.g., de Grijs et al. 2001). This is fascinating since it would imply that the ancient building blocks of galaxies are still formed today induced by perturbations of nearby galaxies, interactions, or even during mergers of galaxies. Since YMCs form typically from enriched material, their metallicity might be higher than that of present-day GCs which have typically sub-solar metallicities. However, this does not imply that today's YMCs are fundamentally different from ancient GCs since GCs with super-solar metallicities have also been observed in massive galaxies (e.g., Puzia et al. 2005).

In this respect, it appears natural to assume that the formation of GCs occurred in a similar way as the formation of YMCs today (e.g., Fall & Rees 1977; Okazaki & Tosa 1995; Fall & Zhang 2001; Elmegreen 2010; Kruijssen 2014; Longmore

et al. 2014; Bastian 2016). Fortunately, the latter is relatively well understood. Thus, I explicitly assume that ancient GCs are formed in the same way as SCs today and introduce all details regarding SC formation in Chap. 2.2. The main points in brief: an SC population forms during one SC formation timescale, δt, and the masses of the SCs are distributed according to the embedded cluster mass function (ECMF). The latter is described by a power law with the slope $-\beta$ within the mass limits between $M_{\rm min}$ and $M_{\rm max}$. Each SC population can be characterized by its most massive SC, $M_{\rm ecl,max}$; this will be of importance later. It is known from observations that $M_{\rm ecl,max}$ is a function of the star formation rate (SFR) in the sense that star formation episodes with higher SFRs lead to the formation of SC populations with higher $M_{\rm ecl,max}$. This is known as the SFR–$M_{\rm ecl,max}$ relation (Weidner et al. 2004; Randriamanakoto et al. 2013) and will allow me to use GCs as tracers of the star formation and assembly history of a galaxy.

1.2 Ultra-compact dwarf galaxies

GCs are now known since well over a century and have been studied extensively since then which is why it is not surprising that they are very well understood. In contrast to that, ultra-compact dwarf galaxies (UCDs) are only known for less than two decades and in particular during the first half of it, there were some difficulties to characterize these objects. However, thorough studies with advanced observing techniques helped to unravel their ambivalent nature.

After their first discoveries by Minniti et al. (1998), Hilker et al. (1999b), and Drinkwater et al. (2000) around NGC 1399 in the Fornax galaxy cluster, UCDs have been found in other galaxy clusters like Virgo (e.g., Haşegan et al. 2005; Jones et al. 2006; Evstigneeva et al. 2007b; Brodie et al. 2011), Hydra (e.g., Wehner & Harris 2007; Misgeld et al. 2011), Coma (e.g., Madrid et al. 2010; Chiboucas et al. 2011), Perseus (Penny et al. 2012, 2014), Antlia (Caso et al. 2013), and other galaxy clusters. Moreover, they have been detected in some galaxy groups (e.g., Evstigneeva et al. 2007a; Da Rocha et al. 2011), around the fossil group NGC 1132 (Madrid 2011; Madrid & Donzelli 2013), around the bright elliptical NGC 3923 in a small group (Norris et al. 2012), and also around M 104, the Sombrero galaxy (Hau et al. 2009). Even though UCDs are a new type of object, it appears that they are not "exotic" since they are found rather commonly in all environments above a certain mass or size (Madrid 2011; Madrid & Donzelli 2013).

The properties of UCDs can be summarized as follows: they have luminosities in the range $-14 < M_V < -10$ mag and radii up to around 100 pc making them significantly brighter and larger than typical GCs. Their masses lie above about 10^6 $M_\odot$ and they are generally old with ages above 8 Gyr while many UCDs are compatible with being as old as the Universe. Moreover, some UCDs exhibit a faint envelope even beyond a radius of 100 pc. These numbers vary slightly depending on the definitions in different works but all values fall roughly in the above given ranges. Nevertheless, because of their luminosities and sizes, UCDs started to fill the originally empty gap between GCs and dwarf galaxies in the luminosity–size plane as can be seen in Fig. 1.1. Previously, two separate class of objects were known in the luminosity–size plane: the "galaxian" family with all types of galaxies (colored symbols) and the objects falling in the "star cluster" category (gray and black symbols). UCDs (asterisks) extend the region in which GCs (gray dots) are located toward the regions where compact ellipticals (cEs, purple triangles) and (dwarf) ellipticals (Es/dEs, blue triangles, red and orange circles) are found. This area is also populated by nuclear star clusters (black empty squares and gray filled squares).

Since it is known that the formation of galaxies and star clusters differ considerably, these findings triggered the question of the origin of the UCDs. Apparently, some UCDs are very similar to nuclei of dwarf galaxies while others seem to be rather related to GCs in terms of luminosity and size. This is why two main formation scenarios for UCDs are discussed in the literature (e.g., Evstigneeva et al. 2008; Chilingarian et al. 2008, 2011; Mieske et al. 2012; Francis et al. 2012):

(a) UCDs are dynamically evolved nucleated dwarf galaxies, from which the outer stellar components were removed while orbiting their host galaxy and suffering from its gravitational tidal field, leaving only a compact nuclear remnant. This formation channel is called the threshing or stripping scenario (e.g., Bekki et al. 2001, 2003a; Drinkwater et al. 2003; Goerdt et al. 2008; Thomas et al. 2008; Pfeffer & Baumgardt 2013; Pfeffer et al. 2014, 2016).

(b) UCDs are the brightest GCs of globular cluster systems and thus they are the result of star cluster formation processes (e.g., Mieske et al. 2002, 2012). Moreover, it has been proposed that the very massive UCDs could also form in the so-called merged star cluster scenario, where massive complexes of star clusters merge and thereby form a "super star cluster" (Kroupa 1998; Fellhauer & Kroupa 2002; Mieske et al. 2006; Brüns et al. 2011; Brüns & Kroupa 2012).

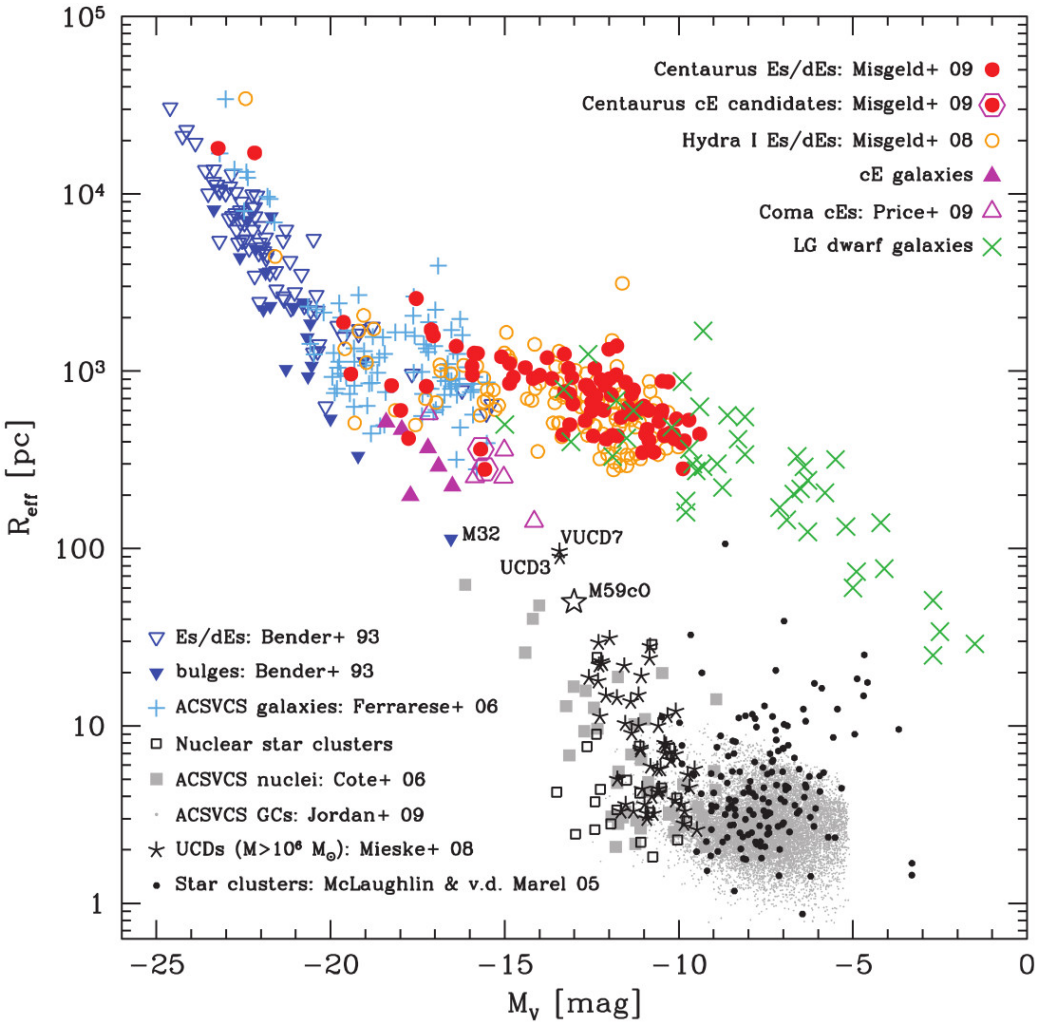

Figure 1.1: Luminosity-size relation for stellar systems as denoted in the figure. Taken from Misgeld & Hilker (2011).

Studies based on individual UCDs found that some of them formed likely through stripping (e.g., Caso et al. 2013; Norris et al. 2015) while others were rather categorized as massive GCs (e.g., Hau et al. 2009; Faifer et al. 2017). The Fornax galaxy cluster and its central giant elliptical NGC 1399 as well as the Virgo galaxy cluster and its central cluster galaxy M 87 were and still are a prime targets to tackle the question about the origin of the UCDs. In Virgo, a fraction of the very massive UCDs are thought to be of galaxian origin (e.g., Strader et al. 2013; Seth et al. 2014; Liu et al. 2015a,b; Norris et al. 2015), while a fraction of the faintest

(and thus lowest mass) UCDs might instead be related to compact SCs (Brodie et al. 2011). Over the years, it became more and more evident that UCDs are rather a "mixed bag of objects" (Hilker 2009b) than a distinct type of stellar system. In fact, many studies which are concentrated on the investigation of a sample of UCDs around an individual galaxy come to the conclusion that both formation channels are contributing to UCDs (e.g., Mieske et al. 2004; Chilingarian et al. 2008; Norris & Kannappan 2011; Chiboucas et al. 2011; Da Rocha et al. 2011; Penny et al. 2012, 2014; Wittmann et al. 2016).

Thus, the current picture of UCD formation allows two co-existing formation scenarios: first, a star cluster origin in which the properties of the UCDs are similar to bright GCs and thus characterized by lower luminosities, compact sizes, older ages, and a super-solar [α/Fe] abundance since they would have formed their stars within a short period of time. Second, an origin as tidally stripped dwarf nuclei in which UCDs have higher luminosities, are more extended spatially, and might have younger ages (Da Rocha et al. 2011). This scheme was refined by Norris & Kannappan (2011): they assume that a GC sample is a composite of "normal" GCs and lower mass stripped dwarf nuclei that appear as GCs. The "normal" GCs themselves are composed of GCs that formed in situ and GCs that were accreted from surrounding galaxies. Above a mass of $2 \cdot 10^6\ M_\odot$, corresponding to a luminosity of $M_V \approx -10$, UCDs start to show a mass-size relation and a likely mass-metallicity relation, known as the blue tilt. Up to the mass of $7 \cdot 10^7\ M_\odot$, corresponding to a luminosity of $M_V \approx -13$, UCDs are either giant GCs or stripped nuclei while above this mass, UCDs are almost exclusively remnant nuclei.

At this point, it should be noted that the term "UCD" introduced by Phillipps et al. (2001) is to some extent misleading since not all of these objects are of galaxian origin. The more neutral term "dwarf-globular transition object" (DGTO) has been suggested by Haşegan et al. (2005) but nevertheless, "UCD" was widely adopted in the literature. Thus, I will use "UCD" in my thesis as well but I would like to emphasize that this name does not necessarily describe the nature of UCDs.

1.3 NGC 1399 in the center of the Fornax cluster and its rich globular cluster system

After the considerably larger Virgo galaxy cluster, Fornax is the second closest galaxy cluster and is approximately 19 Mpc away from us based on a distance modulus of $(m - M) = 31.4 \pm 0.2$ (Dirsch et al. 2003, 2004, see also Ferrarese

et al. 2000; Blakeslee et al. 2009). The Fornax galaxy cluster consists of almost 60 bright galaxies and is mostly located in the constellation Fornax in the southern hemisphere. It is dominated by old galaxies, ellipticals and S0's, as can be seen in the optical image in Fig. 1.2 in which the brightest galaxies are labeled.

The center of Fornax is occupied by the giant elliptical NGC 1399. It is a typical central cluster galaxy in the sense that it is very massive with a total stellar mass of at least $6 \cdot 10^{11}$ $M_\odot$ (Richtler et al. 2008; Iodice et al. 2016) and it is composed mostly of old stars as its stellar age is about 11.5 ± 2.4 Gyr (Trager et al. 2000). Moreover, it harbors a super-massive black hole with a mass of about $5 \cdot 10^8$ $M_\odot$ (Gebhardt et al. 2007) and has an extended, diffuse halo around it as can be seen in Fig. 1.3.

Based on the investigation of a single photographic plate in the mid 70s, a significant clustering of faint objects around NGC 1399 and two other galaxies in the Fornax galaxy cluster was reported by Dawe & Dickens (1976). Already then the authors suspected that at least some of the objects might be unresolved GCs – because of the large distance and the compact sizes of GCs, they appear as point-like sources and cannot be resolved into stars. The authors were absolutely right – most of the point-like, faint objects around NGC 1399 in Fig. 1.3 are indeed GCs. A significant number of studies followed (e.g., Bridges et al. 1991; Grillmair et al. 1994; Kissler-Patig et al. 1997, 1998, 1999; Mieske et al. 2002; Richtler et al. 2004; Bassino et al. 2006a) and it became clear over the years how rich the GC system is: for instance, Forbes et al. (1998) estimated 5 700 GCs while Dirsch et al. (2003) arrived at 6 450 ± 700 GCs within a radius of 15′ which corresponds to roughly 83 kpc. Increasing the considered radius, Gregg et al. (2009) estimated 11 100 ± 2 400 GCs within a radius of 0°.9 around NGC 1399, corresponding to 320 kpc.

Furthermore, the GC system of NGC 1399 shows a bimodal color distribution (e.g., Bassino et al. 2006a; Blakeslee et al. 2012; Kim et al. 2013; D'Abrusco et al. 2016) meaning that one part of the GCs have rather red colors while the other part is rather blue. This is a general characteristic of galaxies with a sufficient mass. The old ages of the GCs which lie between 8 and 13.4 Gyr (Forbes et al. 2001; Kundu et al. 2005; Hempel et al. 2007; Firth et al. 2009; Chilingarian et al. 2011; Francis et al. 2012) imply that red GCs are metal-rich while blue GCs are metal-poor. This offers the opportunity to study how properties of GCs differ depending on the color and thus the metallicity, probably reflecting the spheroid (red GCs) and halo (blue GCs) formation of the host galaxy. In this way, (radial) color gradients (Ostrov et al. 1993; Liu et al. 2011; Kim et al. 2013), the radial distribution of blue and red clusters (Bassino et al. 2006a; Schuberth et al. 2010),

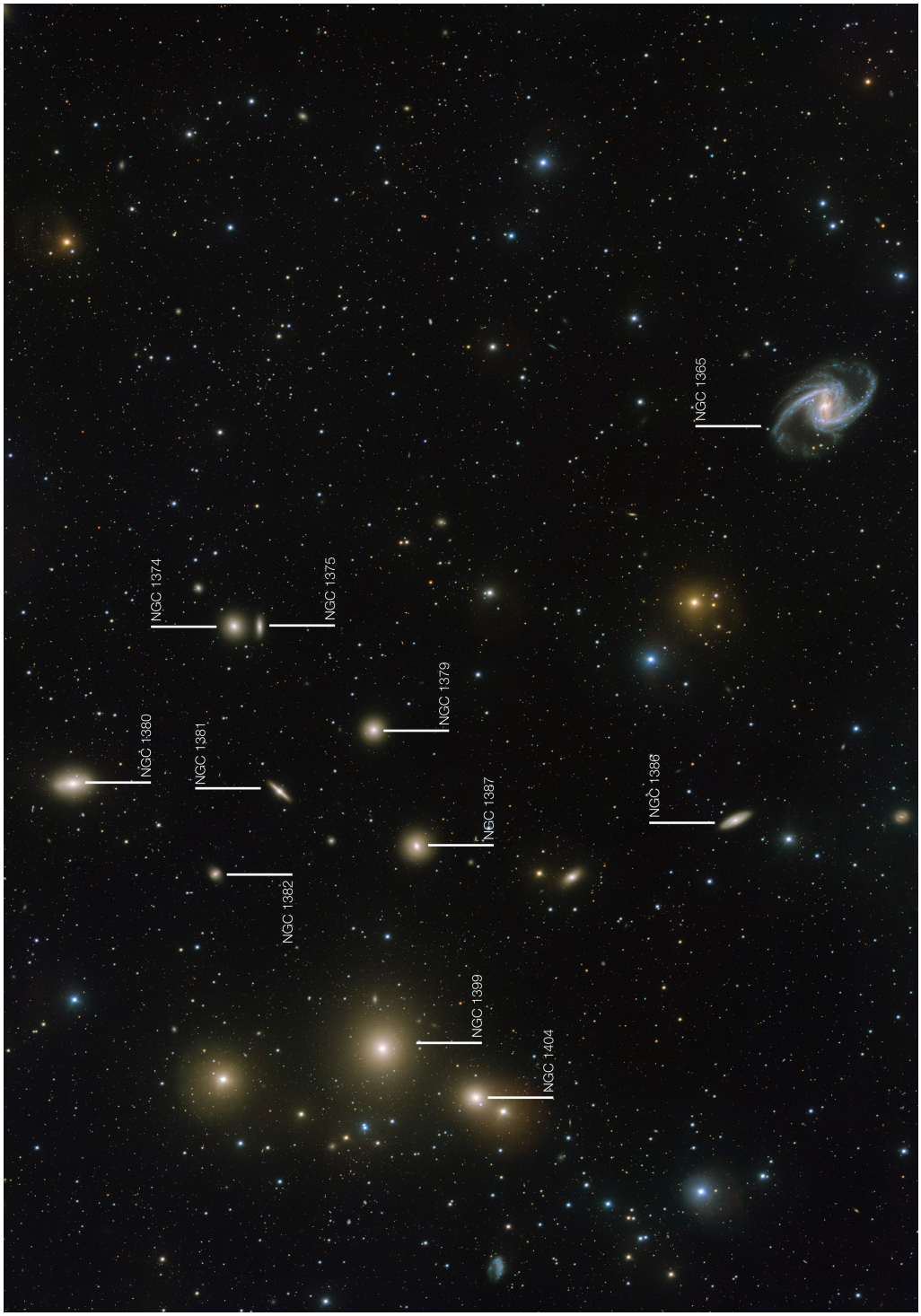

Figure 1.2: Optical image of the central region of the Fornax galaxy cluster as observed with the VLT Survey Telescope. The brightest galaxies are labeled. The angular distance between NGC 1399 and NGC 1365 is about 1° which corresponds to roughly 330 kpc at the distance of Fornax. Credit: ESO

the color-magnitude relation (Mieske et al. 2010), and GC structural parameters of red and blue GCs (Masters et al. 2010; Puzia et al. 2014) have been investigated. Here, it will be not only be examined under which conditions the GCs/UCDs around NGC 1399 formed but also to which extent the formation conditions differ between red and blue GCs/UCDs.

GCs around NGC 1399 have effective radii from smaller than 1 and up to 10 pc with an average of around 3 pc (Masters et al. 2010; Puzia et al. 2014). Their masses range from 10^4 $M_\odot$ up to lower than 10^7 $M_\odot$ (Puzia et al. 2014, their Fig. 15). UCDs, on the other hand, have some overlap with GCs, but also extend the parameter space to larger sizes and masses: their effective radii range from a few pc up to 100 pc (e.g., Drinkwater et al. 2003; Evstigneeva et al. 2007b, 2008; Hilker et al. 2007; Mieske et al. 2008), while their masses lie between 10^6 $M_\odot$ and lower than 10^8 $M_\odot$ (e.g., Drinkwater et al. 2003; Evstigneeva et al. 2007b; Hilker et al. 2007; Mieske et al. 2008; Frank et al. 2011), bridging the region between classical GCs and compact elliptical galaxies. As for UCDs in other environments, there is growing evidence that around NGC 1399, the term "UCD" does not necessarily describe one single type of object (e.g., Mieske et al. 2004; Evstigneeva et al. 2008; Wittmann et al. 2016): some UCDs might be the brightest GCs and could have formed from merging multiple massive SCs (e.g., Kroupa 1998; Mieske et al. 2002, 2012; Brüns et al. 2011) while others might be nucleated dwarf galaxies whose outer envelope was stripped (e.g., Bekki et al. 2001; Drinkwater et al. 2003; Thomas et al. 2008; Pfeffer & Baumgardt 2013, see also Chap. 1.2). It has been shown that the contribution of stripped nuclei seems to be negligible, except for the high-mass end of the GC/UCD mass function (Mieske et al. 2012; Pfeffer et al. 2014, 2016).

Even though there are clearly arguments that not all UCDs around NGC 1399 are actual GCs, there are several arguments in the literature that most of them are very massive GCs:

- The luminosities of GCs and UCDs are distributed smoothly and their luminosity functions do not show any bimodality (Mieske et al. 2002, 2004). Furthermore, the UCDs in Fornax are consistent with being drawn from the bright tail of the GC luminosity function. However, a small excess at the bright end is statistically possible (Mieske et al. 2004; Gregg et al. 2009; Mieske et al. 2012).

- GCs and UCDs form a continuum in the luminosity-size plane (Mieske et al. 2006).

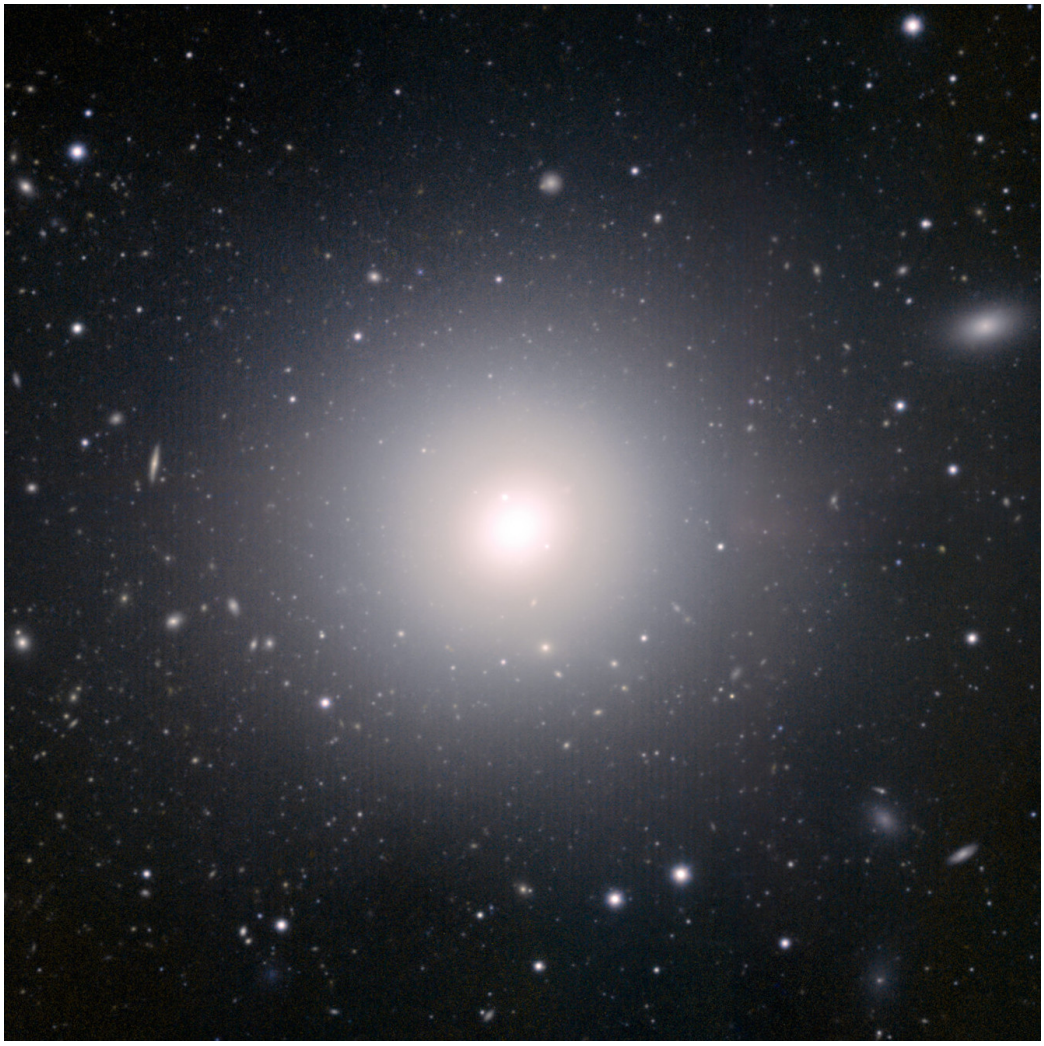

Figure 1.3: The giant elliptical galaxy NGC 1399 in the center of the Fornax galaxy cluster as observed with VISTA in the infrared. Note the large number of GCs surrounding NGC 1399 that appear as faint, point-like sources. This image is about 9 arcmin across, corresponding to approximately 50 kpc. Credit: ESO

- UCDs exhibit the full range of (high and low) metallicities as observed for GCs (Francis et al. 2012).
- The spread of age and metallicity of the UCDs is consistent with that observed for GCs (Francis et al. 2012).

- Most of the UCDs have super-solar α-element abundances, implying short formation times, similar to those of GCs (Francis et al. 2012).

However, even if the UCDs were not genuine GCs, several findings suggest that they are at least the result of an SC formation process:

- Kissler-Patig et al. (2006) placed YMCs with masses higher than $10^7 M_\odot$ on three different scaling relations and found their positions to be similar to those of the UCDs, in particular for the most massive YMCs.
- UCDs have metallicities close to but slightly below those of YMCs of comparable masses (Mieske et al. 2006).
- Fitting a simple stellar population model to the spectra of UCDs reveals that UCDs are in agreement with a pure stellar content (Hilker et al. 2007; Chilingarian et al. 2011) so that no dark matter component is needed in UCDs within their 1−3 half-mass radii (Hilker et al. 2007). Chilingarian et al. (2011) reported that almost all UCDs are compatible with no dark matter in them. Mieske et al. (2013, their Table 3) found that only the most massive UCDs require an additional mass component to compensate the elevated M/L ratio, which they suggested might be massive black holes, while the lower-mass UCDs do not need any form of additional, non-luminous matter (see also Dabringhausen et al. 2009, 2010, 2012).

In general, I follow Mieske et al. (2012) who found that most UCDs are compatible with being formed in the same way as GCs and assume that it is justified to treat UCDs – like GCs – as (very) massive SCs and assume that they formed in SC formation processes. Nevertheless, it is very likely that some of the most massive UCDs did not form in an SC formation process. One object whose nature is debated is UCD3. Even though Frank et al. (2011) found UCD3 to be fully consistent with a massive GC when surveying its internal kinematics, it remains a peculiar object: it has an effective radius of almost 90 pc (Evstigneeva et al. 2007b; Hilker et al. 2007; Frank et al. 2011) and its surface brightness profile is best fit with a two-component model (Drinkwater et al. 2003; Evstigneeva et al. 2007b) with a core that is surrounded by a halo with effective radii of around 10 and 100 pc, respectively (Evstigneeva et al. 2007b). Such a composition of a core and a halo could be interpreted as a not fully completed stripping process of a more extended object (Evstigneeva et al. 2008) but the merged star cluster scenario is a possible formation channel as well (Fellhauer & Kroupa 2005). Apparently,

UCD3 is not compatible with a typical GC for which reason in the subsequent analyses, it will be investigated how the results change as soon as it is excluded from the sample.

UCD3 is not the only object that shows peculiarities. More recently, it was reported that some of the UCDs exhibit extended surface brightness profiles or even tidal features (Richtler et al. 2005; Voggel et al. 2016) or appear asymmetric or elongated (Wittmann et al. 2016). In addition, Voggel et al. (2016) detected for the first time the tendency of GCs to cluster around UCDs. I expect that in the near future more and more studies will concentrate on the observations of individual UCDs to determine their properties and shed light on their nature – whether "genuine GCs" or merged SCs or stripped nuclei. Until then, theoretical considerations are helpful. For the merged SC scenario, no predictions have been made so far regarding the mass and the number of objects that could be expected in an environment like NGC 1399. Fortunately, for the dwarf galaxy threshing scenario, Pfeffer et al. (2014, 2016) estimated for a galaxy similar to NGC 1399 a possible number and mass of objects originating from stripping nucleated dwarf galaxies based on semi-analytic modeling. Their results will be taken into consideration as well.

1.4 Aim of the present thesis

The main goal of this thesis is to determine which distribution of SFRs is necessary to reproduce the observed mass distribution of GC/UCDs around NGC 1399. In summary, I proceed in the following way: using spectroscopic and photometric data of GCs and UCDs around NGC 1399, I convert their luminosities into masses and construct their overall mass function. This present-day GC/UCD mass function is related to the above mentioned ECMF as follows: it is assumed that every object of the GC/UCD sample formed in an SC formation process and is thus referred to as an SC. Each SC forms together with many other SCs during a star formation event, constituting an SC population which is characterized by a similar age and a mass distribution that is described by the ECMF, meaning that they form in a similar way as it is observed in star-forming galaxies in the local Universe today. Accumulating all SC populations ever formed in different formation epochs is equivalent to an addition of all corresponding ECMFs, which leads to their overall birth mass function. SCs are subject to changes, particularly in mass, as the SCs interact with the environment and the stars in these SCs become older. Both lead to mass loss in the course of time. Also, these SCs are observed as

GCs/UCDs today. This transforms the natal SC mass function to the present-day GC/UCD mass function.

To learn under which conditions the GCs/UCDs in the present-day mass function formed, two investigation steps are required: first, it is necessary to determine how aging affects each GC/UCD. I am particularly interested in quantifying how much mass each of them lost since its birth individually. For this, a model by Lamers et al. (2005a) is used which accounts for mass loss due to stellar evolution and gravitational interactions in tidal fields. Applying a mass correction for each GC/UCD individually enables me to reconstruct the natal GC/UCD mass function from their present-day mass function. Second, the natal GC/UCD mass function can then be decomposed into individual SC populations described by the ECMF. As mentioned above, the ECMF can be characterized by the most massive SC in the population, $M_{\mathrm{ecl,max}}$, which can be converted to an SFR using the SFR–$M_{\mathrm{ecl,max}}$ relation. Thus, when decomposing the natal GC/UCD mass function into individual ECMFs, an SFR can be obtained from the most massive GC/UCD, $M_{\mathrm{ecl,max}}$, of each GC/UCD population. The overall distribution of SFRs reveals finally the formation conditions of the GCs and UCDs around NGC 1399 and thus the host galaxy itself.

The summarized procedure is applied to the observed sample of GCs/UCDs around NGC 1399 several times, varying the considered sample slightly each time: in a first approach, the method is applied to all GCs/UCDs while in a second approach, the overall GC/UCD sample is divided into a red and a blue sample which are then analyzed separately. This reveals to which extent the formation condition between red and blue GCs/UCDs differ and offers the opportunity to check whether the findings of the presented method are self-consistent. Also, in separate cases, it is taken into account that some objects – like UCD3 or the stripped nuclei sample – are not the result of an SC formation process for which reason they are excluded from the sample before analyzing it. The resulting SFRs in conjunction with the previous SFRs allow to estimate how strongly these objects influence the outcome.

Why targeting the GC system around NGC 1399?
Since the discovery of its rich GC system, NGC 1399 has always been an attractive target for studying various properties of its GCs like their dynamics, radial distribution, or structural parameters, also in combination with its bimodal color distribution. The method presented in this thesis is of statistical nature and aims to decompose a sample of SCs into individual SC populations which are described by the ECMF. In doing so, it cannot be guaranteed that the objects which are assumed

to form an SC population formed indeed together. However, this circumstance can be weakened if there a many objects, in particular with similar masses, since this makes them exchangeable. Thus, the proposed method requires a sample that comprises many objects and is statistically robust. Consequently, any considerably large galaxy with numerous associated GCs would suit the method - a central giant elliptical with thousands of GCs will apparently be a prime target for such an analysis.

In practical terms, the situation is advantageous regarding the availability of data: on one hand, I used a compilation of the brightest GCs/UCDs that were observed spectroscopically in many different studies. The membership of each object was confirmed by measurements of its radial velocity which was extracted from the corresponding spectrum. Assuming that all GCs/UCDs have comparable M/L-ratios this implies that these brightest objects are also among the most massive around NGC 1399, making the high-mass end of the present-day GC/UCD mass function robust since all objects were observed individually. On the other hand, a photometric sample of GCs/UCDs was available based on observations with the Advanced Camera for Surveys (ACS) on the Hubble Space Telescope (HST). Fortunately, GCs are still resolved with the HST at Fornax distance allowing to compile a reliable sample. Photometric analyses are able to detect objects with lower luminosities, and therefore with lower masses. Such objects occur much more frequently than brighter objects which is why a photometric sample is particularly reliable in the intermediate- and low-mass regime. However, the two samples were not ideal: the spectroscopic sample comprised mostly objects within a radius of 85 kpc around NGC 1399; further away the coverage became sparse. The photometric sample on the other hand, had reliable number counts up to a radius of 160 kpc but this area was not covered entirely due to the small field-of-view of the ACS camera, making a scaling necessary.

Moreover, during the time of my PhD, spectroscopic data from VIMOS and photometric data from the Fornax Deep Survey (D'Abrusco et al. 2016; Iodice et al. 2016) became available which allowed two main improvements: first, both surveys covered the area of 160 kpc around NGC 1399 fully. Second, I was able to cross match the spectroscopic with the photometric data and had therefore uniform photometry measurements for both samples. The large number of objects in both samples allowed me to identify the color bimodality in each of the samples quantitatively and enabled me to discern for each individual object in both samples reliably whether it belongs to the red or the blue population. After this important step, the GC/UCD mass function could be determined and analyzed for red and blue objects separately.

Why determining SFRs to constrain the formation history?
The quantity SFR is measured in $M_\odot$/yr and quantifies how much mass is converted from gas into stars over a certain period of time. It is known that the formation timescale for SCs is approximately 10 Myr (see e.g. Chap. 2.5) so that it can simply be estimated how much stellar mass is produced: for instance, an SFR of 1 $M_\odot$/yr implies that over one SC formation epoch, a stellar mass of 10^7 $M_\odot$ is formed. If it is instead known for how long and at which SFR stars were formed, the stellar mass produced during that time can be calculated accordingly. Knowledge about the amount of the produced stellar mass also indicates the required mass in molecular gas since only a fraction of the molecular mass is converted to stellar mass. This conversion factor is known as the star formation efficiency and it lies between 10 and 30% (e.g., Lada & Lada 2003). These numbers imply that between 3 and 10 times more molecular gas mass is required to form stars of a certain mass. Taking this into account, recalling the masses of GCs, and remembering that not only one object but a whole population of SCs is produced in an SC formation event, illustrates how massive the giant molecular clouds must have been that led to the formation of GCs.

Characteristic values for the SFR cover a wide range over several orders of magnitude: SFRs can be as low as 10^{-4} $M_\odot$/yr but also as high as 10^3 $M_\odot$/yr. For instance, typical values for dwarf galaxies range between 10^{-4} and a few $M_\odot$/yr depending on the strength of their star formation activities (e.g., Hunter et al. 2010; Rosenberg et al. 2008). Spirals usually have SFRs that are similar to the ones from star-forming dwarfs with 10^{-2} and 10 $M_\odot$/yr (Rossa & Dettmar 2003); the MW is with its SFR of about 2 $M_\odot$/yr (Chomiuk & Povich 2011) a typical spiral galaxy. Higher SFRs are detected in starburst galaxies where values up to several 10^2 $M_\odot$/yr are found (Sargsyan & Weedman 2009). These SFR values are observed in galaxies in the local Universe. Moving to higher redshifts, even higher SFRs between several 10^2 $M_\odot$/yr and up to several 10^3 $M_\odot$/yr are detected: for instance, at redshifts of $z \approx 0.5$ these SFR values can be reached in galaxy clusters in which star formation can be even more violent than in the local Universe (Mittal et al. 2017). For redshifts up to $z \approx 3$ similar SFRs are observed in interactions or mergers of gas-rich galaxies; these galaxies are characterized by high luminosities in the infrared for which reason they are called (ultra-/hyper-)luminous infrared galaxies ((U/H)LIRGs, e.g., Takata et al. 2006; Ruiz et al. 2013; Kilerci Eser et al. 2014). To detect heavily star-forming galaxies at even higher redshifts, observations are moved to far-infrared and sub-mm wavelengths which is why this type of galaxies are called sub-mm galaxies (SMGs), or more generally, dusty, star-forming galaxies (DSFGs) because these galaxies are highly obsured. They have

SFRs up to 10^3 $M_\odot$/yr (e.g., Alaghband-Zadeh et al. 2012; Swinbank et al. 2014; Simpson et al. 2015) and are presumed to be the progenitor of present-day massive galaxies going through heir highest star formation activities and not major mergers (Narayanan et al. 2015; Mancuso et al. 2016). Interestingly, they show the tendency to have higher SFRs with higher redshifts (da Cunha et al. 2015). This is in agreement with the finding that the SFR increase with redshift or lookback time (e.g., Le Floc'h et al. 2005; Speagle et al. 2014). This evolution is illustrated with the diagram in Fig. 1.4 which is known as the "Madau plot".

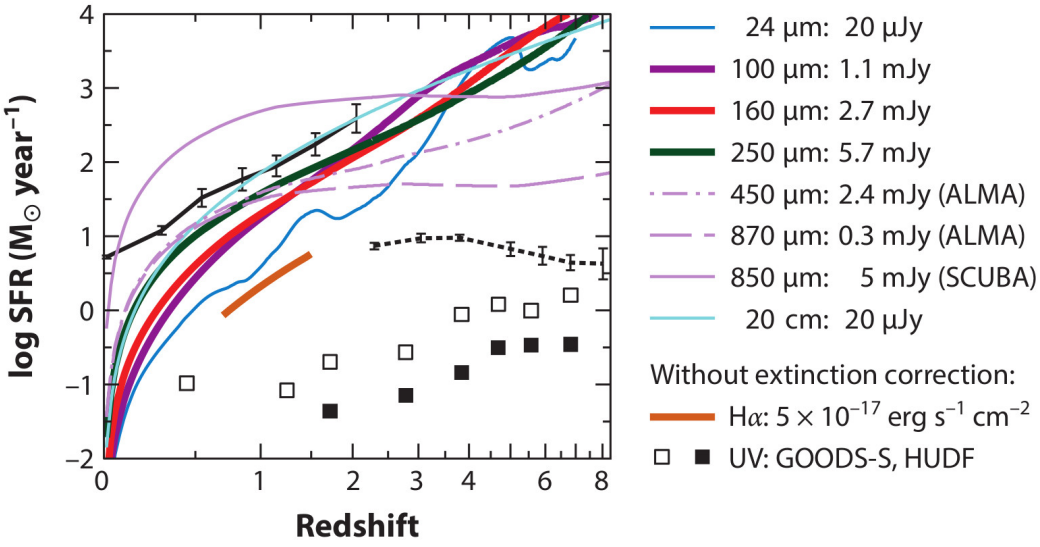

Figure 1.4: Evolution of the SFR as a function of redshift, known as "Madau plot". As can be seen, the SFR increases with lookback time independent of how the SFR is measured. Taken from Madau & Dickinson (2014).

Since this work is focused on the conditions under which GC formed it would be useful to get a feeling for the SFRs that can be expected. Given the old ages of the GCs, they must have formed early on at redshifts between roughly 2 and 5 (e.g., Kravtsov & Gnedin 2005). For this range of redshifts, Fig. 1.4 indicates that very high SFRs above roughly 10^2 $M_\odot$/yr up to 10^4 $M_\odot$/yr were predominant at that time. It will be interesting to see to which extent this rough estimate proves to be true.

1.5 Outline of the present thesis

My thesis is structured as follows: first, I present the underlying framework for this thesis in Chap. 2 which is based on my Diploma thesis. In Chap. 3, I determine the required SFRs based on all GCs/UCDs around NGC 1399. I first describe the available GC/UCD samples (Chap. 3.1) and evaluate then the mass loss for each object to determine the birth mass function for the GCs/UCDs (Chap. 3.2). Afterwards, this mass function is decomposed into individual ECMFs (Chap. 3.3) from which the distribution of necessary SFRs can be derived (Chap. 3.4). Finally, I discuss my assumptions, the results, and the implications on the formation of NGC 1399 and its GC system (Chap. 3.5).

In Chap. 4, I start with an introduction of the new spectroscopic and photometric surveys (Chap. 4.1). I use them to acquire a more reliable spectroscopic and photometric GC/UCD sample and explain how to separate the objects in both samples into red and blue GCs/UCDs (Chaps. 4.2 and 4.3). Based on the photometric properties of each object, I determine its mass in Chap. 4.4. I continue with the description of how the red and blue objects in the spectroscopic and photometric sample have to be combined to obtain a robust present-day mass function for red and blue GCs/UCDs separately in Chap. 4.5. Then, the present-day masses of all GCs/UCDs are corrected for mass loss (Chap. 4.6) and the corrected mass functions of red and blue GCs/UCDs are decomposed into individual SC populations (Chap. 4.7). From this, the required distributions of SFRs are obtained in Chap. 4.8 and discussed in Chap. 4.9.

In Chap. 5, I compare the two approaches and summarize all findings in Chap. 5.1. Afterwards, I highlight the strengths of the analysis in Chap. 5.2 and work out possible improvements of the analysis in Chap. 5.3. Finally, I discuss future perspectives of this work and apply the presented method to the GC system of the Fornax dwarf galaxy in Chap. 5.4.

Chapter 2

Underlying framework

The theoretical background of this work is based on my Diploma thesis which I submitted and successfully defended at the Argelander Institut für Astronomie at the University of Bonn. The content of the Diploma thesis was published afterwards in Schulz et al. (2015). All necessary ingredients that are relevant for this thesis are summarized in the following chapter. It starts with the description of a new sampling technique, called improved optimal sampling, in Chap. 2.1 which is then used in all subsequent chapters. Then, it is described in detail how star cluster formation is modeled and the embedded cluster mass function (ECMF) is introduced which describes how the masses of a newly born SC population are distributed. With this knowledge, the SFR–$M_{\rm ecl,max}$ relation is derived in Chap. 2.2. Afterwards, the concept of the integrated galactic embedded cluster mass function (IGECMF) is developed which describes the mass distribution of many SC populations accumulated during an formation period of arbitrary length in Chap. 2.3. For better understanding, the concept is visualized in Chap. 2.4. I continue then with the second important part of the underlying framework, namely how long it takes to form an embedded SC out of its parent molecular cloud. This length of one SC formation epoch, δt, is determined using the above mentioned SFR–$M_{\rm ecl,max}$ relation in Chap. 2.5.

2.1 Improving optimal sampling

A simple and commonly used method of discretizing a parental distribution function is by random sampling. The distribution function is perceived as a probability distribution function from which values are diced using a generation function.

Such an ensemble of sampled values naturally shows statistical deviations from the parental distribution function (Kroupa et al. 2013). However, for a wide range of applications it is necessary to accurately extract the number of objects as well as their individual masses from an arbitrary distribution function. This mass distribution function, denoted by $\xi(M)$, is described as

$$\xi(M) = \frac{\mathrm{d}N}{\mathrm{d}M}, \tag{2.1}$$

where $\mathrm{d}N$ is the number of objects in the mass interval M to $M + \mathrm{d}M$. The particular functional form of the distribution function, $\xi(M)$, is specified below and is not required for the general approach.

The outcome of any sampling technique should reproduce the number distribution, $\mathrm{d}N/\mathrm{d}M$, as well as the mass distribution, $M\ \mathrm{d}N/\mathrm{d}M$, as precisely as possible. If this is the case for a sample of objects, the corresponding distribution function is called "fully populated" throughout this thesis. Moreover, for any lower and upper mass limits, M_{min} and M_{max}, respectively, the total number of objects, N_{tot}, and the total mass, M_{tot}, should agree with the analytical computation of N_{tot} as well as of M_{tot} at the same time:

$$N_{\mathrm{tot}} = \int_{M_{\mathrm{min}}}^{M_{\mathrm{max}}} \xi(M)\ \mathrm{d}M, \tag{2.2}$$

$$M_{\mathrm{tot}} = \int_{M_{\mathrm{min}}}^{M_{\mathrm{max}}} M\ \xi(M)\ \mathrm{d}M. \tag{2.3}$$

Thus, the quality of a sampling method can be measured by how accurately the outcome resembles $\mathrm{d}N/\mathrm{d}M$ and $M\ \mathrm{d}N/\mathrm{d}M$ and how well the actual values for N_{tot} and M_{tot} agree with the analytical values (Eqs. (2.2) and (2.3)). Compliance with one of these four conditions does not imply that one or all other conditions are fulfilled as well.

One technique used to do this is the optimal sampling method developed by Kroupa et al. (2013) and later incorporated into the extended software package originally published by Pflamm-Altenburg & Kroupa (2006). It is designed to generate a population of stars from the initial mass function (IMF). The procedure requires the analytical form of the IMF, the physical upper mass limit for stars, m_{max}, and the total stellar mass of the embedded SC, M_{ecl}. As shown by Kroupa et al. (2013), their Fig. 1, optimal sampling nicely reproduces the shape of the IMF, $\xi_{\mathrm{IMF}}(M) = \mathrm{d}N/\mathrm{d}M$, without introducing any Poisson noise. However, a

closer look reveals that optimal sampling does not fulfill Eq. (2.2), as will be shown below.

Is it possible at all to devise a sampling technique that fulfills all four conditions and works without adding stochastic fluctuations to the outcome? It is, as will be developed in the following.

Starting with Eqs. (2.2) and (2.3), both integrals have to be divided into $N_{\rm tot}$ separate integrals, each integral representing one individual object:

$$\begin{aligned} N_{\rm tot} = &\int_{M_{\rm min}}^{m_{N_{\rm tot}}} \xi(M)\,{\rm d}M + \int_{m_{N_{\rm tot}}}^{m_{N_{\rm tot}-1}} \xi(M)\,{\rm d}M + ... + \\ &\int_{m_{i+1}}^{m_i} \xi(M)\,{\rm d}M + ... + \int_{m_3}^{m_2} \xi(M)\,{\rm d}M + \int_{m_2}^{M_{\rm max}} \xi(M)\,{\rm d}M, \end{aligned} \tag{2.4}$$

$$\begin{aligned} M_{\rm tot} = &\int_{M_{\rm min}}^{m_{N_{\rm tot}}} M\xi(M)\,{\rm d}M + \int_{m_{N_{\rm tot}}}^{m_{N_{\rm tot}-1}} M\xi(M)\,{\rm d}M + ... + \\ &\int_{m_{i+1}}^{m_i} M\xi(M)\,{\rm d}M + ... + \int_{m_3}^{m_2} M\xi(M)\,{\rm d}M + \int_{m_2}^{M_{\rm max}} M\xi(M)\,{\rm d}M, \end{aligned} \tag{2.5}$$

since in total there are $N_{\rm tot}$ objects. With $m_1 = M_{\rm max}$, the index of the upper limit, i, of each separate integral enumerates the individual objects. Thus, each separate integral must fulfill the two following requirements:

1. Each integral must give one object. Integration of $\xi(M)$ within the limits m_i and m_{i+1} yields exactly unity:

$$1 = \int_{m_{i+1}}^{m_i} \xi(M)\,{\rm d}M. \tag{2.6}$$

2. Then the mass of this i-th object, M_i, is determined by

$$M_i = \int_{m_{i+1}}^{m_i} M\,\xi(M)\,{\rm d}M, \tag{2.7}$$

where the limits m_i and m_{i+1} have to be equal to those in Eq. (2.6).

These two requirements ensure that the number distribution, $\mathrm{d}N/\mathrm{d}M$, and the mass distribution, $M\ \mathrm{d}N/\mathrm{d}M$, are reproduced and that N_{tot} and M_{tot} agree with the analytical values. Since $m_{i+1} < m_i$ with increasing number i the objects become less massive.

As this work considers the formation of SC distributions, the task is to generate an ideal population of SCs. However, the underlying concept is so general that it can be applied to any other type of object. For the sake of simplicity, it is assumed that the mass distribution function of SCs follows a one-part power law with the index β

$$\xi(M) = k\left(\frac{M}{M_{\mathrm{max}}}\right)^{-\beta} \tag{2.8}$$

within the lower and upper mass limit, M_{min} and M_{max}, respectively. k is a normalization constant. Similarly to Weidner et al. (2004), this function is normalized as follows:

$$1 = \int_{M_{\mathrm{max}}}^{M_{\mathrm{trunc}}} \xi(M)\ \mathrm{d}M, \tag{2.9}$$

with a truncation mass $M_{\mathrm{trunc}} = \infty$. This leads to a normalization constant, k,

$$k = (\beta - 1)\ M_{\mathrm{max}}^{-1}. \tag{2.10}$$

Here and in all following equations, $\beta > 1$ must be fulfilled. Otherwise, the antiderivatives of $\xi(M)$ and $M\ \xi(M)$ cannot be computed.

These ingredients enable computing the individual masses of the SCs. Equation 2.6 implies for the $(i+1)$-th integration limit of any of the separate integrals from Eq. (2.4):

$$\begin{aligned} 1 &= \int_{m_{i+1}}^{m_i} \xi(M)\ \mathrm{d}M = M_{\mathrm{max}}^{\beta-1}\left(m_{i+1}^{1-\beta} - m_i^{1-\beta}\right) \\ \Longleftrightarrow \quad m_{i+1} &= \left(m_i^{1-\beta} + M_{\mathrm{max}}^{1-\beta}\right)^{\frac{1}{1-\beta}} \quad \text{with} \quad m_1 = M_{\mathrm{max}}, \end{aligned} \tag{2.11}$$

which allows iteratively determining the integration limits of all separate integrals in (Eq. (2.4)). With these, the individual masses of all SCs of the ideal population can be computed, so that the i-th SC has a mass of

$$M_i = \int_{m_{i+1}}^{m_i} M\,\xi(M)\,\mathrm{d}M = \\ = \begin{cases} M_{\max}\,(\ln m_i - \ln m_{i+1}) & ,\ \beta = 2 \\ \frac{\beta-1}{2-\beta}\,M_{\max}^{\beta-1}\,(m_i^{2-\beta} - m_{i+1}^{2-\beta}) & ,\ \beta \neq 2. \end{cases} \tag{2.12}$$

Moreover, using Eq. (2.8), the expected total number of objects, N_{tot}, and their total mass, M_{tot}, as in Eqs. (2.2) and (2.3), can be evaluated analytically by replacing the lower and upper integration limits in Eqs. (2.11) and (2.12) with $M_{\min}$ and $M_{\max}$, respectively:

$$N_{\mathrm{tot}} = \int_{M_{\min}}^{M_{\max}} \xi(M)\,\mathrm{d}M = \left(\frac{M_{\max}}{M_{\min}}\right)^{\beta-1} - 1, \tag{2.13}$$

$$M_{\mathrm{tot}} = \int_{M_{\min}}^{M_{\max}} M\,\xi(M)\,\mathrm{d}M \\ = \begin{cases} M_{\max}\,(\ln M_{\max} - \ln M_{\min}) & ,\ \beta = 2 \\ M_{\max}\,\left[\frac{\beta-1}{2-\beta}\,\left(1 - \left(\frac{M_{\min}}{M_{\max}}\right)^{2-\beta}\right)\right] & ,\ \beta \neq 2. \end{cases} \tag{2.14}$$

The performance of the introduced sampling technique and the comparison to the original optimal sampling method (Kroupa et al. 2013) is illustrated and quantified with an exemplary calculation in Schulz et al. (2015, see their Sect. 2.1). It is shown that optimal sampling is not optimal in the sense that it does not lead to the correct total number of SCs, N_{tot}, even if it reproduces the total mass, M_{tot}, and the sampled SCs are distributed according to the parental distribution function. In contrast, the introduced sampling method produced an outcome that is able to resemble the underlying distribution function in terms of $\mathrm{d}N/\mathrm{d}M$ and $M\ \mathrm{d}N/\mathrm{d}M$ and has a total number of SCs, N_{tot}, and a total mass, M_{tot}, which fully agrees with the analytical expectations (Eqs. (2.13) and (2.14)). Thus, the new sampling method was termed improved optimal sampling.

The advantages of the improved optimal sampling are – apart from the fact that it fulfills all of the four conditions stated at the beginning of this section – that the outcome is free of stochastic fluctuations and that the whole sampling can be performed analytically since the antiderivatives of $\mathrm{d}N/\mathrm{d}M$ and $M\ \mathrm{d}N/\mathrm{d}M$ (cf. Eqs. (2.2)–(2.7)) can be calculated analytically as well, which saves computational time. Also, since the underlying concept is so general it can be used to

sample any type of object that can be represented by a distribution function that is a piecewise power law. A practical description is given in Schulz et al. (2015, see their Sect. 2.1).

2.2 Embedded cluster mass function (ECMF)

The ECMF is the mass distribution function of young, embedded SCs that were formed during one star cluster formation epoch (SCFE). Observations suggest that the stellar masses of young SCs are distributed according to a power law with index β:

$$\xi_{\rm ECMF}(M) = \frac{{\rm d}N_{\rm ECMF}}{{\rm d}M} = k\left(\frac{M}{M_{\rm max}}\right)^{-\beta}. \tag{2.15}$$

$M_{\rm max}$ is the stellar upper mass limit for SCs formed during one SC formation epoch, k a normalization constant, and $-\beta$ the slope of the ECMF lying in the range $1.6 \lesssim \beta \lesssim 2.5$ (direct measurements: Zhang & Fall 1999; Bik et al. 2003; de Grijs et al. 2003; Hunter et al. 2003; Lada & Lada 2003; Fall 2004; Gieles et al. 2006a; de Grijs & Anders 2006; McCrady & Graham 2007; de Grijs & Goodwin 2008; Dowell et al. 2008; Whitmore et al. 2010; Chandar et al. 2010, 2011; derived from models: e.g., Kroupa & Boily 2002; Weidner et al. 2004; see also de Grijs et al. 2003, their Table 2, for slopes of the cluster luminosity function for different galaxies).

It is debated whether the ECMF is a pure power law (Whitmore et al. 2007, 2010; Chandar et al. 2010, 2011) or has a fundamental upper limit like a cutoff or an exponential turn-over at the high-mass end, which can be described by a Schechter function (Gieles et al. 2006a,b; Bastian 2008; Larsen 2009; Bastian et al. 2012a,b). A differentiation between the two types is very difficult because of the low number of high-mass SCs (e.g., Bastian 2008; Bastian et al. 2012a). If the ECMF is indeed truncated, Haas & Anders (2010) did not expect the precise shape at the high-mass end to be important. They investigated how the choice of the sampling technique and the index of the ECMF alters the integrated galactic initial mass function (IGIMF) – the analogon of the IGECMF for stars instead of SCs. They pointed out that an exponential turn-down and a truncation of the cluster mass function will have a similar effect on the IGIMF, for which reason the precise shape of the ECMF is not expected to be important.

Bonatto & Bica (2012), for instance, simulated how a Schechter-type initial cluster mass function of galactic GCs evolves due to stellar evolution and dy-

namical mass-loss processes into a present-day mass function for different M/L dependences on luminosity. Interestingly, the most realistic results were obtained for M/L ratios increasing with luminosity – as is observed for GCs – with a truncation mass of $M_{\rm trunc} \approx 10^{10}$ M$_\odot$, which means, effectively a pure power law without an upper limit. On the other hand, there might exist an upper mass limit for SCs since they form out of giant molecular clouds (GMCs) whose mass function is truncated at the high-mass end at least in M33, as reported by Rosolowsky et al. (2007).

Since a completely limitless ECMF is unphysical, it is assumed that there is a theoretical upper mass limit for SCs, $M_{\rm max}$, which is not a fixed value, but depends on the SFR, as derived below. Following Weidner et al. (2004), a lower mass limit for newly born SCs of $M_{\rm min} = 5$ M$_\odot$ is assumed. The ECMF (Eq. (2.15)) was assumed to be a pure power law ranging from $M_{\rm min}$ to the cutoff mass, $M_{\rm max}$, beyond which SCs cannot be formed. All following derivations are based on the findings from Chap. 2.1, meaning that the same normalization and the new sampling method were used so that all results obtained there are applicable here. The choice of a deterministic sampling technique is motivated by Pflamm-Altenburg et al. (2013) and Kroupa (2015, see also references therein) since a self-regulated rather than a probabilistic or stochastic description of the emergence of an SC population out of a dense molecular cloud is consistent with the data. Thus, the total number of young SCs, $N_{\rm ECMF}$, of one SC formation epoch is given by Eq. (2.13),

$$N_{\rm ECMF} = \int_{M_{\rm min}}^{M_{\rm max}} \xi_{\rm ECMF}(M)\,{\rm d}M = \left(\frac{M_{\rm max}}{M_{\rm min}}\right)^{\beta-1} - 1. \tag{2.16}$$

According to Eq. (2.14), the total stellar mass of a young, embedded SC population, $M_{\rm ECMF}$, formed during one SC formation epoch, is determined by

$$\begin{aligned} M_{\rm ECMF} &= \int_{M_{\rm min}}^{M_{\rm max}} M\,\xi_{\rm ECMF}(M)\,{\rm d}M \\ &= \begin{cases} M_{\rm max}\ (\ln M_{\rm max} - \ln M_{\rm min}) & ,\ \beta = 2 \\ M_{\rm max}\ \left[\frac{\beta-1}{2-\beta}\left(1 - \left(\frac{M_{\rm min}}{M_{\rm max}}\right)^{2-\beta}\right)\right] & ,\ \beta \neq 2. \end{cases} \end{aligned} \tag{2.17}$$

For all following computations the following is assumed for the SC formation process:

1. During one SC formation epoch, all SCs and the stars therein form coevally and represent a single-age SC population. The SC masses of this young

SC population are always distributed according to the ECMF (Eq. (2.15)) within the limits $M_{\rm min}$ and $M_{\rm max}$, implying that the ECMF is fully (or "optimally") populated (Chap. 2.1).

2. The index β of the ECMF does not change with time.

3. An SC formation epoch is of duration δt, which is not a function of time.

4. During an SC formation epoch, the total mass of the young SC population, $M_{\rm ECMF}$, is formed at a constant SFR:

$$M_{\rm ECMF} = {\rm SFR} \cdot \delta t. \tag{2.18}$$

The total mass of one SC population, $M_{\rm ECMF}$, can be calculated from Eq. (2.17) if the lower and upper limit of the SC masses are known. Moreover, knowledge about $M_{\rm ECMF}$ and δt allows extracting the underlying SFR: rearranging Eq. (2.18) using Eq. (2.17) leads to an SFR of

$${\rm SFR} = \begin{cases} \frac{M_{\rm max}}{\delta t} \ (\ln M_{\rm max} - \ln M_{\rm min}) & , \beta = 2 \\ \frac{M_{\rm max}}{\delta t} \ \frac{\beta-1}{2-\beta} \ \left(1 - \left(\frac{M_{\rm min}}{M_{\rm max}}\right)^{2-\beta}\right) & , \beta \neq 2. \end{cases} \tag{2.19}$$

Since $M_{\rm min}$, β, and δt are treated as constant quantities, the SFR (Eq. (2.19)) is determined by $M_{\rm max}$ alone. Because the ECMF is a function of $M_{\rm max}$ and $M_{\rm max}$ is correlated with the SFR, the ECMF implicitly depends on the SFR:

$$\xi_{\rm ECMF}(M) \equiv \xi_{\rm ECMF,SFR}(M_{\rm min} \leq M \leq M_{\rm max}({\rm SFR})). \tag{2.20}$$

Regrettably, the theoretical upper mass limit for SCs of a particular SC formation epoch, $M_{\rm max}$, is very hard to determine. However, the mass of the most massive SC of the same SC formation epoch, $M_{\rm ecl,max}$, can be estimated. The ansatz of the new sampling technique enables relating the theoretical upper mass limit, $M_{\rm max}$, and the mass of the heaviest SC, $M_{\rm ecl,max}$, to each other. In the first condition (Eq. (2.6)), $i = 1$ is assigned to the most massive SC since the SCs become less massive with increasing i (Chap. 2.1), so $m_i = m_1 = M_{\rm max}$

$$1 = \int_{m_2}^{M_{\rm max}} \xi_{\rm ECMF}(M) \, {\rm d}M = \left(\frac{m_2}{M_{\rm max}}\right)^{1-\beta} - 1. \tag{2.21}$$

Solving for m_2 gives

$$m_2 = 2^{\frac{1}{1-\beta}} M_{\max}. \tag{2.22}$$

According to the second condition (Eq. (2.7)), the mass of the most massive SC, $M_{\mathrm{ecl,max}}$, is determined by the integration limits from Eq. (2.21) and replacing m_2 with Eq. (2.22) results in

$$\begin{aligned} M_{\mathrm{ecl,max}} &= \int_{m_2}^{M_{\max}} M\, \xi_{\mathrm{ECMF}}(M)\, \mathrm{d}M \\ &= \begin{cases} (\ln 2)\ M_{\max} & , \beta = 2 \\ \frac{\beta-1}{2-\beta}\left(1 - 2^{\frac{2-\beta}{1-\beta}}\right) M_{\max} & , \beta \neq 2. \end{cases} \end{aligned} \tag{2.23}$$

Inversely, the upper mass limit for SCs of one SC formation epoch, $M_{\max}$, as a function of the observed most massive SC, $M_{\mathrm{ecl,max}}$, reads

$$M_{\max} = \begin{cases} (\ln 2)^{-1}\ M_{\mathrm{ecl,max}} & , \beta = 2 \\ \frac{2-\beta}{\beta-1}\left(1 - 2^{\frac{2-\beta}{1-\beta}}\right)^{-1} M_{\mathrm{ecl,max}} & , \beta \neq 2, \end{cases} \tag{2.24}$$

which allows relating $M_{\mathrm{ecl,max}}$ and SFR to each other by replacing $M_{\max}$ in Eq. (2.19) with Eq. (2.24). From this arises the so-called SFR–$M_{\mathrm{ecl,max}}$ relation:

$$\mathrm{SFR} = \begin{cases} \frac{M_{\mathrm{ecl,max}}}{\delta t \cdot \ln 2}\left(\ln\left(\frac{M_{\mathrm{ecl,max}}}{\ln 2}\right) - \ln M_{\min}\right) & , \beta = 2 \\ \frac{M_{\mathrm{ecl,max}}}{\delta t}\left(1 - 2^{\frac{2-\beta}{1-\beta}}\right)^{-1}\left(1 - \left(\frac{\beta-1}{2-\beta}\left(1 - 2^{\frac{2-\beta}{1-\beta}}\right)\frac{M_{\min}}{M_{\mathrm{ecl,max}}}\right)^{2-\beta}\right), & \beta \neq 2. \end{cases} \tag{2.25}$$

Indeed, observations suggest that $M_{\mathrm{ecl,max}}$ scales with SFR (see Fig. 2.2 below) as found for example by Weidner et al. (2004, see also Randriamanakoto et al. 2013). According to this, during high-SFR episodes SCs of higher masses are formed than at low-SFR episodes. This means in turn that high SFRs are essential for the formation of high-mass SCs. In Chap. 2.5, this SFR–$M_{\mathrm{ecl,max}}$ relation is analyzed to determine the length of one SC formation epoch, δt.

2.3 The concept of the integrated galactic embedded cluster mass function (IGECMF)

Star cluster formation typically continues over more than just one formation epoch, δt. In this framework, it means that for each formation epoch one fully populated ECMF is added to the already existing sample of SCs and that all properties mentioned in Chap. 2.2 apply to each epoch. Here, it is implicitly assumed that it is possible to divide a SC formation episode into a certain number of SC formation epochs of length δt. In this respect, it does not matter whether SC formation takes place continuously or in bursty phases. An observed sample of SCs is thus – unless the SCs are coeval – a superposition of several SC populations, each described by the ECMF. Analogously to the ECMF, this time-integrated mass distribution function is called the IGECMF. The IGECMF reveals how the birth stellar masses of SCs are distributed after a certain SC formation episode, but it does not take into account any changes of the individual SC masses afterward.

The ECMF of each SC formation epoch is determined by an individual $M_{\rm max}$ (cf. Eqs. (2.15) and (2.10)). Since $M_{\rm max}$ is dependent on the SFR (Eq. (2.19), see also Eq. (2.20)), the distribution function of SFRs, called $F(\mathrm{SFR})$, is needed to obtain the IGECMF. It describes the number of SC formation epochs (SCFEs) $\mathrm{d}N_{\rm SCFE}(\mathrm{SFR})$ per SFR interval:

$$F(\mathrm{SFR}) = \frac{\mathrm{d}N_{\rm SCFE}(\mathrm{SFR})}{\mathrm{dSFR}}. \tag{2.26}$$

The IGECMF will arise from the integration of the ECMF over the whole range of SFRs in which the ECMF (Eq. (2.15), see also Eq. (2.20)) is modulated by $F(\mathrm{SFR})$:

$$\xi_{\rm IGECMF}(M) = \int_{\mathrm{SFR}_{\rm min}}^{\mathrm{SFR}_{\rm max}} \xi_{\rm ECMF,SFR}(M)\ F(\mathrm{SFR})\ \mathrm{dSFR}. \tag{2.27}$$

The resulting IGECMF will have a unique shape because $F(\mathrm{SFR})$ carries information about the formation history, which is unique for any galaxy or galaxy cluster. Since the ECMF implicitly depends on SFR (Eq. (2.20)) and the inverse function $M_{\rm max}(\mathrm{SFR})$ cannot be calculated analytically (cf. Eq. (2.19)), the integration of Eq. (2.27) cannot be performed directly. For this reason, $M_{\rm max}$ is substituted for

the integration variable SFR so that Eq. (2.27) becomes

$$\xi_{\mathrm{IGECMF}}(M) = \int_{M_{\mathrm{max}}^{\mathrm{low}}}^{M_{\mathrm{max}}^{\mathrm{up}}} \xi_{\mathrm{ECMF}}(M, M_{\mathrm{max}})\, F(M_{\mathrm{max}})\, \frac{\mathrm{dSFR}}{\mathrm{d}M_{\mathrm{max}}}\, \mathrm{d}M_{\mathrm{max}}, \tag{2.28}$$

with $M_{\mathrm{max}}^{\mathrm{low}}$ and $M_{\mathrm{max}}^{\mathrm{up}}$ being the new limits of the integration over all possible M_{max} corresponding to the lowest and highest SFRs, $\mathrm{SFR}_{\mathrm{min}}$ and $\mathrm{SFR}_{\mathrm{max}}$. The transformation from $F(\mathrm{SFR})$ to $F(M_{\mathrm{max}})$ can be carried out by converting SFR to M_{max} after inverting Eq. (2.19) numerically; the value of the function itself is not affected by this rescaling. The derivatives of Eq. (2.19) are

$$\frac{\mathrm{dSFR}}{\mathrm{d}M_{\mathrm{max}}} = \begin{cases} \frac{1}{\delta t}\ (1 + \ln M_{\mathrm{max}} - \ln M_{\mathrm{min}}) & , \beta = 2 \\ \frac{1}{\delta t}\ \left[\frac{\beta-1}{2-\beta}\ \left(1 - (\beta-1)\left(\frac{M_{\mathrm{min}}}{M_{\mathrm{max}}}\right)^{2-\beta}\right)\right] & , \beta \neq 2. \end{cases} \tag{2.29}$$

The integral in Eq. (2.28) is equivalent to a summation of ECMFs up to their individual M_{max}. $F(M_{\mathrm{max}})$ determines how often each ECMF contributes to the overall IGECMF since it reveals how often the corresponding SFR occurred.

The derivations here are focused on how the birth stellar masses of all SCs ever formed will be distributed after an SC formation episode of arbitrary duration. This mass distribution is computed by purely superposing the single-age SC populations of many SC formation events, allowing the SFR to change with time. Thus, neither stellar nor dynamical evolution leading to mass loss or even to the destruction of SCs are taken into account here. However, these effects and the impact of the tidal field must be accounted for as soon as the derived SC mass distributions are compared to observed mass distributions of SCs. This will be done in detail in Chap. 3.2.

2.4 From the ECMF to the IGECMF – an exemplification

Since the subject matter of the previous sections is very theoretical, the interrelation between the ECMF and the IGECMF is exemplified with Fig. 2.1 in this section. It is sketched how different star formation activities (top panels, labeled "a") influence the ECMFs (middle panels, labeled "b") and thereby shape the IGECMF (bottom panels, labeled "c"). A double-logarithmic scale is used so that the power-law ECMFs appear as straight lines.

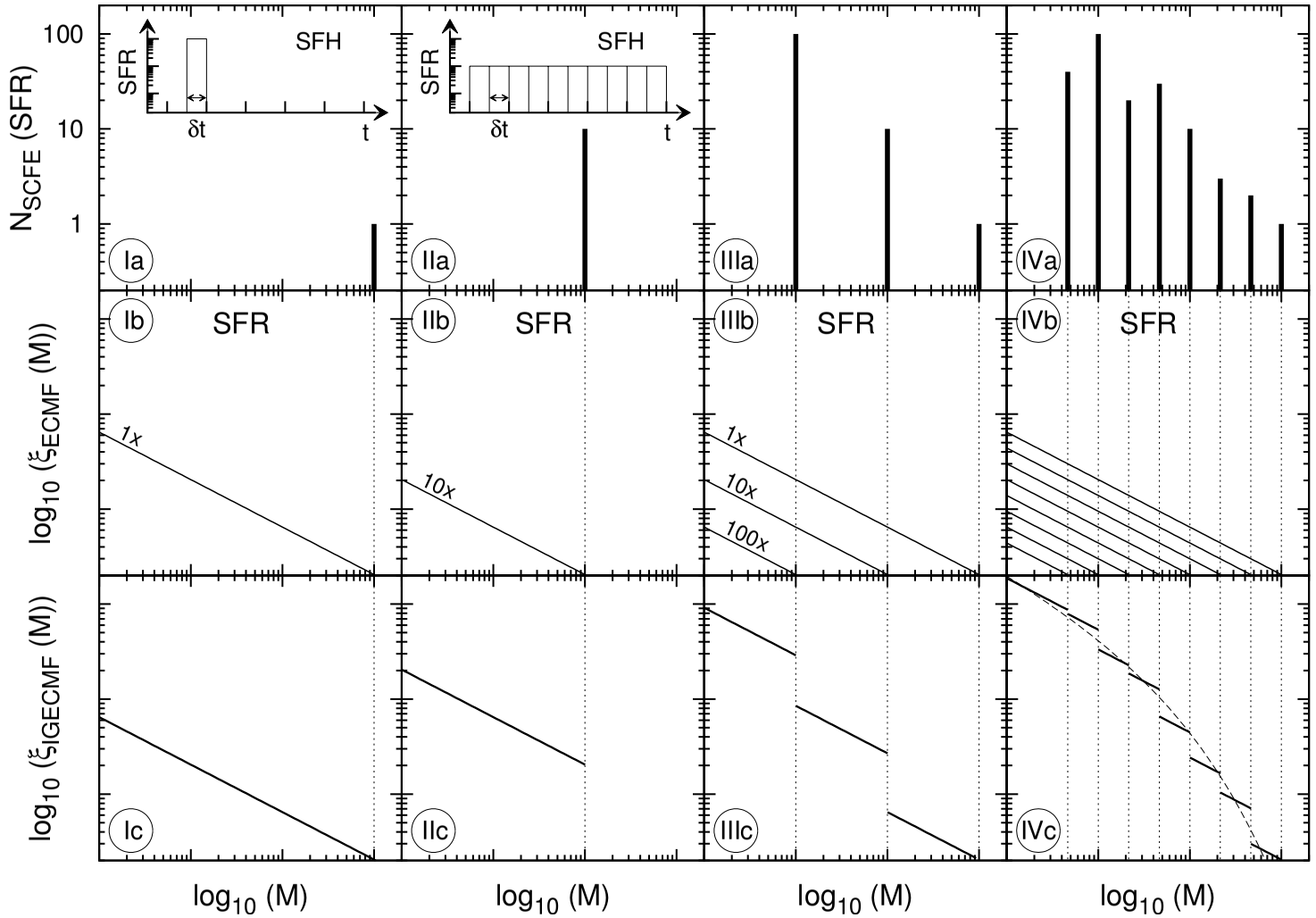

Figure 2.1: Sketch of how different star formation activities (top panels, "a") influence the ECMFs (middle panels, "b") and thereby shape the IGECMF (bottom panels, "c") for four exemplary cases (Cols. I–IV) according to the superposition principle.

Starting with the easiest case (I), there is exactly one SC formation epoch of length δt at a relative high SFR (Ia). Converting this SFR to its respective $M_{\rm max}$ (vertical thin dotted line in panel Ib) visualizes up to which mass the corresponding ECMF is populated once – since only one formation epoch occurred (Ib). Thus, the respective IGECMF (Ic) is equal to the ECMF (Ib) since just one ECMF contributed.

In the second case (II), the SFR remains constant at a medium level over ten SC formation epochs, each of duration δt (IIa). Again, converting the SFR to its respective $M_{\rm max}$ defines the ECMF (IIb), which is populated ten times in total. Thus, the corresponding IGECMF (IIc) is shifted upward by a factor of ten and is truncated sharply at $M_{\rm max}$, which is lower than in the first case (I).

From examples (I) and (II) it becomes clear that, on the one hand, the level of the SFR is relevant since it determines the upper mass limit of the ECMF, and on the other hand, that how often this particular SFR appeared constitutes how often the corresponding ECMF contributes to the IGECMF. This is exemplified in the third case (III), where SC formation takes place at different SFRs and each SFR appears a certain number of times (IIIa). Each SFR has its own respective ECMF, which is populated the number of times the SFR occurred (IIIb): the ECMF corresponding to the lowest SFR is populated one hundred times, while the ECMF belonging to the highest SFR is populated just once. According to the superposition principle, the IGECMF (IIIc) is composed of all contributing ECMFs. The summation has to be carried out in the mass ranges separated by the thin dotted lines by taking into account how often each ECMF occurred: in the highest mass range, only the ECMF corresponding to the highest SFR has to be considered, while in the lowest mass range all ECMFs contribute. Thus, one observes jumps in the IGECMF (IIIc).

The most realistic case is presented in the last column (IV). As in (IIIa), SC formation takes place at different SFRs and a different number of times (IVa), which defines how often each corresponding ECMF will be populated (IVb). Superposing all these ECMFs – each multiplied by the number of formation epochs of the respective SFR – leads to the IGECMF (IVc). Since the summation has to be performed separately in each mass range, the IGECMF exhibits jumps, as in the case before (IIIc).

If even more SC formation epochs occur at SFRs lying between the considered ones (IVa), even more but smaller jumps will appear in the IGECMF. It will develop a curved shape, as indicated by the dashed line (IVc), meaning that it becomes steeper toward the high-mass end. It has been shown in Schulz et al. (2015, their Fig. 9) that the superposition of power-law ECMFs each generated

during one SC formation epoch yields IGECMFs with a Schechter-like turn-down at the high-mass end if the SFR changed over time. Interestingly, such a steepening towards the high-mass end in the SC mass distribution has already been detected observationally (e.g., Hilker 2009a).

2.5 Determining the star formation duration δt using the SFR–$M_{\rm ecl,max}$ relation

The SFR–$M_{\rm ecl,max}$ relation originates from a relation between the global SFR of a galaxy and the brightest SC in the V band and was found by Larsen (2002). Later, Adamo et al. (2011) investigated the same properties of massive young SCs in blue compact galaxies and found them to lie slightly above the upper end of the Larsen relation. Moreover, Randriamanakoto et al. (2013) observed a similar relation in the near-infrared for the brightest super star clusters (SSCs) in luminous infrared galaxies.

In an analysis based on Larsen (2002), Weidner et al. (2004) showed the brightest SC to be the most massive young SC in most cases, even though the M/L-ratio of a stellar population depends highly on its age. They converted the SFR-brightest SC relation to the SFR–$M_{\rm ecl,max}$ relation and analyzed it for dwarf and spiral galaxies. Their data (young, most massive SCs ($M_{\rm ecl,max}$) vs. current, galaxy-wide SFR, taken from Larsen 2002; Weidner et al. 2004; Larsen 2009; provided by C. Weidner, priv. comm.) are replotted in Fig. 2.2 and confirm a correlation between the SFR and $M_{\rm ecl,max}$. A typical error estimate is plotted in the bottom right corner. On the x-axis, the calibration of the SFR as a function of the infrared flux is the main contributor to the error, while on the y-axis the uncertainties mostly originate from converting the luminosity of a SC into a mass with an assumed M/L-ratio that strongly depends on the age of the SC (C. Weidner, priv. comm., see also Weidner et al. 2004).

Apparently, there is some spread in the data, particularly above the relation. These data points mostly belong to dwarf and irregular starburst galaxies (Billett et al. 2002; Larsen 2002). Several explanations have been suggested for this offset: Weidner et al. (2004) argued that an intense star formation activity in a dwarf galaxy may be halted once a very massive SC has formed (the "quenching" hypothesis). The feedback of this SC may heat the surrounding dense gas and prevent further star formation. This scenario was supported by Bastian (2008) based on a study of NGC 1569, a dwarf-irregular (post) starburst galaxy. Ac-

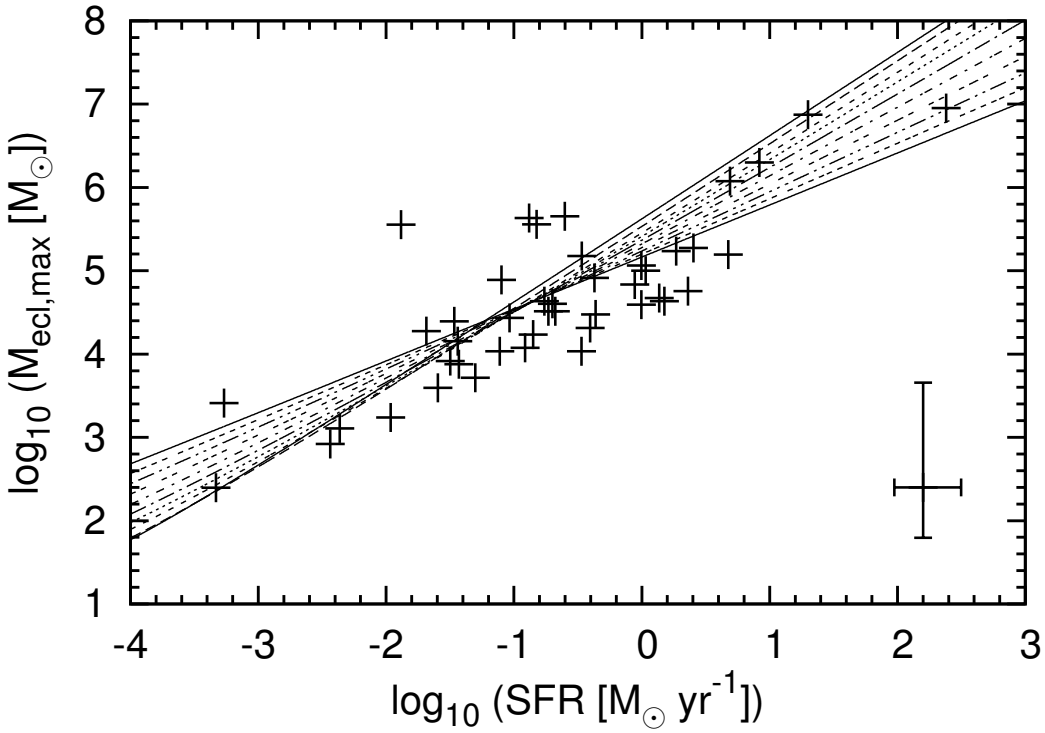

Figure 2.2: $M_{\rm ecl,max}$ vs. galaxy-wide SFR (replotted from Weidner et al. (2004), including new data points). The curves are least-squares fits according to the SFR–$M_{\rm ecl,max}$ relation (Eq. (2.25)) with the fitting parameter δt for all β between 1.5 (steepest curve) and 2.6 (shallowest curve) in steps of 0.1. The curves for β = 1.6, and 1.8 are omitted. A typical error estimate is indicated in the bottom right corner.

cording to the quenching hypothesis, the outlying data points may be located at incorrect positions in the diagram: the SFR might have dropped significantly after the formation of these SCs, for which reason the data points would have to be horizontally shifted to the right since they formed at higher SFRs and may lie in the area of the other measurements.

On the other hand, for the Milky Way (MW) galaxy and the Large Magellanic Cloud (LMC), Fukui et al. (1999) suggested that the stronger gravitational field in the MW compared to the LMC leads to a stronger fragmentation of molecular clouds, for which reason the MW is able to form solely open SCs. In contrast, the weaker gravitational field of the LMC allows the formation of more populous SCs. More generally, Billett et al. (2002) proposed that dwarf galaxies are able

to form massive SSCs due to the absence of shear. Weidner et al. (2010) investigated how shear forces act on GMCs in dwarf and spiral galaxies. They found that the presence of shear prevents GMCs to collapse into dense SSCs in spirals, while in dwarfs the lack of rotational support allows the formation of SSCs. Thus, dwarf galaxies would be able to form more massive SCs than spirals at the same SFR and therefore lie above the mentioned SFR–$M_{\rm ecl,max}$ relation. This would be equivalent to $\xi_{\rm ECMF}(M)$ deviating from the canonical form (Eq. (2.15)) for some dwarf galaxies.

To begin, all data points are included, but it is examined below how the analysis is influenced when the four data points lying above the relation in Fig. 2.2 with $M_{\rm ecl,max}$ between 10^5 $M_\odot$ and 10^6 $M_\odot$ and $\log_{10}({\rm SFR}) < 0$ are excluded. These data points belong to measurements in NGC 1705, NGC 1569, the Small Magellanic Cloud, and the LMC, viewed from left to right. However, assuming that these data points are placed at the correct positions, this would require an SC formation timescale of at least 10 Myr according to a simple estimate using Eq. (2.18).

The length of one SC formation epoch, δt, was determined by fitting the SFR–$M_{\rm ecl,max}$ relation (Eq. (2.25)) to all data points using the least-squares method. Since δt might vary with β, a fit for each β was performed separately in the range from 1.5 to 2.6 in steps of 0.1. Figure 2.2 shows the fitted curves through the data points. The steepest curve corresponds to $\beta = 1.5$, the shallowest curve to $\beta = 2.6$. For purposes of clarity, the curves belonging to $\beta = 1.6$, and 1.8 are omitted.

Clearly, δt increases with increasing β, ranging from 0.4 Myr to 186 Myr (Table 2.1, Col. 2), as visualized by the crosses in the upper panel of Fig. 2.3. A physical explanation might be that it takes longer to populate an ECMF with a large β than an ECMF with a small β due to the larger number of SCs for a given $M_{\rm max}$ (cf. Eq. (2.16)). In addition, the reduced $\chi^2_{\rm red}$ values are extracted from the fit analysis (Table 2.1, Col. 3) and indicated by crosses in the lower panel of Fig. 2.3. Regarding $\chi^2_{\rm red}$, the most probable combinations of β and δt are those for $\beta \lesssim 2$. Toward larger β, $\chi^2_{\rm red}$ increases but does not exceed unity.

For comparison, the same fitting analysis is applied to the SFR–$M_{\rm ecl,max}$ data set (Fig. 2.2) excluding the above mentioned four data points lying above the relation. The resulting length of one SC formation epoch, δt, can be viewed in Col. 4 in Table 2.1 and is represented by filled circles in the upper panel of Fig. 2.3. It emerges that the values for δt are somewhat lower than the previous fitting results (cf. Cols. 2 and 4 in Table 2.1, Fig. 2.3). This is anticipated since δt can be found in the denominator of the SFR–$M_{\rm ecl,max}$ relation (Eq. (2.25)). Consequently, an increasing δt induces the fitting function to shift downward in Fig. 2.2. However, fitting Eq. (2.25) to the data without the outliers already places this function

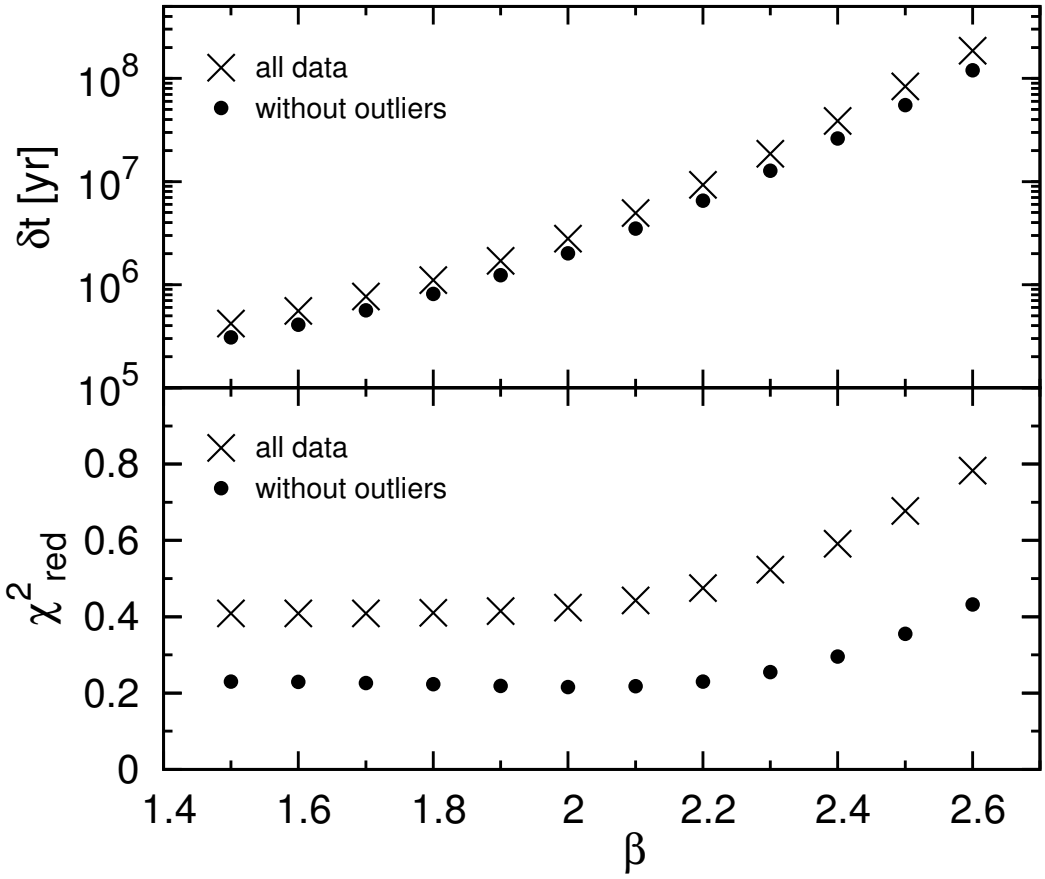

Figure 2.3: Duration of one SC formation epoch, δt, (upper panel) and the reduced $\chi^2_{\rm red}$ (lower panel) as determined from the fitting in Fig. 2.2 with (crosses) and without the four outliers (filled circles) for each β. The values can be found in Table 2.1.

slightly below the previous fits since the outliers lie above the actual relation. Thus, δt is smaller than before. Moreover, the removal of the outliers leads to a smaller spread in the remaining data set and therefore to lower reduced $\chi^2_{\rm red}$ values than in the previous fitting. This becomes clear from the lower panel of Fig. 2.3, where the obtained $\chi^2_{\rm red}$ values are marked with filled circles, and from comparing Cols. 3 and 5 in Table 2.1.

The theoretical star formation timescale of about 10 Myr follows from the calculation of the Jeans time in molecular clouds (e.g., Egusa et al. 2004). This value has been widely adopted (e.g., Billett et al. 2002; Weidner et al. 2004;

Table 2.1: Duration of one SC formation epoch, δt, and the reduced $\chi^2_{\rm red}$ as determined from the least-squares fits in Fig. 2.2 for each β (Col. 1). In Cols. 2 and 3 all data points are used while in Cols. 4 and 5 the four data points lying above the relation in Fig. 2.2 (with 10^5 M$_\odot \lesssim M_{\rm ecl,max} \lesssim 10^6$ M$_\odot$) are excluded. All values are visualized in Fig 2.3.

β	δt [Myr]	$\chi^2_{\rm red}$	δt [Myr]	$\chi^2_{\rm red}$
1.5	0.42	0.409	0.31	0.230
1.6	0.55	0.409	0.41	0.229
1.7	0.77	0.409	0.56	0.226
1.8	1.11	0.410	0.81	0.223
1.9	1.70	0.414	1.24	0.219
2.0	2.80	0.424	2.01	0.216
2.1	4.94	0.443	3.51	0.218
2.2	9.31	0.475	6.51	0.230
2.3	18.57	0.524	12.75	0.255
2.4	38.77	0.591	26.09	0.296
2.5	83.77	0.677	55.19	0.355
2.6	185.82	0.782	119.79	0.432

Maschberger & Kroupa 2007). In simulations performed by Bonnell et al. (2006), star formation occurs within 2 Myr, while the surrounding cloud disperses on a timescale of 10 Myr.

There have been various attempts to estimate the timescale of SC formation observationally: from analyzing GMCs in the LMC, Fukui et al. (1999) estimated SC formation to proceed in a few Myr and a typical lifetime of a molecular cloud of about 6 Myr. Likewise in the LMC, Yamaguchi et al. (2001) found that SCs are actively formed over roughly 4 Myr and the host molecular clouds completely dissipates in about 10 Myr after the onset of SC formation. Another approach to observationally estimate the SC formation timescale is to measure the offset between Hα, emitted through recombination of hydrogen ionized by newly born massive stars, and CO, a tracer of molecular gas which is observed in star-forming spiral arms. Star formation times derived in this way by Egusa et al. (2004, 2009) range from 4 to 28 Myr, whereas half of the measurements lie between 11 and 14 Myr. Similarly, Tamburro et al. (2008) compared images of spiral galaxies in HI from cold gas and 24 μm from warm dust heated by UV and find shorter timescales between 1 and 4 Myr.

Combining the results from theory, simulations, and observations, suggests that the formation of an SC population through the formation and the dispersal of their birth molecular clouds occurs galaxy-wide on a timescale between at least a few Myr and at most a few 10 Myr. The fitting results for δt, the duration of one SC formation epoch, which match these estimates, are highlighted in light gray, while the most probable values are shaded slightly darker in Table 2.1. Additionally, observed values for β, the index of the ECMF, are presented in light gray, while the values found most frequently are highlighted somewhat darker. As one can see immediately, the colored entries in the two columns overlap over almost the full range. This demonstrates the reliability of the analytically derived SFR–$M_{\rm ecl,max}$ relation (Eq. (2.25)) since it naturally connects – without any adjustment – the empirical estimates of the two independent quantities β and δt in combination with the SFR vs. $M_{\rm ecl,max}$ data from Weidner et al. (2004). Note that this finding is virtually independent of whether outliers are excluded or not (cf. Table 2.1).

Since there has not been a definitive statement about the four outliers and the outliers do not change the results much, none of them is excluded. Thus, for all further calculations the values for δt are used as given in Col. 2 in Table 2.1. However, it is not expected that the further analysis will depend much on whether the outliers are excluded or not since in both cases the values for δt are similar and increase with β in a similar way (cf. Cols. 2 and 4 in Table 2.1, Fig. 2.3). Moreover, it is assumed that the SFR–$M_{\rm ecl,max}$ relation, extrapolated to higher values, holds true.

Chapter 3

Distribution of star formation rates during the rapid assembly of NGC 1399 as deduced from its globular cluster system

After having introduced all necessary ingredients for the further analysis, I proceed with the application of the IGEMCF principle to observational data. This chapter is structured such that I start with the introduction of the observed globular cluster (GC) and ultra-compact dwarf (UCD) samples in Fornax in Chap. 3.1. Thereafter it is explained how their present-day mass function needs to be corrected to describe their mass function at their birth in Chap. 3.2. It follows the decomposition of the latter into individual SC populations in Chap. 3.3 from which the distribution of required SFRs can be deduced using the SFR–$M_{\rm ecl,max}$ relation in Chap. 3.4. I continue with a discussion of my analysis in Chap. 3.5. In there, I first focus on the assumptions (Chap. 3.5.1), then critically review the results (Chap. 3.5.2) and finally construe the implications for the formation of the host galaxy NGC 1399 (Chap. 3.5.3).

This chapter is based on a paper that has been published as Schulz, C., Hilker, M., Kroupa, P., & Pflamm-Altenburg, J. 2016, A&A, 594, A119, with the title "Distribution of star formation rates during the rapid assembly of NGC 1399 as deduced from its globular cluster system".

3.1 Observed GC and UCD samples in Fornax

The majority of GCs and UCDs in the Fornax galaxy cluster are very old (age estimates range between roughly 8 and 13.4 Gyr; Forbes et al. 2001; Kundu et al. 2005; Hempel et al. 2007; Firth et al. 2009; Chilingarian et al. 2011; Francis et al. 2012). Above an age of about 5 Gyr, age measurements become less certain because isochrones lie closer to each other in line index diagrams the higher the probed age. Thus, it is impossible to tell when exactly each individual object formed. However, even if firm conclusions about the formation history of each and every GC/UCD cannot be drawn, it is at least possible to make a statistically reliable statement about the formation of the whole GC/UCD system based on the sheer number of objects: Gregg et al. (2009) estimated 11 100 ± 2400 GCs/UCDs within 320 kpc around NGC 1399. However, only a fraction of them have been spectroscopically confirmed so far. As shown by Mieske et al. (2012, their Fig. 3), very many GCs and UCDs are confirmed within a radius of 50 kpc around NGC 1399 thanks to a high spatial coverage. At radii between 50 kpc and 100 kpc, there are fewer, while beyond 100 kpc the number of confirmed GCs/UCDs decreases strongly. This is not only caused by their decreasing radial number density profile (e.g., Schuberth et al. 2010, their Fig. 15) but also due to an incomplete spatial coverage inherent to spectroscopic surveys. Thus, it is not straightforward to obtain a statistically representative sample around NGC 1399. This is achieved here by combining a spectroscopic and a highly confident photometric sample.

Spectroscopic sample ("spec" sample): The first sample contains 935 of the brightest GCs/UCDs around NGC 1399. This sample is a compilation of many different studies (Hilker et al. 1999b; Drinkwater et al. 2000; Mieske et al. 2002, 2004, 2008; Bergond et al. 2007; Hilker et al. 2007; Firth et al. 2007; Gregg et al. 2009; Schuberth et al. 2010; Chilingarian et al. 2011, and Puzia & Hilker (priv. comm.)). Since GCs/UCDs have roughly the same age, they probably have a comparable M/L-ratio, for which reason these brightest objects are also among the most massive in the central Fornax galaxy cluster. Because of their brightness, they are particularly suitable for spectroscopic analyses. The membership of these objects is confirmed by measurements of their radial velocity, extracted from their spectra. For this reason, the spectroscopic sample offers very reliable number counts at the high-mass end of the GC/UCD mass function.

Photometric sample ("phot" sample): The second sample contains 6268 objects, mostly GCs, around NGC 1399 and other central Fornax cluster galaxies based on HST/ACS observations, allowing resolved images of the GCs, reported by Jordán et al. (2007). Since much fainter objects can be detected through photometry, GCs of much lower masses can be identified. Thus, as a result of the large number of objects and the lower mass limit, the photometric sample is statistically more reliable than the spectroscopic sample, particularly in the intermediate- and low-mass regime.

The masses of the GCs/UCDs were determined as follows: for the photometric sample, the g- and z-band photometry was converted into M_V and $V-I$ based on the calibration by Peng et al. (2006). For the spectroscopic sample, V, $V-I$, or $C-R$ were used to obtain the latter quantities. The individual GC/UCD masses were then determined using the obtained M_V and $V-I$, a Kroupa IMF (Kroupa 2001) and a mass-to-light ratio, M/L_V, derived from models by Maraston (2005), where for each GC/UCD a 13 Gyr old simple stellar population (SSP) was assumed (Misgeld & Hilker 2011; Mieske et al. 2013; Puzia et al. 2014). For comparison, the individual GC/UCD masses were also determined based on M/L_V obtained from models by Bruzual & Charlot (2003), also assuming a 13 Gyr old SSP and using the same M_V and $V-I$, but a Chabrier IMF (Chabrier 2003). For the analysis, masses are used as calculated from Maraston (2005) and it is shown below how much these masses differ from those determined based on Bruzual & Charlot (2003).

Since the investigations here are focused on the surroundings of NGC 1399, it is necessary to apply distance cuts: the objects in the spectroscopic sample are concentrated around NGC 1399, but their distribution becomes patchy beyond 85 kpc. To obtain a spatially homogeneous sample, only objects within that radius are included, which led to a selection of 801 objects. On the other hand, the photometric sample comprises objects that are located around other galaxies in the Fornax galaxy cluster more than 1 Mpc away from NGC 1399 and thus not associated with it. To obtain a statistically representative sample, only objects that are within a radius of 160 kpc around NGC 1399 are taken into consideration since this region is dominated by the central giant elliptical. This led to a selection of 2326 objects in the photometric sample.

Applying these distance cuts, the resulting cumulative GC/UCD mass functions where the GC/UCD masses were determined from models by Maraston (2005) with a Kroupa IMF are shown in Fig. 3.1 for the spectroscopic sample in orange and for the photometric sample in purple. In the same colors but with

thin dashed lines, the same mass distributions are shown for the masses determined based on Bruzual & Charlot (2003) with a Chabrier IMF. Figure 3.1 shows that the models by Bruzual & Charlot (2003) predict somewhat lower masses than models by Maraston (2005): on average, the objects are 20% and 15% less massive in the spectroscopic and photometric sample, respectively. In conclusion, the uncertainty in the mass determination is around 20% on average even if there are cases where the masses deviate by up to one third.

To obtain an accurate number distribution across the whole mass range, the two samples have to be combined. This needs to be done in such a way that each sample covers the mass regimes where it is more reliable. Consequently, the spectroscopic sample should determine the high-mass end of the GC/UCD mass function, while the photometric sample should define the shape of the GC/UCD mass function at the intermediate- and low-mass range. To achieve this, it is necessary to scale the photometric sample such that it matches the spectroscopic sample. The scaling must be done in a mass region that is not too high, where the photometric sample is inaccurate, but not too low where the spectroscopic sample becomes incomplete. This overlapping region is determined by demanding the same slope for both mass functions. As indicated by the vertical lines in Fig. 3.1, the interval [6.55, 6.75] is selected for the spectroscopic sample where the corresponding cumulative mass function has a slope of 3.3 and the interval [6.4, 6.6] for the photometric sample with a similar slope of 3.4. These two slopes are included in Fig. 3.1 with blue dashed lines. At $\log_{10}(M/M_\odot) = 6.6$, there are 100 objects in the spectroscopic sample, while the photometric sample contains 29 GCs, leading to a scaling factor of $100/29 \approx 3.5$ with an error of about 0.7 when only considering Poisson noise. When the scaling point is chosen at a lower mass of $\log_{10}(M/M_\odot) = 6.55$, 6.5, or 6.45 a scaling factor of 3.2, 3.1, or 2.9, respectively, is obtained because the spectroscopic mass function flattens toward lower masses. Choosing the scaling point at $\log_{10}(M/M_\odot) = 6.65$, 6.7, or 6.75 gives a scaling factor of 4.5, 5.2, or 4.7, respectively, because the mass function of the photometric sample falls off steeply above $\log_{10}(M/M_\odot) = 6.6$. Therefore, the requirement is set that the scaling has to be done at a mass where the slopes of the spectroscopic and photometric mass functions are similar.

The two samples are combined in the following way: the high-mass part above $\log_{10}(M/M_\odot) = 6.6$ (indicated by a vertical arrow in Fig. 3.1) is defined by the spectroscopic sample, while the intermediate- and the low-mass part emerges from shifting the photometric sample upward by the factor 3.5. The similar slope of the two samples in the overlap region leads to a smooth transition. The combined cumulative mass function of GC/UCD is represented by a red dotted line in

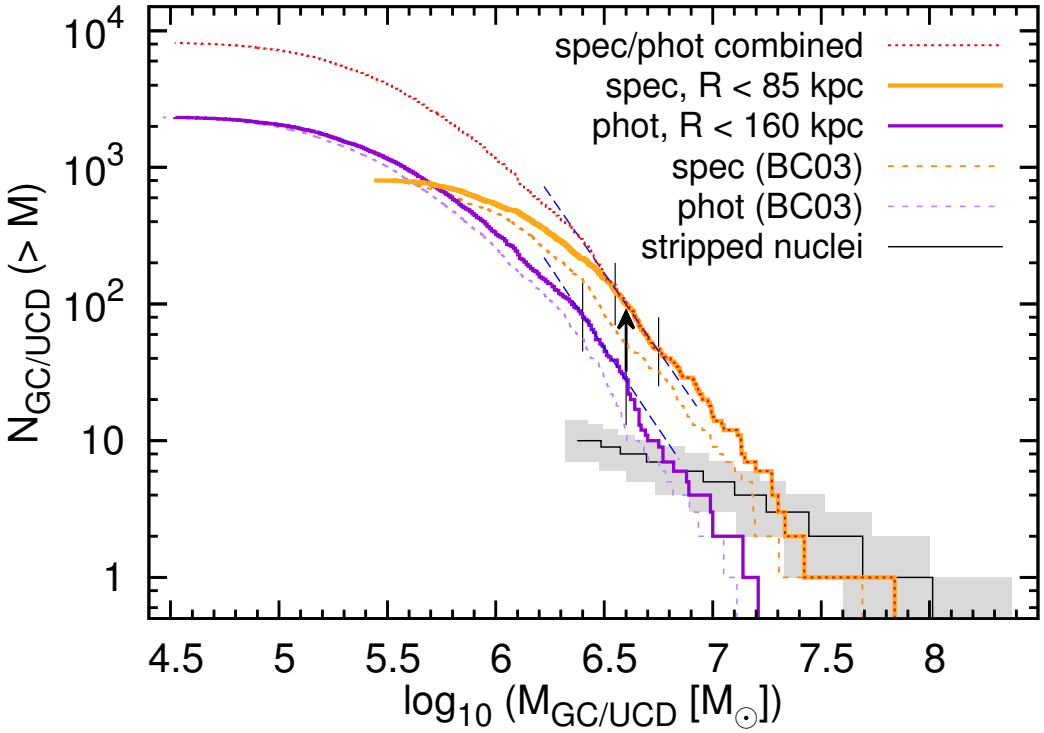

Figure 3.1: Cumulative mass function of the spectroscopic (orange continuous line, spec sample) and the photometric sample (purple continuous line, phot sample). In both cases, the masses were determined from SSP models by Maraston (2005). The scaling with the factor 3.5 was applied at $\log_{10}(M/M_{\odot}) = 6.6$ (vertical arrow) where the slopes (dashed blue lines) of the cumulative functions are almost the same, resulting in the combined cumulative GC/UCD mass function (red dotted line). For comparison, the dashed thin orange and purple lines show the cumulative mass function of the spectroscopic and the photometric sample, respectively, where the masses have been calculated based on Bruzual & Charlot (2003). The black line represents the cumulative distribution of stripped nuclei as determined by Pfeffer et al. (2014), while the standard deviation area is colored in gray (see Chap. 3.3).

Fig. 3.1 and consists of 8143 objects. This is well within the estimate by Gregg et al. (2009) because a smaller region is probed. However, based on two different approaches, Dirsch et al. (2003) expected 6100 ± 770 and 6800 ± 950 objects, respectively, within 83 kpc (i.e., almost the same spatial region). Compared to their estimates, the combined sample includes slightly more objects.

3.2 Correction of the observed GC/UCD sample

To determine which distribution of SFRs has led to the formation of the observed GC/UCD sample, the individual mass of each GC/UCD at the time of its birth is required. Thus, it is necessary to correct the observed mass function for all aspects that resulted in a change of the individual GC/UCD masses. The main contributors are

1. mass loss due to stellar evolution,
2. mass loss due to dynamical evolution, and
3. elimination of objects that are not the result of an SC formation process.

There are many elaborate models that treat the evolution of SCs as a function of various parameters, such as the orbit of the SCs, the concentration factor, and/or the Roche-lobe filling conditions (e.g., Lamers et al. 2010, 2013; Alexander & Gieles 2012; Alexander et al. 2014; Brockamp et al. 2014). The corrections of the first two aspects were based on the relatively simple model by Lamers et al. (2005a). Their model appears to be very suitable for the purposes here since it requires only a handful of ingredients. This is important because the current knowledge about the combined GC/UCD sample is limited: based on their photometric properties, a mass estimate exists for all objects. Additionally, spectra have been taken for the most luminous and therefore most massive objects, from which the radial velocity and some internal properties of these objects can be deduced. From photometry and/or spectroscopy, the metallicities and the ages of the GCs/UCDs are known. Typically, they lie between -2 dex and $+0.5$ dex, while the metal-poor and the metal-rich sub-populations peak at rougly -1.5 dex and -0.5 dex, respectively. Moreover, the projected 2D distance to the center of NGC 1399 is known for each object.

However, external properties such as the 3D position in the galaxy cluster, the absolute velocity, or the parameters of the orbit are not known for any object of the sample. This means in turn that it is not possible to apply corrections regarding the internal and external dynamical evolution to each object individually without making assumptions, in particular for the lower mass tail of the combined GC/UCD sample, where number counts were extrapolated by scaling. Applying corrections based only on assumptions will lead to relatively large uncertainties that might prevent drawing reliable conclusions about the formation of the observed GC/UCD sample. To avoid this, corrections are only applied based on accessible properties of the sample.

The model by Lamers et al. (2005a) allows to correct for stellar evolution and the disruption of SCs in tidal fields, the two most important contributions regarding the mass loss of SCs. Using Eq. (7) from Lamers et al. (2005a), the initial mass of each SC, $M_{\rm initial}$, is calculated as a function of its present mass, $M_{\rm now}$, and its age, t:

$$M_{\rm initial}(M_{\rm now}, t) = \left[\left(\frac{M_{\rm now}}{M_\odot}\right)^\gamma + \frac{\gamma t}{t_0}\right]^{1/\gamma} \frac{1}{\mu_{\rm ev}(t)}. \tag{3.1}$$

Here, $\gamma = 0.62$ and t_0 can be expressed as $t_0 = (t_4/660)^{1/0.967}$, where t_4 is the total disruption time of an SC with an initial mass of $10^4 M_\odot$. These parameters carry the information related to the mass loss due to tidal disruption for an SC of any mass. The mass loss due to stellar evolution is described by $\mu_{\rm ev}(t)$, which is the mass fraction of an SC with initial mass $M_{\rm initial}$ that is still bound at age t. With Eqs. (2) and (3) in Lamers et al. (2005a), $\mu_{\rm ev}(t)$ reads

$$\mu_{\rm ev}(t) = 1 - 10^{(\log(t) - a_{\rm ev})^{b_{\rm ev}} + c_{\rm ev}}, \tag{3.2}$$

where $t > 12.5$ Myr must be fulfilled. Since the GCs/UCDs to have an assumed age of $t = 13$ Gyr (Chap. 3.1), the requirement is easily complied with. The parameters $a_{\rm ev}$, $b_{\rm ev}$, and $c_{\rm ev}$ characterize the mass loss by stellar evolution and depend on the metallicity, Z. The values of $a_{\rm ev}$, $b_{\rm ev}$, and $c_{\rm ev}$ can be found in Table 1 in Lamers et al. (2005a). A metallicity of -0.8 dex on average is assumed for the whole GC/UCD sample, that means $10^{-0.8} Z_\odot = 0.00269$ with $Z_\odot = 0.017$ (e.g., Grevesse & Sauval 1998) and 0.00212 for a newer estimate $Z_\odot = 0.0134$ (Asplund et al. 2009, see also references therein), respectively. According to these numbers, the closest match is $Z = 0.0040$, for which the parameters read $a_{\rm ev} = 7.06$, $b_{\rm ev} = 0.26$, and $c_{\rm ev} = -1.80$.

The only ingredient that is not determined so far is t_0, which can be derived from t_4. Which would be a good estimate for the total disruption time of a 10^4 $M_\odot$ SC around the giant elliptical NGC 1399? t_4 has been determined for M51, M33, the solar neighborhood, and the Small Magellanic Cloud by Lamers et al. (2005b, see their Table 1). Their values for t_4 vary between $10^{7.8}$ yr and $10^{9.9}$ yr. Their Table 1 and their Fig. 3 show that t_4 decreases with increasing ambient density, $\rho_{\rm amb}$, meaning that SCs are destroyed more easily in denser environments. This relationship is also found theoretically: based on N-body simulations by Portegies Zwart et al. (1998, 2002, PZ) and Baumgardt & Makino (2003, BM), Lamers et al. (2005b) showed in their Fig. 2 the dependence of t_4 on $\rho_{\rm amb}$, and two predicted lines that pass through the data points of each set of simulations. These two relations can be approximated by

$$\text{PZ}: \quad \log(t_4) = -0.5\log(\rho_{\rm amb}) + 8.5 \tag{3.3}$$
$$\text{BM}: \quad \log(t_4) = -0.5\log(\rho_{\rm amb}) + 8.9. \tag{3.4}$$

This correlation was used to determine the parameter t_4, which requires the ambient density profile around NGC 1399. Moreover, the above two relations also allow to estimate the uncertainty of t_4.

The ambient density around NGC 1399 was assessed by using Fig. 22 of Schuberth et al. (2010) where different approximations of the cumulative mass distribution of NGC 1399 as a function of the radius are shown. The effect on t_4 was investigated based on the three models labeled R1, R2, and a10. These models were selected because they represent the full range of possible solutions to the observed mass distribution (see Fig. 22 in Schuberth et al. 2010). Their mass profiles emerge from the following model parameters:

$$\text{R1}: \quad \rho_{\rm s} = 0.0085\ M_\odot {\rm pc}^{-3}, \quad r_{\rm s} = 50\ {\rm kpc}, \tag{3.5}$$
$$\text{R2}: \quad \rho_{\rm s} = 0.0065\ M_\odot {\rm pc}^{-3}, \quad r_{\rm s} = 50\ {\rm kpc}, \tag{3.6}$$
$$\text{a10}: \quad \rho_{\rm s} = 0.0088\ M_\odot {\rm pc}^{-3}, \quad r_{\rm s} = 34\ {\rm kpc}, \tag{3.7}$$

where $r_{\rm s}$ is a core radius and $\rho_{\rm s}$ the central density. The two models R1 and R2 were taken from Richtler et al. (2008). For all these models, the corresponding profile of the ambient density as a function of the radius is expressed by Eq. (10) in Richtler et al. (2004), where $\zeta = 1$ was used (cf. Eqs. (11) and (12) in Richtler et al. 2004 with Eq. (3) in Richtler et al. 2008):

$$\rho_{\rm amb} = \frac{\rho_{\rm s}}{(r/r_{\rm s})(1 + r/r_{\rm s})^2}. \tag{3.8}$$

Using this equation, the ambient densities, $\rho_{\rm amb}$, were calculated at different radii for the three models R1, R2, and a10 (Eqs. (3.5)−(3.7)) and converted into lifetimes of a $10^4\ M_\odot$ SC, t_4, according to the two above relations (Eqs. (3.3) and (3.4)). All results can be found in Table 3.1. The underlaid gray shading of individual entries in the table shows how strongly that particular value for t_4 would influence the correction of the observed GC/UCD mass function: the stronger the effect, the darker the color (dark gray: $t_4 < 5$ Gyr, medium gray: 5 Gyr $< t_4 <$ 10 Gyr, light gray: 10 Gyr $< t_4 < t_{\rm Hubble}$).

Table 3.1 lists the resulting values for t_4 , which shows that it depends much on the radius, the model used for the ambient density, and its conversion to t_4. First,

t_4 increases with increasing radius, which is expected since the ambient density decreases at the same time. Second, compared to t_4 values of the mass model R2, the corresponding t_4 values of the mass model R1 are lower, while the t_4 values of the mass model a10 are higher. This is also expected because the mass in model R1 increases more strongly with radius than model R2, while the increase of mass with radius is weaker for model a10 (cf. Fig. 22 in Schuberth et al. 2010). The t_4 values of the different models reflect that the ambient density changes with radius in the same way as the mass does. Third, the conversion relation BM generally leads to longer lifetimes of 10^4 $M_\odot$ SCs than the relation PZ. This is caused by the larger second term in the equation (cf. Eqs. (3.3) and (3.4)).

Interestingly, the conversion relations influence the resulting t_4 values much more strongly than the choice of the mass model: the relation BM gives values for t_4 more than twice as high as those from the relation PZ, while the differences in t_4 for the three mass models R1, R2, and a10 are on a 10% level that slightly increases with radius, r. Thus, the primary influence determining the value of t_4 is the conversion relation and not the mass model. The shortest survival time of a 10^4 $M_\odot$ SC of about 2 Gyr is obtained near the center of NGC 1399 with mass model R1 and the conversion relation PZ, while a similar SC can outlast several Hubble times in the outskirts of NGC 1399.

Apparently, there is no one single value for t_4 that comprises all information about the dynamical evolution of the observed GCs/UCDs that have a variety of masses and distances to the center of NGC 1399. Therefore, different approximations for t_4 were used to see how much the analysis depend on that parameter. The first assumed value was $t_4 = 15$ Gyr, which is somewhat longer than the Hubble time. In this case, the correction term (Eq. (3.1)) is dominated by mass loss due to stellar evolution, making the mass loss due to dynamical evolution negligible for all GCs/UCDs. Guided by the t_4 values based on the conversion relation by PZ in Table 3.1, in two comparison cases the lifetime of a 10^4 $M_\odot$ SC was assumed to be $t_4 = 6$ Gyr and $t_4 = 3$ Gyr. In particular, $t_4 = 3$ Gyr will allow to determine how strongly this parameter influences the analysis. In this case, the strongest effect on the combined GC/UCD mass function is expected to occur at its low-mass end.

The last aspect listed in the enumeration in the beginning of this section, the elimination of objects that did not form in a typical SC formation process such as stripped nuclei of dwarf galaxies or merged super SCs, is also a challenge. As a first approach, it was assumed that all objects in the combined GC/UCD sample are genuine SCs, but two alternatives were also investigated in Chap. 3.3.

Now, all ingredients for the mass correction are available: all parameters were chosen as described above, while for t_4 the values 3, 6, and 15 Gyr were assumed.

Table 3.1: Determination of the ambient density, $\rho_{\rm amb}$, based on three different mass models (R1 in Cols. 2–4, R2 in Cols. 5–7, and a10 in Cols. 8–10.) to estimate the lifetime of a $10^4\ M_\odot$ SC, t_4, based on two different conversion relations (PZ in Cols. 3, 6, 9, and BM in Cols. 4, 7, 10) as a function of the radius r (Col. 1).

r [kpc]	$\rho_{\rm amb}^{\rm R1}$ [$M_\odot$pc^{-3}]	$t_4^{\rm PZ}$ [Gyr]	$t_4^{\rm BM}$ [Gyr]	$\rho_{\rm amb}^{\rm R2}$ [$M_\odot$pc^{-3}]	$t_4^{\rm PZ}$ [Gyr]	$t_4^{\rm BM}$ [Gyr]	$\rho_{\rm amb}^{\rm a10}$ [$M_\odot$pc^{-3}]	$t_4^{\rm PZ}$ [Gyr]	$t_4^{\rm BM}$ [Gyr]
10	$2.95 \cdot 10^{-2}$	1.84	4.62	$2.26 \cdot 10^{-2}$	2.11	5.29	$1.79 \cdot 10^{-2}$	2.37	5.94
20	$1.08 \cdot 10^{-2}$	3.04	7.63	$8.29 \cdot 10^{-3}$	3.47	8.72	$5.93 \cdot 10^{-3}$	4.11	10.31
30	$5.53 \cdot 10^{-3}$	4.25	10.68	$4.23 \cdot 10^{-3}$	4.86	12.21	$2.82 \cdot 10^{-3}$	5.96	14.97
40	$3.28 \cdot 10^{-3}$	5.52	13.87	$2.51 \cdot 10^{-3}$	6.32	15.86	$1.58 \cdot 10^{-3}$	7.96	19.99
60	$1.46 \cdot 10^{-3}$	8.27	20.76	$1.12 \cdot 10^{-3}$	9.45	23.74	$6.52 \cdot 10^{-4}$	12.38	31.10
80	$7.86 \cdot 10^{-4}$	11.28	28.34	$6.01 \cdot 10^{-4}$	12.90	32.40	$3.33 \cdot 10^{-4}$	17.34	43.55
100	$4.72 \cdot 10^{-4}$	14.55	36.55	$3.61 \cdot 10^{-4}$	16.64	41.80	$1.93 \cdot 10^{-4}$	22.78	57.23
130	$2.52 \cdot 10^{-4}$	19.91	50.01	$1.93 \cdot 10^{-4}$	22.77	57.19	$9.89 \cdot 10^{-5}$	31.79	79.86
160	$1.51 \cdot 10^{-4}$	25.77	64.73	$1.15 \cdot 10^{-4}$	29.47	74.02	$5.74 \cdot 10^{-5}$	41.73	104.81

The present mass of each GC/UCD in the combined sample (Fig. 3.1) is inserted into Eq. (3.1) to determine its initial mass. The corrected cumulative mass functions can be viewed in Fig. 3.2, where they are drawn by blue, purple, and orange continuous lines for the t_4 values 3, 6, and 15 Gyr, respectively, while the present-day mass function is indicated by a red dotted line. The corrected mass functions represent the mass distributions of the GCs/UCDs at their birth and were used as the starting point to determine their formation history.

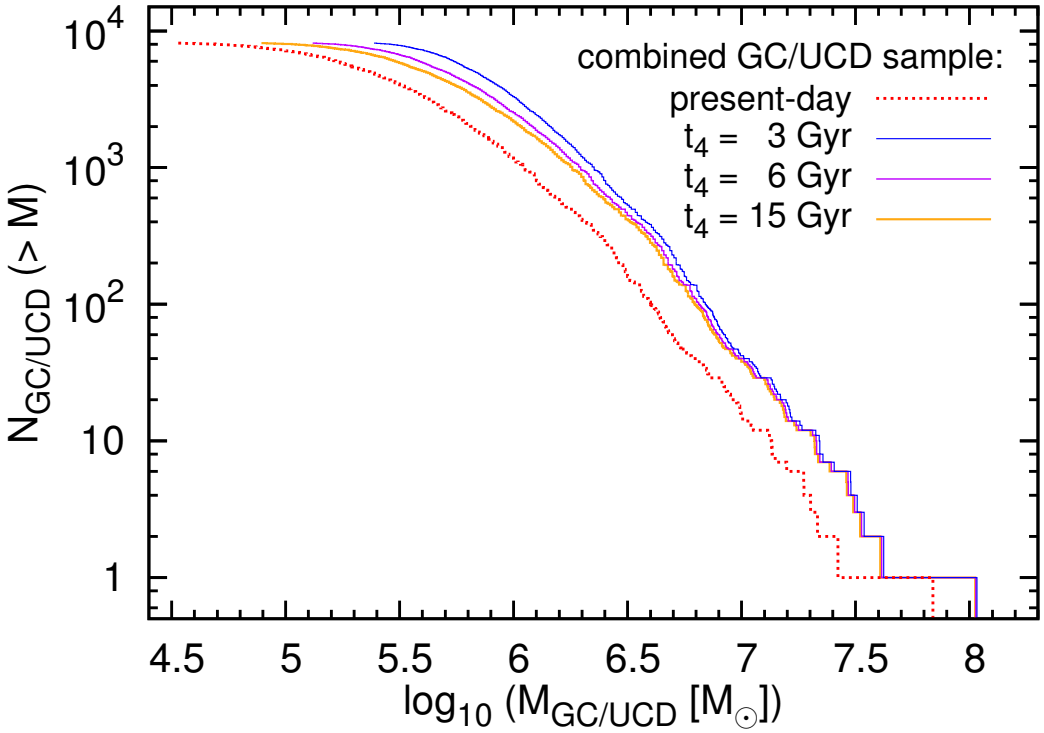

Figure 3.2: Present-day (red dashed line) and natal cumulative mass functions (continuous lines) of the combined GC/UCD sample. The latter resulted from the former based on Eq. 3.1 with different values for the lifetime of a 10^4 $M_\odot$ SC, t_4 (blue: t_4 = 3 Gyr, purple: t_4 = 6 Gyr, orange: t_4 = 15 Gyr). All other parameters are described in Chap. 3.2.

As compared to the present-day mass function, the corrected mass functions are generally shifted to higher masses since SCs only lose but do not gain mass in the course of time, although under some circumstances further mass growth is possible (Bekki & Mackey 2009; Pflamm-Altenburg & Kroupa 2009). Apparently, the shift at the high-mass end is almost the same for all three values of t_4:

the reason is that essentially all mass loss is caused by stellar evolution, which depends on the mass itself, while the tidal field, and thus t_4, has almost no influence on high-mass SCs. On the other hand, the shift at the low-mass end differs significantly among the three mass functions: as compared to high-mass SCs, SCs of lower masses are much more strongly exposed to the tidal field and thus lose a higher fraction of their mass, while the relative amount of mass lost due to stellar evolution remains the same. Thus, when correcting for mass loss, those SCs gain more mass relative to their present mass than high-mass SCs. This results in a steepening of the mass function at the low-mass end with decreasing t_4.

Note that this correction cannot tell how many SCs have been destroyed in the course of time: it is only possible to trace back the mass loss of GCs that still exist, but there is no indication of how many GCs have been destroyed over the same period of time. The number of destroyed SCs should increase with decreasing mass and decreasing t_4. On the other hand, the lifetime of any SC must have been longer in the past since the mass of the central elliptical NGC 1399 and the surrounding Fornax galaxy cluster increased to its present-day value, leading to longer survival times in the past. It is not obvious to which extent these two effects might counteract each other. Nevertheless, since destroyed GCs are not accounted for, this implies that in particular the number of low-mass GCs is probably underestimated.

Probably, the real natal mass function of the GC/UCD sample lies somewhat above the cumulative mass function described by $t_4 = 15$ Gyr. The latter represents the case of minimum requirement where all GC/UCD are corrected for stellar evolution while the influence of the tidal field becomes negligible. At least toward higher masses, the mass function with $t_4 = 3$ Gyr can be interpreted as a rough upper limit: for this mass function it is assumed that all objects have such a low t_4 value. This clearly is an overestimate since only the innermost objects have low t_4 values, and these objects only constitute a fraction of the whole sample. Still, at higher masses, the mass function is probably relatively accurate since the influence of t_4 is marginal and the complete dissolution of high-mass GCs/UCD is unlikely. However, in particular toward smaller masses, even the mass function with $t_4 = 3$ Gyr is probably an underestimate since destroyed GCs are not accounted for and low-mass GCs are particularly susceptible to dissolution (e.g., Fall & Rees 1977; Okazaki & Tosa 1995; Elmegreen 2010). Bearing this in mind, all three corrected GC/UCD mass functions from Fig. 3.2 are used in the following section to determine the variation this introduces in the distribution of necessary SFRs.

3.3 Replication and Decomposition of the GC/UCD sample

After restoring the natal cumulative mass function of the combined GC/UCD sample (Fig. 3.2), it is now possible to decompose it into separate SC populations, each described by the ECMF (Eq. (2.15)). Here, the fact is used that the most massive SCs in the combined GC/UCD sample can only be formed during epochs with a high SFR, while low-mass SCs can be formed during any SC formation epoch (Eq. (2.19)). Thus, to determine which and how many formation epochs contributed to the overall GC/UCD mass function, the replication has to start at the high-mass end:

1. The (remaining) most massive SC, $M_{\rm SC,max}$, in the combined GC/UCD sample is selected and converted into the theoretical upper mass limit, $M_{\rm max}$, after rearranging Eq. (2.23).

2. $M_{\rm max}$ determines the required SFR through Eq. (2.19).

3. The normalization constant k (Eq. (2.10)) depends on $M_{\rm max}$, which is known from step 1, and β, which is varied in the range [1.7, 2.5]. With β, k, and $M_{\rm max}$, the ECMF (Eq. (2.15)) is fully determined. Note that β also sets the length of one SC formation epoch, δt (see Table 2.1 in Chap. 2.5; cf. also Cols. 2 and 3 in Table 3.2 in Chap. 3.5).

4. The derived ECMF is integrated downward to calculate the individual SC masses, M_i, of the population formed in the same epoch as the most massive SC, $M_{\rm SC,max}$, selected in step 1. For this, the optimal sampling technique (Chap. 2.1) is used. Since the ECMF is a pure power law, the individual SC masses can be evaluated analytically by using Eqs. (2.6) and (2.7).

5. All generated SCs (also from previous runs, if existing) are accumulated and sorted according to their mass. Starting at the high-mass end, the masses of the most-massive, second most-massive, third most-massive, and so on, SC of the generated and observed distributions are compared pairwise. A deviation of up to five percent is accepted. The comparison stops as soon as the mass of an SC in the generated sample is less massive than tolerated, as compared to its counterpart in the observed sample. This SC in the observed sample is regarded as the remaining most massive SC in the observed GC/UCD sample. Thereafter the loop restarts.

A schematic plot of this procedure is shown in Fig. 3.3 for an ECMF with $\beta = 1.8$: the procedure generates a first population (lower blue colored area) of SCs based on the most massive SC, $M_{\mathrm{SC,max,1}}$, in the observed GC/UCD sample corrected for mass loss (see Chap. 3.2; red continuous line). From the mass $M_{\mathrm{SC,max,2}}$ on, the first generated sample starts to deviate from the observed distribution. Thus, this SC in the observed sample is regarded as the most massive of the second population (light blue colored area). The first and second population together start deviating from the observed sample at the SC with the mass $M_{\mathrm{SC,max,3}}$, which is regarded as the most massive SC of the third population (upper blue colored area). This iteration process is repeated until all generated SCs together replicate the observed GC/UCD sample as precisely as possible. Based on these and all following $M_{\mathrm{SC,max},i}$, the required SFR for each formation epoch is determined according to steps 1 and 2 in the above enumeration.

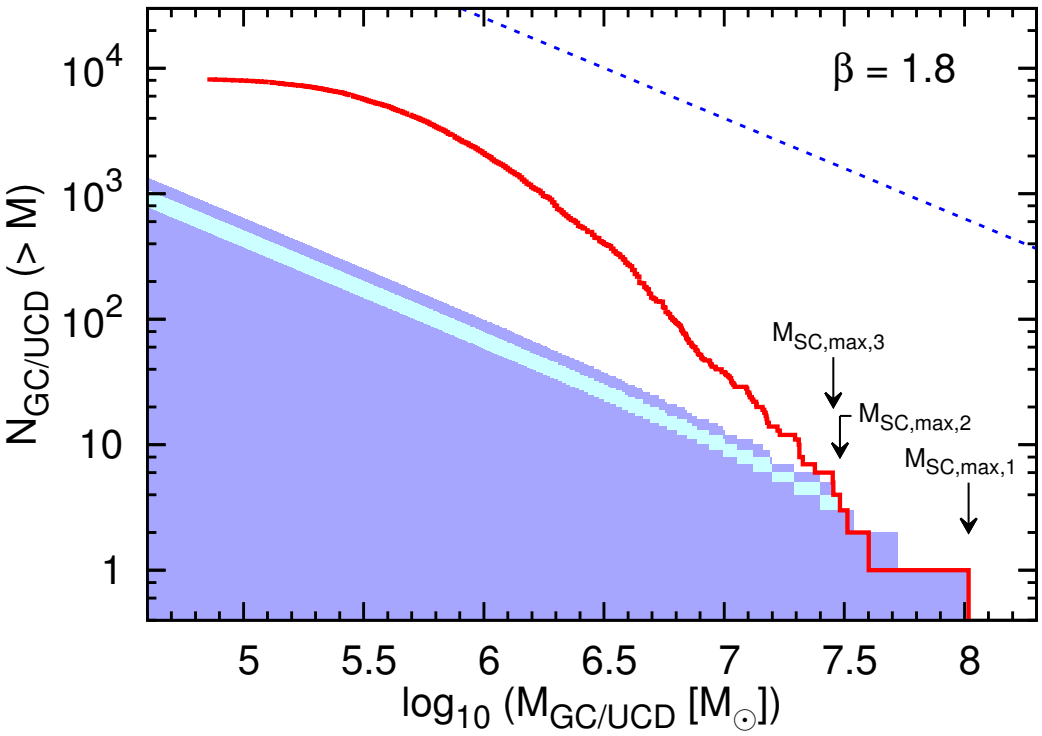

Figure 3.3: Decomposition of the observed GC/UCD cumulative mass distribution corrected for mass loss (see Chap. 3.2; red continuous line) into individual SC populations (colored areas). Here, the first three populations for an ECMF with $\beta = 1.8$ are shown. The most massive object of each population is indicated.

The goal is to reproduce the overall shape of the GC/UCD mass distribution and not to generate exact matches between individual SCs. To achieve this, a five percent tolerance was allowed as mentioned above. Moreover, when comparing the SCs in the generated and the observed sample pairwise from high to low masses, it was kept track of the difference in mass for each SC pair. For instance, sometimes an SC in the generated sample was more massive than its counterpart in the observed sample. When this occurred, it was checked whether the following SC pair could compensate for this mass difference, and only then an SC pair with a mass difference above the mentioned tolerance was accepted.

The reason for the above approach, the tolerance and taking care of the mass difference, is threefold: first, in this way, the generation of an SC population is prevented if an SC of similar but slightly lower mass is available in the generated sample. This is done to avoid an overproduction of SCs that potentially do not have an equally massive counterpart in the observed GC/UCD sample since there is no way of excluding an SC from the generated sample once it is generated. Second, this ensures that the total mass in the generated and the observed sample are similar. This allowed to obtain a match between the generated and observed sample in terms of the shape of the GC/UCD mass distribution and the total mass in it. Third, the five percent margin introduces some tolerance since the optimized sampling distributes the masses of SCs very smoothly. However, it was also tested how the choice of a margin of five percent influences the analysis. For comparison, no tolerance at all (i.e., 0 %) and a margin of twenty percent was assumed. When comparing the results, it turned out that in the former case slightly more and in the second case slightly fewer SCs are generated. The influence is minor but is discussed in Chap. 3.5.1.

As a first approach, all GCs/UCDs in the combined sample were treated as being formed in an SC formation process. The replication of the observed GC/UCD sample is shown for β in the range between 1.7 and 2.5 in Fig. 3.4. The initial GC/UCD mass distributions are represented by continuous lines (blue: t_4 = 3 Gyr, purple: t_4 = 6 Gyr, orange: t_4 = 15 Gyr), while the corresponding generated distributions are drawn with short dashed lines of the same color. The green dashed lines indicate the underlying ECMF. The mass distributions generated with no margin and a twenty percent margin exhibit slightly more and fewer SCs, respectively. The mass functions themselves look essentially the same apart from the fact that they are slightly shifted upward and downward at the low-mass end, respectively, but have the same slope. To avoid overcrowding the figure, they are not shown because the difference is barely visible owing to the logarithmic scale.

Overall, and in particular for lower β, the above procedure works well: the

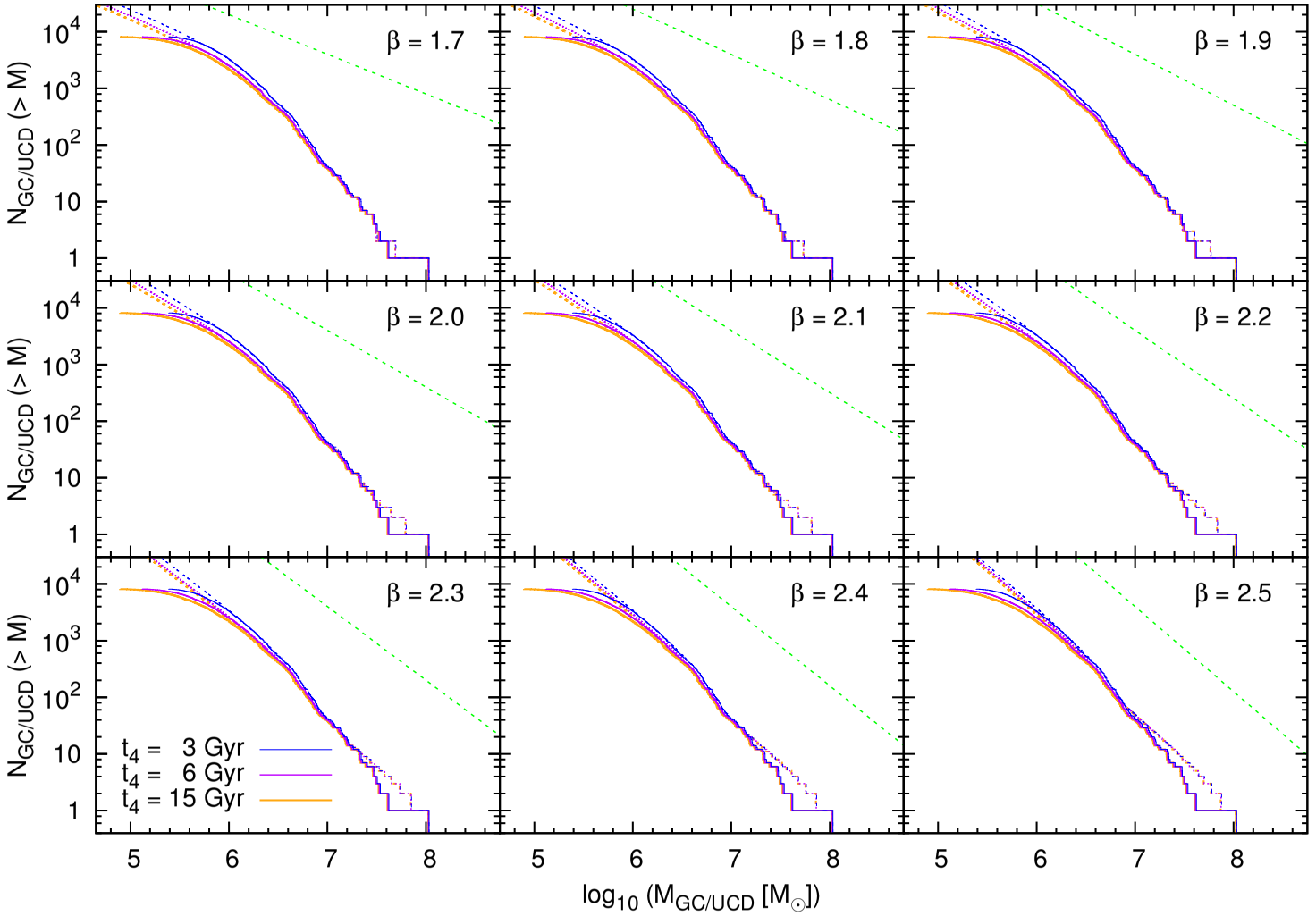

Figure 3.4: Natal GC/UCD cumulative mass functions (continuous lines) together with the replicated ones (short dashed lines) as a function of β (green dashed lines). The color scheme is the same as in Fig. 3.2.

generated distributions match the observed one nearly perfectly. Only at the low-mass end do the samples of generated SCs start to deviate from the observed GCs/UCDs sample because the distribution of GCs/UCDs flattens toward the lower mass end, while the underlying ECMF (green dashed lines in Fig. 3.4) has the same slope throughout. As β increases and the parental ECMFs steepen, the deviation at the low-mass end becomes more prominent. This deviation might be due to the fact that in the observed mass distribution, the survived GCs/UCDs were corrected for stellar and dynamical evolution, but the completely dissolved GCs/UCDs were not taken into account: if the masses of SCs are distributed according to a power law, as assumed here, it was shown in various studies that low-mass SCs are destroyed more efficiently than high-mass SCs (e.g., Fall & Rees 1977; Okazaki & Tosa 1995; Elmegreen 2010). This leads to a Gaussian mass distribution, which is indeed observed around NGC 1399 (see e.g., Hilker 2009a, their Figs. 4 and 5).

Another peculiarity appears in Fig. 3.4: at the high-mass end, the SCs of the generated sample become more massive than their counterparts in the observed GC/UCD sample because β increases, therefore more SCs are drawn from the underlying ECMF. In contrast, the most massive object in the observed sample is more than 2.5 times more massive than the second most massive object, which leads to a substantial mass gap in between.

All of the above findings are independent of the choice of the parameter t_4. The only difference between the generated mass distributions with a certain β is that they are slightly shifted to higher masses in the same way as the low-mass end of the initial mass distributions.

The most massive object in the combined GC/UCD sample is UCD3, which Frank et al. (2011) found to be fully consistent with a massive GC when surveying its internal kinematics. However, it still remains a peculiar object: it has an effective radius of almost 90 pc (Evstigneeva et al. 2007b; Hilker et al. 2007; Frank et al. 2011), which is much larger than the effective radii of typical GCs of about 3 to 5 pc (e.g., Drinkwater et al. 2003; Jordán et al. 2005). Moreover, its surface brightness profile is best fit with a two-component model (Drinkwater et al. 2003; Evstigneeva et al. 2007b), meaning that UCD3 is described best by a core that is surrounded by a halo with effective radii of around 10 and 100 pc, respectively (Evstigneeva et al. 2007b). Such a composition of a core and a halo could be interpreted as a not fully completed stripping process of a more extended object (Evstigneeva et al. 2008). However, the merged star cluster scenario is a possible formation channel as well (Fellhauer & Kroupa 2005). Brüns & Kroupa (2012) emphasized that a core-halo surface brightness profile may also occur after

the merging of SCs based on their simulations on the formation of super SCs in Brüns et al. (2011).

Since UCD3 does not seem to be a typical GC, it was tested how the analysis is influenced when it is removed from the combined GC/UCD sample. Everything else was kept the same and the above method was repeated. There was only one difference compared to the previous run: the agreement at the high-mass end was much tighter. This finding is independent of β, for which reason only the resulting mass distributions for $\beta = 2.0$ are shown in the middle panel of Fig. 3.5, in comparison to the first approach where UCD3 was included (left panel of Fig. 3.5). The overproduction of high-mass SCs clearly disappears completely. The situation at the low-mass end, meaning the dependence on t_4, remains the same as before.

There are two interpretations possible for this finding: first, if it is assumed that UCD3 is a genuine SC, then this would hint at a small β since otherwise between one and three very massive SCs of similar mass should have formed in the same formation event (cf. the overproduction of SCs at the high-mass end for large β in Fig. 3.4). However, this is not observed. It is unlikely that these objects exist because they would be among the brighest UCDs and thus hard to miss observationally. The mass gap between the most massive and the second most massive UCD (cf. the high-mass end of the GC/UCD sample in Fig. 3.4) together with the typical values for β of around 2.0 to 2.3 (e.g., Zhang & Fall 1999; Lada & Lada 2003; Weidner et al. 2004; McCrady & Graham 2007; Chandar et al. 2011) indicate a second possibility: as already suggested by its internal properties, UCD3 cannot be classified as a normal GC that formed in a typical SC formation process. This is regarded as the more probable possibility.

The question is whether UCD3 is not be the only object that does not fall into the category "genuine GC". Unfortunately, no predictions have been made so far regarding the SC mass function for the merged star cluster scenario. However, for the dwarf galaxy threshing scenario, Pfeffer et al. (2016) estimated for a galaxy similar to NGC 1399 a possible number of objects originating from stripping a nucleated dwarf galaxy. Their expected cumulative distribution within 83 kpc around the central galaxy, this means similar to the distance cut applied above, is plotted in black, while the standard deviation area is colored in gray in Fig. 3.1 (J. Pfeffer, priv. comm.). To be consistent, the same mass correction as described in Chap. 3.2 was applied to the stripped nuclei sample by Pfeffer et al. (2016).

In a third approach, it was assumed that this stripped nuclei sample represents those objects in the combined GC/UCD sample (here, the most massive object, UCD3, is included again) that did not form in an SC formation process but are

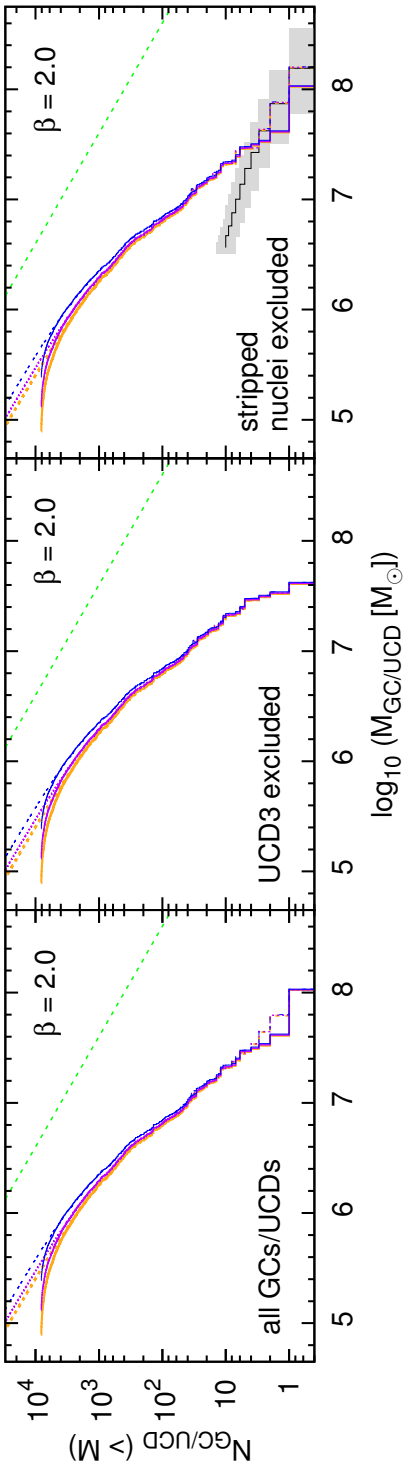

Figure 3.5: Same as Fig. 3.4, but for $\beta = 2.0$ (green dashed lines) for the standard approach (left panel), after excluding UCD3, the most massive object in the sample (middle panel), and using the stripped nuclei sample to account for the most massive objects in the sample (right panel). The color scheme is the same as in Fig. 3.2.

nuclei whose envelope was stripped away. Figure 3.1 shows that the distribution of stripped nuclei accounts for the four most massive objects in the observed sample, which lie within the standard deviation area of the stripped nuclei sample. Consequently, the method needs to reproduce all remaining objects so that finally, the stripped nuclei sample together with the generated sample match the observed distribution of GCs/UCDs. For this, the stripped nuclei were taken as the initial sample and the analysis was repeated as before. The result of this third approach is shown in the right panel of Fig. 3.5 where the same color scheme is used.

The behavior at the low-mass end is essentially the same as in the two cases before: while the observed GC/UCD distribution flattens toward lower masses, the distribution of generated SC continues with the same slope as the underlying ECMF. In addition, the same shift to higher masses appears for shorter t_4. However, at the high-mass end the situation appears to be different from the first approach and similar to the previous one where UCD3 was excluded: since the stripped nuclei sample accounts for the four most massive objects in the observed sample, there is no overproduction of SCs at the high-mass end. Instead, for all β, the algorithm accurately replicates the remaining GCs/UCDs distribution (right panel of Fig. 3.5).

3.4 Distribution of necessary SFRs

Each SC population is characterized by its own individual stellar upper mass limit, $M_{\rm max}$. According to the SFR-$M_{\rm max}$ relation (Weidner et al. 2004; Randriamanakoto et al. 2013), this mass limit can be translated into an SFR under which that SC population formed. Since the observed GC/UCD mass function was decomposed into individual SC populations, it is possible to determine the necessary SFR for each population: for each of the three approaches and for each of the initial GC/UCD mass distributions based on the three different t_4, $M_{\rm max}$ of each SC population is converted into an SFR using Eq. (2.19). This results in nine different cumulative SFR distributions that are plotted in Fig. 3.6 for the different β. These SFR distributions show in a cumulative way how many GC/UCD formation events are necessary above a certain SFR. The color coding is as follows: the resulting SFR distributions for the standard approach, where all GCs/UCDs are kept, are marked in blue. The SFR distributions of the second approach where UCD3 was excluded are drawn in green, while those of the last approach where a sample of stripped nuclei was taken into account are shown in red. Moreover, the thickness of the lines representing the SFR distributions are varied depending on the t_4 value

of the underlying GC/UCD birth mass function: a thick line is used for $t_4 = 3$ Gyr, a medium thick line for $t_4 = 6$ Gyr, and a thin line $t_4 = 15$ Gyr.

The resulting SFR distributions are remarkably similar for each β, regardless of the different approaches and the t_4 value of the underlying GC/UCD birth mass function. The similarity is particularly striking toward smaller β. The details are as follows:

1. The resulting SFRs increase with β and cover a range between log(SFR) $\approx$ 0.5 and 2.5 for $\beta = 1.7$, while for $\beta = 2.5$ the SFR range lies between log(SFR) $\approx$ 2.0 and 4.5. This is mostly independent of the choice of t_4 but depends on the treatment of the highest mass objects (see below). At the same time, the number of required GC/UCD formation events, $N_{\rm SCFE}$, decreases with β from a few thousand events for $\beta = 1.7$ to roughly one hundred events for $\beta = 2.5$. Consequently, the main finding is that the higher β, the higher the SFRs and the fewer formation epochs, $N_{\rm SCFE}$, are needed to build up the entire GC/UCD sample (cf. Cols. 4, 7, and 10 in Table 3.2).

2. As mentioned above, the SFR distributions become less similar with increasing β. In addition to the somewhat broader distribution of the SFR functions toward lower SFRs, the main difference is the distribution of the highest SFRs: in particular for $\beta = 2.5$, for the standard approach (blue lines) obviously only one GC/UCD formation event with a very high SFR is needed, while the other two approaches (green and red lines) require several formation events with a range of slightly lower SFRs. Even though the latter two are treating the objects at the high-mass end differently, their resulting SFR distributions are fairly similar, independent of β.

3. The highest peak SFRs are always obtained for the standard approach (all GCs/UCDs included, blue lines), the lowest peak SFRs always in the case when the stripped nuclei sample is taken into account (red lines). When only UCD3 is excluded (green lines), the peak SFRs are somewhat higher than taking into account the stripped nuclei sample. This is expected since lower SFRs are needed if the highest mass object(s) is excluded or is accounted for by the stripped nuclei sample, respectively.

4. At the low-SFR end, the SFR distributions develop into three different tails, depending on t_4 (thickness of the lines) but independent of how the high-mass end is treated (color). This is particularly visible for a not too high β.

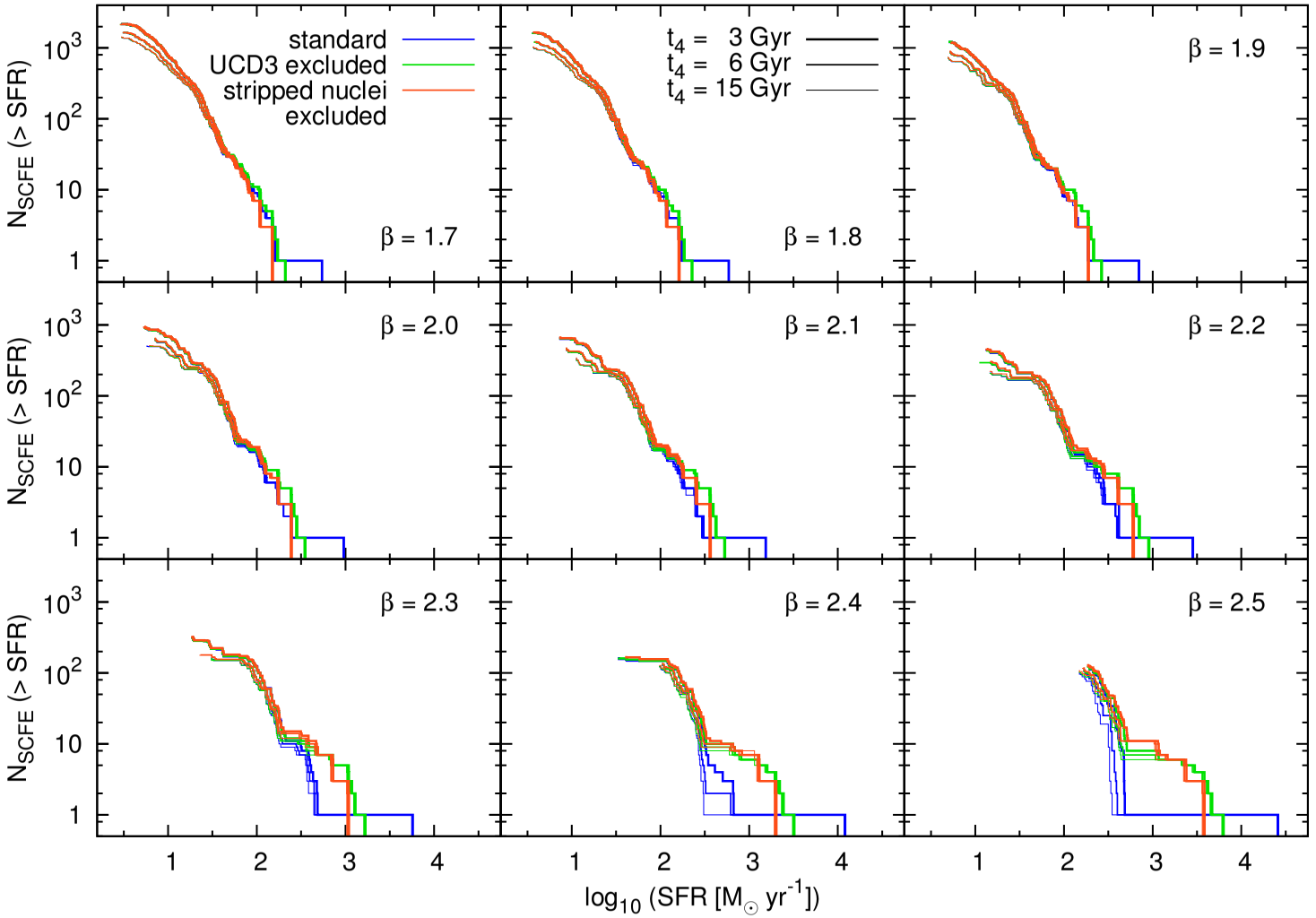

Figure 3.6: Cumulative number of SC formation epochs (SCFEs) as a function of the SFR for the standard approach in blue, for the GC/UCD sample after excluding UCD3 in green, and for taking into account the stripped nuclei sample in red. The thickness of the lines depends on the value of the parameter t_4 (thick lines for t_4 = 3 Gyr, medium thick lines for t_4 = 6 Gyr, thin lines for t_4 = 15 Gyr).

It shows that the number of GC/UCD formation events at the low-SFR end is solely defined by the shape of the low-mass end of the GC/UCD mass function, which itself is determined by t_4, and independent of the treatment of the high-mass end of the GC/UCD mass function. The number of formation events is highest for the smallest t_4 (3 Gyr, thick lines) while the smallest number of formation events is obtained for the highest t_4 (15 Gyr, thin lines). This simply represents the slighty higher/lower masses of the low-mass objects in the observed GC/UCD sample for lower/higher t_4 values, respectively. However, it needs to be considered that the SFR distributions particularly at the low-SFR end only represent a lower limit: the used mass functions are not corrected for destroyed GCs/UCDs, so that more formation epochs and/or higher SFRs might be necessary. Furthermore, the choice of a five-percent margin when replicating the observed GC/UCD mass function also influences the SFR distribution, but only at the low-SFR end since mainly the low-mass end of the mass function changes. For a larger/smaller margin, slightly fewer/more formation epochs and lower/higher SFRs are required. Since the difference is rather small, the resulting SFR distributions are not shown in Fig. 3.6 for clarity (but see Chap. 3.5.1 for a discussion).

Given that the lowest and highest β are only rarely observed and the standard approach, meaning the assumption that even the most massive UCDs formed as a single SC, is not well justified, peak SFRs of between log(SFR) $\approx$ 2.5 and 3.5 are obtained corresponding to values between roughly 300 and 3000 $M_{\odot}\mathrm{yr}^{-1}$. The question is how reasonable these SFRs are for the formation of a rich GC/UCD system like that observed around NGC 1399. Comparing this result to other studies in the literature, it is discussed in Chap. 3.5.3 in detail what the range of SFRs reveals about the formation of NGC 1399 itself.

3.5 Discussion

For this investigation, several assumptions were made that are reviewed in the first part of this section. The second part is continued with a discussion of the results while the third part is focused on the formation of NGC 1399 and its GC/UCD system.

3.5.1 Assumptions

The main assumption is that it is possible to decompose the observed GC/UCD sample into individual SC populations that formed at the same time out of the same molecular cloud. This approach can be applied to the data because it is known that the GCs/UCDs are of similar age. However, it cannot be proven that those GCs/UCDs that are assumed to form a population indeed formed together. The sample is comprehensive, therefore this assumption is not too strong because particularly toward the low-mass end, there are many GCs with similar masses, making them exchangeable. It should be noted that the approach here is of a statistical nature and not a deterministic analysis.

Even though it was taken into account that a part of the UCDs might not originate from an SC formation process, it is not entirely clear whether the bulk of UCDs are compatible with being massive GCs. According to Gregg et al. (2009), the UCDs in the Fornax galaxy cluster form a dynamically distinct population compared to the GC system, with a higher mean velocity and a lower velocity dispersion (see also Mieske et al. 2004). This might indicate a different formation process but does not imply in general that UCDs are not SCs since the most massive SCs have probably formed in the most intense star-forming region and may therefore have a different kinematic signature. Moreover, it has been suggested that only the fainter and less massive UCDs could be genuine GCs while the brightest and most massive ones might have formed by tidal threshing (Mieske et al. 2004; Chilingarian et al. 2011). However, Mieske et al. (2012) restricted the fraction of tidally stripped dwarfs to not more than 50% of UCDs with masses above $2 \cdot 10^6\ M_\odot$ based on statistical considerations. Pfeffer et al. (2014) expected roughly 12 and 20 stripped within 83 kpc and 300 kpc around NGC 1399, whereas almost 150 and 200 GCs/UCDs are observed, respectively (see their Table 2). The contribution for lower masses becomes insignificant. This is well within the constraints set by Mieske et al. (2012). More recently, Pfeffer et al. (2016) estimated that stripped nuclei account for around 40% of the GCs/UCDs above $10^7\ M_\odot$, while for masses between $10^6\ M_\odot$ and $10^7\ M_\odot$ the contribution drops to about 2.5%. As the authors emphasized, this implies that not all of the objects observed at the high-mass end of the GC/UCD mass function can be explained by tidally stripped dwarf galaxies.

If most of the UCDs are indeed of SC origin and not threshed dwarfs, it is not known whether they might have formed in the merged SC scenario (e.g., Fellhauer & Kroupa 2002; Brüns & Kroupa 2012). At the time of formation, the newly born massive SCs were most likely embedded in a high-density environment, allow-

ing a part of these SCs to merge into more massive super SCs. In this case, the masses of the pristine SCs are distributed according to the ECMF (Eq. (2.15)), but the masses of the final SC population might be distributed fairly differently. Consequently, the observed GC/UCD mass function cannot be decomposed into SC populations that are described by the ECMF.

It is not clear whether and how the formation of SCs changes in case of very high SFRs as derived here. The stellar IMF may become top-heavy at high SFRs or high star-forming densities (Gunawardhana et al. 2011; Weidner et al. 2011) and increasing pre-GC cloud-core density (Marks et al. 2012). Furthermore, Narayanan & Davé (2013) found that massive galaxies form the majority of their stars with a top-heavy IMF, but they may experience both top-heavy and bottom-heavy IMF phases during their life. The implications of a top-heavy IMF were studied extensively by Dabringhausen et al. (2009, 2010, 2012) and Murray (2009). Massive stars are then formed more frequently compared to a canonical IMF. They leave behind dark remnants such as neutron stars and black holes, which become visible in X-rays if they accrete matter from a low-mass companion star. Dabringhausen et al. (2012) found that these low-mass X-ray binaries are up to ten times more frequent in UCDs than expected for a canonical IMF.

Weidner et al. (2011) explored the implications of SFRs above $10^3\ M_\odot \mathrm{yr}^{-1}$ on the mass function of SCs and found that either the ECMF becomes top-heavy or no low-mass SCs are formed. If the formation of low-mass SCs is indeed suppressed, the assumption of the lower mass limit, $M_{\mathrm{min}} = 5\ M_\odot$, would not be justified. A change in M_{min} would have an effect on the total mass of each SC population, M_{ECMF} (Eq. (2.17)), and thus also on the SFR (Eq. (2.19)). With a higher M_{min}, M_{ECMF} will become lower so that the necessary SFR will decrease as well. However, it is difficult to quantify this effect since it is not clear what a more realistic lower mass limit would be.

3.5.2 Results

In Chap. 3.1, it was noted that the mass determination strongly depends on the modeled M/L ratio: the mass estimate of GCs and UCDs by Bruzual & Charlot (2003) is on average between 15% and 20% lower than the used one by Maraston (2005). Based on the mass determination, this translates into an uncertainty in the SFR on the same order (cf. Eq. (2.19)), meaning that the derived SFRs are accurate to about 20%.

Moreover, for each run, it was extracted from the analysis how many SC formation epochs (SCFE), N_{SCFE}, are necessary to reproduce the observed GC/UCD

sample, the total time this takes, $t_{\mathrm{SCFE,tot}}$, and the total stellar mass, M_{tot}, formed during that time. All these values can be found in Table 3.2 as a function of the parameter t_4 and the considered approach. The resulting values are similar, independent of the approach, and follow the same trend with increasing β and t_4.

An age of 13 Gyr was assumed for the GC/UCD sample. Even though the age determination becomes more uncertain for older ages, it is known from observations that the vast majority of objects in the sample formed more than 8 Gyr ago (cf. Chap. 3.1). Thus, the total SC formation time, $t_{\mathrm{SCFE,tot}} = N_{\mathrm{SCFE}} \cdot \delta t$ (Cols. 5, 8, 11) with δt, the length of one SC formation epoch, should not exceed several Gyr. This is the case for $\beta \lesssim 2.2$ mostly independent of t_4 and the chosen approach, and agrees nicely with the fact that $\beta \approx 2.0$ is typically found observationally (e.g., Zhang & Fall 1999; Lada & Lada 2003; McCrady & Graham 2007; Chandar et al. 2011).

However, this does not imply that $\beta \gtrsim 2.2$ is ruled out. With increasing β, the corresponding values for δt increase strongly up to about 80 Myr (cf. Col. 3). Observationally, the duration of one SC formation epoch is found to be a few Myr up to a few tens Myr at most (e.g., Fukui et al. 1999; Yamaguchi et al. 2001; Tamburro et al. 2008; Egusa et al. 2004, 2009, see also Chap. 2.5). Apparently, for large β, the estimates for δt are too high, which implies that the total SC formation time, $t_{\mathrm{SCFE,tot}}$, is an overestimate. Furthermore, calculating the total SC formation time through $t_{\mathrm{SCFE,tot}} = N_{\mathrm{SCFE}} \cdot \delta t$ assumes that the SC populations form consecutively. However, it is conceivable that SC formation could occur at the same time but at several separated places. In this case, an individual ECMF would be populated with SCs at each of those places, but the total SC formation time would be shorter than suggested by the formula. The latter might also explain why the found formation timescales are several times longer than the estimate of shorter than 0.5 Gyr according to the downsizing picture (e.g., Thomas et al. 1999; Recchi et al. 2009, see also Chap. 3.5.3).

Today, the total stellar mass of NGC 1399 amounts to $6 \cdot 10^{11}\ M_{\odot}$ within 80 kpc and rises to roughly $10^{12}\ M_{\odot}$ at a distance of 670 kpc (Richtler et al. 2008, their Table 1). Recently, Iodice et al. (2016) derived a total stellar mass of NGC 1399 and its halo of about $6.6 \cdot 10^{11}\ M_{\odot}$, while the stellar mass in the halo amounts to about $4 \cdot 10^{11}\ M_{\odot}$. These estimates set a strict upper limit on the total stellar mass, M_{tot}, that formed during the entire SC formation process.

The M_{tot} columns of each approach in Table 3.2 show that a disagreement with the above limit occurs again for $\beta \gtrsim 2.3$ mostly independent of t_4 and the considered approach. Two things should be mentioned here. First, the above limit regarding the total stellar mass does not imply that this mass is still stored in the

GC/UCD sample today. Apparently, only a tiny portion still is: the present-day mass of the combined GC/UCD sample is about $5 \cdot 10^9$ $M_\odot$, which means about 1% of the total stellar mass of NGC 1399, but a large part of the initially formed SCs dissolved and contributed their stars to NGC 1399 and its halo. Moreover, even the surviving SCs lost part of their mass because of stellar evolution and the loss of stars in the tidal field, which also added to NGC 1399 and its surroundings. Second, the constraint on $M_{\rm tot}$ does not necessarily imply that larger β have to be excluded: as mentioned in Chap. 3.5.1, the lower mass limit, $M_{\rm min}$, was assumed to be 5 $M_\odot$, which might be not well justified since very high SFRs as derived here might prevent the formation of lower-mass SCs.

If indeed $M_{\rm min}$ is underestimated, then the total mass of each SC population, $M_{\rm ECMF}$ (Eq. (2.17)), and therefore also the total mass ever formed in SCs, $M_{\rm tot}$, are overestimated. A higher $M_{\rm min}$ would lower all estimates for $M_{\rm tot}$ in Table 3.2. However, the overestimation of the total mass would be highest for large β since due to the steeper ECMF, more low-mass SCs are formed per high-mass SC.

As mentioned in Chap. 3.3, a margin of five percent was introduced when replicating the observed GC/UCD mass distribution. For comparison, it was checked how no tolerance at all and a margin of twenty percent influences the outcome: the higher the margin, the more the generated GC/UCD mass distributions is shifted downward at the low-mass end. Consequently, when the mass function contains fewer SCs, slightly fewer formation epochs and lower SFRs are required. However, since mainly the low-mass end of the GC/UCD distribution is affected but not the high-mass end, the high-SFR end of the SFR distribution does not change. The most noticeable difference appears in the total mass, $M_{\rm tot}$, of all SCs ever formed: for a larger margin, slightly fewer formation epochs are necessary. Large β are affected the most because for them, the relative number of low-mass SC, produced during every formation epoch, is higher. As compared to a margin of five percent, the difference in $M_{\rm tot}$ varies between +2 % and −8 % for $\beta = 1.7$ and +5 % and −15 % for $\beta = 2.5$ for no tolerance at all and a margin of twenty percent, respectively. To avoid underestimating the total mass, $M_{\rm tot}$, a relative small margin of 5 % was chosen.

In summary, it appears that all cases up to $\beta \approx 2.2$ are in agreement with the conditions set by NGC 1399 mostly independent of t_4, the considered approach, and the choice of the margin. Again, this fits the observations of young SCs well, where usually $\beta \approx 2.0$ is found. However, as already mentioned in Chap. 3.4, the standard approach is not regarded as very well justified because according to it, all GCs/UCDs are assumed to be genuine SCs, even though in numbers, the derived values for $t_{\rm SCFE,tot}$ and $M_{\rm tot}$ do not vary much among the different approaches (cf. Table 3.2).

Table 3.2: The total number of SC formation epochs (SCFEs), $N_{\rm SCFE,tot}$, the total SC formation time, $t_{\rm SCFE,tot}$, and the total stellar mass, $M_{\rm tot}$, formed during that time for the three different approaches as a function of t_4 (Col. 1) and β (Col. 2). These quantities are listed for the standard approach in Cols. 4–6, for the case when the most massive object, UCD3, is excluded in Cols. 7–9, and for an assumed distribution of stripped nuclei in Cols. 10–12. For reference, the length of one SC formation epoch, δt, is listed in Col. 3 as determined in Chap. 2.5 (see Table 2.1).

			Standard approach			UCD3 excluded			Stripped nuclei excluded		
t_4	β	δt [Myr]	$N_{\rm SCFE,tot}$	$t_{\rm SCFE,tot}$ [Gyr]	$M_{\rm tot}$ [10^{10} $M_\odot$]	$N_{\rm SCFE,tot}$	$t_{\rm SCFE,tot}$ [Gyr]	$M_{\rm tot}$ [10^{10} $M_\odot$]	$N_{\rm SCFE,tot}$	$t_{\rm SCFE,tot}$ [Gyr]	$M_{\rm tot}$ [10^{10} $M_\odot$]
3 Gyr	1.7	0.77	2168	1.66	1.98	2178	1.67	1.97	2186	1.67	1.95
	1.8	1.11	1639	1.82	2.52	1646	1.82	2.51	1655	1.83	2.50
	1.9	1.70	1211	2.06	3.56	1218	2.07	3.55	1226	2.09	3.53
	2.0	2.80	934	2.61	5.84	934	2.61	5.83	947	2.65	5.82
	2.1	4.94	671	3.31	11.11	669	3.30	11.08	688	3.40	11.12
	2.2	9.31	451	4.20	24.40	450	4.19	24.40	465	4.33	24.42
	2.3	18.57	323	6.00	61.94	321	5.96	61.86	332	6.17	61.83
	2.4	38.77	167	6.47	166.03	164	6.36	165.56	173	6.71	165.74
	2.5	83.77	121	10.14	516.62	126	10.56	522.28	133	11.14	519.83
6 Gyr	1.7	0.77	1671	1.28	1.55	1672	1.28	1.54	1683	1.29	1.52
	1.8	1.11	1225	1.36	1.96	1221	1.35	1.94	1239	1.37	1.93
	1.9	1.70	899	1.53	2.76	894	1.52	2.74	917	1.56	2.74
	2.0	2.80	651	1.82	4.48	652	1.82	4.47	661	1.85	4.45
	2.1	4.94	470	2.32	8.54	470	2.32	8.51	482	2.38	8.51
	2.2	9.31	287	2.67	18.55	294	2.74	18.62	309	2.88	18.65
	2.3	18.57	165	3.06	46.46	163	3.03	46.23	180	3.34	46.44
	2.4	38.77	135	5.23	140.82	134	5.19	139.86	139	5.39	138.43
	2.5	83.77	113	9.47	448.24	113	9.47	446.09	118	9.89	440.75
15 Gyr	1.7	0.77	1434	1.10	1.35	1436	1.10	1.34	1454	1.11	1.32
	1.8	1.11	1025	1.14	1.69	1025	1.14	1.68	1036	1.15	1.66
	1.9	1.70	741	1.26	2.38	746	1.27	2.37	753	1.28	2.35
	2.0	2.80	507	1.42	3.81	503	1.41	3.78	515	1.44	3.77
	2.1	4.94	339	1.67	7.19	336	1.66	7.16	347	1.71	7.16
	2.2	9.31	212	1.97	15.87	209	1.95	15.85	224	2.08	15.87
	2.3	18.57	146	2.71	42.34	144	2.67	41.96	149	2.77	41.60
	2.4	38.77	125	4.85	127.39	126	4.88	127.29	129	5.00	125.08
	2.5	83.77	102	8.54	403.35	105	8.80	404.42	110	9.22	400.12

3.5.3 Formation of NGC 1399 and its GC/UCD system

Here, possible formation scenarios of elliptical galaxies that can explain SFRs of more than 1000 $M_{\odot}\mathrm{yr}^{-1}$ are discussed. There are suggestions that a massive elliptical might be the result of a merger of two (gas-rich spiral) galaxies (e.g., Lilly et al. 1999; Kilerci Eser et al. 2014) and subsequent accretion of additional galaxies in the course of time. This is based on the observations of so-called (ultra-/hyper-)luminous infrared galaxies ((U/H)LIRGs), which are characterized by a substantial emission in the infrared (LIRGs: $L_{\mathrm{IR}} > 10^{11} L_{\odot}$; ULIRGs: $L_{\mathrm{IR}} > 10^{12} L_{\odot}$; HLIRGs: $L_{\mathrm{IR}} > 10^{13} L_{\odot}$). The energy behind these high luminosities is produced by active galactic nuclei (AGN) and/or an intense starburst (e.g., Carico et al. 1990; Condon et al. 1991) and then re-radiated in infrared wavelengths. Observations show that the relative contribution of the AGN and the starburst component to the IR emission is a function of the luminosity: LIRGs and low-luminosity ULIRGs are mostly powered by a starburst, while high-luminosity ULIRGs and HLIRGs are dominated by an AGN (e.g., Veilleux et al. 1999; Nardini et al. 2010).

In particular for ULIRGs and partly for HLIRGs, the picture emerged that they depict the merger of two gas-rich galaxies (e.g., Genzel & Cesarsky 2000; Farrah et al. 2002), thereby producing an elliptical galaxy (e.g., Kormendy & Sanders 1992; Genzel et al. 2001). A strong encounter instead of a merger between two gas-rich galaxies may be what is observed, however (see Kroupa 2015 for a discussion on mergers vs. interactions), and in this case, the ULIRGs/HLIRGs may not be progenitors of elliptical galaxies. Whether a merger or not, the interaction triggers an intense star formation with SFRs between roughly 200 and 4000 $M_{\odot}\mathrm{yr}^{-1}$ (e.g., Farrah et al. 2002; Le Floc'h et al. 2005; Takata et al. 2006; Bastian 2008; Ruiz et al. 2013; Kilerci Eser et al. 2014), which matches the range of found SFRs well. These galaxies cover a wide redshift range of up to $z \approx 3$ (i.e., light emission up to 11.5 Gyr ago) and show a tendency of higher SFRs with higher redshifts (e.g., cf. Bastian 2008; Kilerci Eser et al. 2014 vs. Farrah et al. 2002; Takata et al. 2006, see also Rowan-Robinson 2000), which is confirmed by studies focusing on the evolution of the SFR with redshift or over cosmic time (e.g., Le Floc'h et al. 2005; Schiminovich et al. 2005; Speagle et al. 2014; Mancuso et al. 2016).

Toward higher redshifts, the level of obscuration of galaxies increases: they are usually barely visible in the optical and UV, but have an enormous emission at far-IR and sub-mm wavelengths (e.g., Michałowski et al. 2010; Narayanan et al. 2015; Mancuso et al. 2016). This is why they are called sub-millimeter galaxies (SMGs) or, more generally, dusty, star-forming galaxies (DSFGs). According to

their IR-luminosities, the most luminous of them fall into the regime of HLIRGs and are among the most luminous, heavily star-forming galaxies in the Universe (e.g., Michałowski et al. 2010; Hainline et al. 2011; Casey et al. 2014). Their SFRs are similar to those of ULIRGs/HLIRGs and typically lie between a few hundred and a few thousand $M_{\odot}\mathrm{yr}^{-1}$ (e.g., Alaghband-Zadeh et al. 2012; Swinbank et al. 2014; da Cunha et al. 2015; Simpson et al. 2015), with the tendency that SMGs with higher redshifts have higher SFRs (da Cunha et al. 2015). It has been argued that these DSFGs are not major mergers but galaxies experiencing their highest star formation activities (e.g., Farrah et al. 2002; Narayanan et al. 2015; Mancuso et al. 2016). This matches with the fact that massive elliptical galaxies are known to be α-element enhanced and metal-rich, such that they cannot have formed from the mergers of pre-existing comparatively metal-poor disk galaxies.

Moreover, these galaxies are extremely massive: they can be interpreted to reside in particle dark matter or in phantom dark matter halos (e.g., Famaey & McGaugh 2012; Lüghausen et al. 2015) with masses of between more than 10^{11} and more than 10^{13} $M_{\odot}$ (Hickox et al. 2012; Béthermin et al. 2013) and have stellar masses in the range of between lower than 10^{11} and more than 10^{12} $M_{\odot}$ (e.g., Swinbank et al. 2006; Michałowski et al. 2010; Hainline et al. 2011). For halo masses around $10^{12}M_{\odot}$, star formation occurs most efficiently (e.g., Behroozi et al. 2013; Béthermin et al. 2013; Wang et al. 2013), which is why the progenitors of even more massive present-day halos passed through this mass quickly, and thus formed most of their stars on timescales shorter than 1−2 Gyr (see left panel of their Fig. 13 in Behroozi et al. 2013; Marsan et al. 2015).

Overall, DSFGs represent a phase in massive galaxy evolution that marks the transition from cold gas-rich, heavily star-forming galaxies to passively evolving systems (Hickox et al. 2012). In simulations by Narayanan et al. (2015), this active phase was accompanied by a significant build-up of stellar mass; thereafter, these galaxies are expected to evolve into massive ellipticals (e.g., Michałowski et al. 2010; Hickox et al. 2012). For instance, when passively evolving high-redshift SMGs to the present time, Hainline et al. (2011) found their luminosity (and therefore mass) distribution to be similar to that of massive ellipticals in the Coma galaxy cluster. The authors noted that typical SMGs cannot represent the formation phase of the very luminous cD galaxies observed in galaxy clusters because the baryonic mass of a typical SMG is too low. Miller et al. (2015) emphasized that there are better tracers for the assembly of the most massive structures in the Universe than SMGs, Lyman-break galaxy analogs, for instance.

However, it needs to be taken into account that the Coma galaxy cluster is much richer in galaxies and in mass than the Fornax galaxy cluster. The cen-

ter of the Coma galaxy cluster is dominated by two giant ellipticals, NGC 4874 and NGC 4889. Measurements by Okabe et al. (2010, with $h = 0.678$ from Planck Collaboration et al. 2014) and Andrade-Santos et al. (2013) resulted in halo masses of $6.7 \cdot 10^{12}\ M_\odot$ and $7.6 \cdot 10^{12}\ M_\odot$ for NGC 4874, and $11.4 \cdot 10^{12}\ M_\odot$ and $9.1 \cdot 10^{12}\ M_\odot$ for NGC 4889, respectively. In comparison, Richtler et al. (2008, their Table 1) estimated a halo mass of $3.5 \cdot 10^{12}\ M_\odot$ for NGC 1399 within a radius of 80 kpc. Clearly, NGC 1399 is several times less massive than the center of the Coma galaxy cluster and could be considered as a less massive version of it at most. Nevertheless, there are hints that NGC 1399 went through multiple interactions that left an imprint on the spatial distribution of GCs (D'Abrusco et al. 2016) and a faint stellar bridge in the intracluster region on the west side of NGC 1399 (Iodice et al. 2016).

Regarding the formation timescale, massive elliptical galaxies like NGC 1399 must have formed on a short timescale, while less-massive galaxies are known to have formed over longer times, which is known as downsizing (e.g., Cowie et al. 1996; Thomas et al. 1999; Juneau et al. 2005; Recchi et al. 2009). Assuming that most of the mass of NGC 1399 was formed early on, the build-up must have been completed within less than 0.5 Gyr according to Eq. (19) in Recchi et al. (2009, see also their Fig. 18). This allows to estimate the SFR during the formation: to simplify matters, a constant SFR over that time can be assumed, which leads to $\mathrm{SFR} = M/t \approx 5 \cdot 10^{11}\ M_\odot/0.5\ \mathrm{Gyr} \approx 1000\ M_\odot/\mathrm{yr}$. Since the formation timescale might be shorter and the SFR over the formation period does not have to be constant, the peak SFRs might be a few times higher than estimated in this simple calculation.

In summary, the range of SFRs found in Chap. 3.4 is in very good agreement with the SFRs observed in SMGs and the simple estimate based on downsizing. Moreover, the age of the GCs/UCDs (Chap. 3.1) sets a limit on the formation timescale of NGC 1399 since the central Fornax galaxy and its GC/UCD system formed probably coevally. Most of the mass was built up within a few Gyr, which matches the generally short formation timescales of massive elliptical galaxies. In that respect, it seems reasonable to assume that as a result of their extreme star formation activity, massive high-redshift SMGs might represent the progenitors of cD galaxies like NGC 1399.

Chapter 4

Distribution of star formation rates during the rapid assembly of NGC 1399 as deduced from its red and blue globular clusters

After having analyzed which distribution of SFRs are responsible for the formation of the whole GC/UCD system around NGC 1399, the aim of this chapter is to repeat the analysis by determining the required SFRs for the red, metal-rich, and the blue, metal-poor, GCs/UCDs separately. The division into two color samples is based on new spectroscopic and photometric observations which are introduced in Chap. 4.1. Using the new surveys, I describe how to obtain a spectroscopic (Chap. 4.2) and a photometric sample (Chap. 4.3) and explain on which grounds the color of each object is determined. The photometric properties of each GCs/UCDs allows me to calculated the mass of each object individually (Chap. 4.4). I combine the masses of the red and blue objects from the two samples and generate an overall mass function for red and blue objects in Chap. 4.5. Then, the red and blue GC/UCD mass functions are corrected for mass loss in Chap. 4.6 and afterward decomposed into individual SC populations in Chap. 4.7. The resulting SFR distributions are presented and compared to the previous analysis in Chap. 4.8 and finally discussed in Chap. 4.9.

This chapter is based on a paper that will been published as Schulz, C., et al. with the title “Distribution of star formation rates during the rapid assembly of NGC 1399 as deduced from red and blue globular clusters”.

4.1 New spectroscopic and photometric surveys

4.1.1 VIMOS spectroscopy

The new spectroscopic data is taken from observations with the instrument VIMOS (Le Fèvre et al. 2003) on the VLT under the program ID 094.B-0687(B) (PI: M. Capaccioli). VIMOS is a wide field imager and multi-object spectrograph (MOS) in the visible wavelength range. Here, it was used in MOS mode and acquired a few thousands of spectra of point-like sources around NGC 1399. The radial velocities of these objects have been determined from the Calcium triplet. If this radial velocity is within the limits of 900 to 2100 km/s it is assumed that it belongs to the Fornax galaxy cluster. All further details about the observations and the data reduction can soon be found in Pota et al. (in prep.).

The outcome is a catalog which includes 866 objects with radial velocities based on the Calcium triplet in its final version, out of which 471 are classified as foreground stars and 395 as GCs of the Fornax galaxy cluster. Some of the objects were observed multiple times. For the final catalog, multiple matches have been removed to make sure that every object occurs only once resulting in 464 stars and 388 GCs out of 852 unique objects in total.

4.1.2 Fornax Deep Survey (FDS)

The photometric data is taken from the Fornax Deep Survey (FDS, D'Abrusco et al. 2016; Iodice et al. 2016) and consists of images in the u, g, r, and i bands. They have been obtained during Guaranteed Time Observations on the 2.6 m ESO VLT Survey Telescope (VST) with the wide field camera OmegaCAM that is equipped with broadband Sloan filters (Kuijken 2011). The program is still ongoing but the observations of the central region as well as the first analyses of them have been completed (D'Abrusco et al. 2016; Iodice et al. 2016, 2017).

For the GC selection, the "small stellar systems" catalogs compiled by M. Cantiello (priv. comm.) are used. They include SExtractor photometry of all compact sources like GCs, stars and unresolved background galaxies in the observed fields 6, 7, 11, 12, 16, 17, and 20 for each band separately. All objects from these fields are marked with dots in two different shades of gray in Fig. 4.1 to visualize the relative position of the fields to each other. The field numbers are indicated. Note that the fields are overlapping at their edges as indicated by the horizontal and vertical boxes in Fig. 4.1 implying that objects in the overlapping regions are observed in more than one field. I merged the separate catalogs

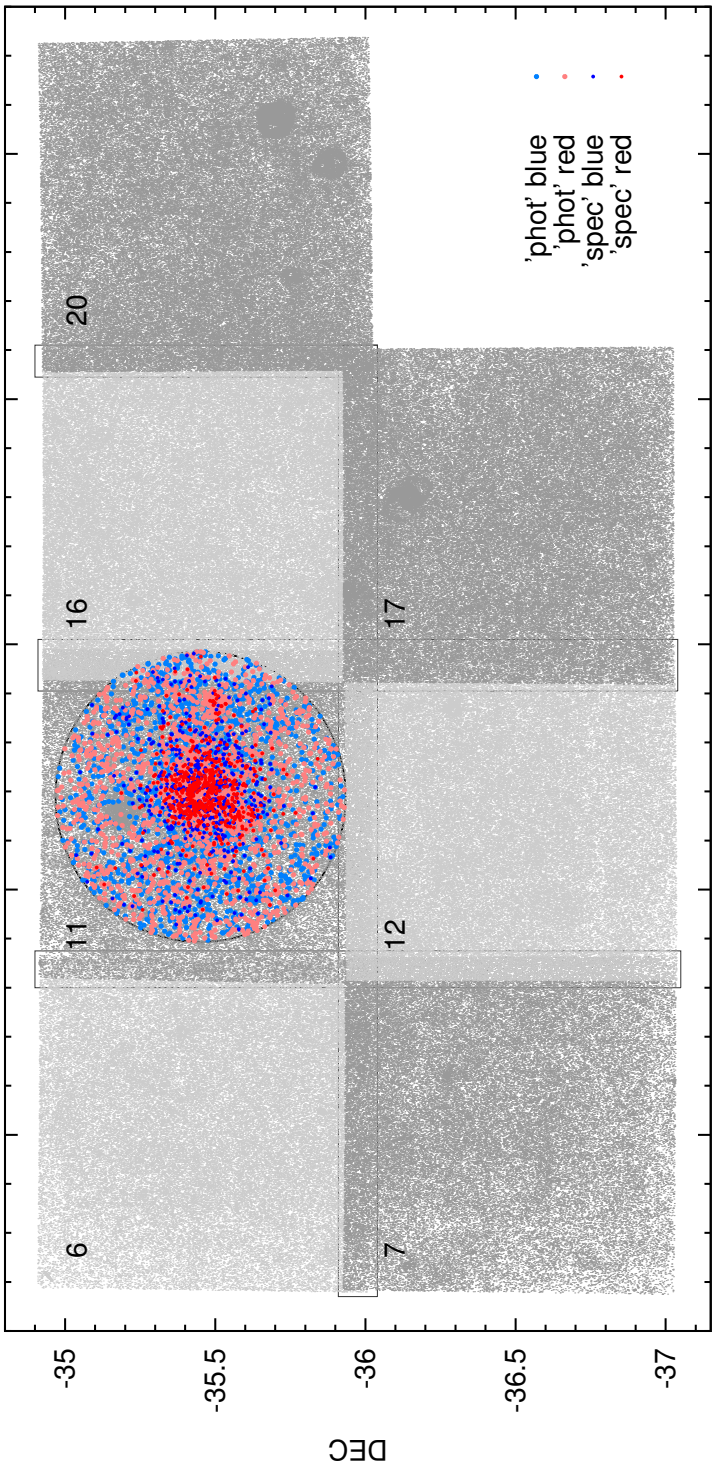

Figure 4.1: Spatial distribution of photometric objects in the Fornax galaxy cluster. The gray dots are compact sources observed in the FDS (Chap. 4.1.2) and amount to over 660 000 objects. Two different shades of gray are used to depict the relative positions of the different fields to each other. The field numbers are indicated. Horizontal and vertical boxes illustrate the overlap regions between the fields. Objects from the spectroscopic sample (Chap. 4.2) are marked with saturated red and blue colors and smaller filled points in comparison to the objects from the photometric sample (Chap. 4.3). The circle is centered on NGC 1399 and indicates a radius of 160 kpc.

to obtain a "master" catalog in which multiple detections of the same object are averaged and assigned to each object all available magnitudes. Both tasks were carried out based on the coordinates of each object. After some testing, it turned out that a matching radius of 1.8 arcsec is ideal in terms of being large enough to account for slight shifts between the different bands but also small enough to avoid assigning the same measured magnitude to more than one object. However, before being able to use the measured magnitudes, an aperture correction and a color calibration have to be applied as explained in the next two paragraphs, following the instructions in an internal document by M. Cantiello (priv. comm.).

Aperture correction
For point-like sources, the photometry is generally determined from the aperture magnitude at 8 pixels ($\approx 1\farcs7$) in diameter by applying the aperture correction to infinite radius. The corrected magnitude $m_{\rm corr}$ is calculated from

$$m_{\rm corr} = MAG\_APER_{\rm 8pix} - c_{\rm 8pix}, \tag{4.1}$$

where $MAG\_APER_{\rm 8pix}$ is the measured SExtractor magnitude for an object in a particular band and $c_{\rm 8pix}$ is the constant aperture correction, both for an 8 pixel aperture. $c_{\rm 8pix}$ is derived from isolated point sources and depends on the field and on the band and is tabulated in the above mentioned internal document.

Color calibration
All magnitudes have to be color corrected for which the equations as given in the VST-Tube data reduction pipeline were used. They read for objects in the fields 6, 7, and 12:

$$m_{\rm u,corr} = m_{\rm u,unc} + 0.0318(u - g), \tag{4.2}$$
$$m_{\rm g,corr} = m_{\rm g,unc} + 0.406 + 0.0380(g - i), \tag{4.3}$$
$$m_{\rm r,corr} = m_{\rm r,unc} + 0.082 + 0.0460(r - i), \tag{4.4}$$
$$m_{\rm i,corr} = m_{\rm i,unc} - 0.0030(g - i), \tag{4.5}$$

and for objects in the fields 11, 16, 17, and 20:

$$m_{\rm u,corr} = m_{\rm u,unc} + 0.0459(u - g), \tag{4.6}$$
$$m_{\rm g,corr} = m_{\rm g,unc} + 0.0247(g - i), \tag{4.7}$$
$$m_{\rm r,corr} = m_{\rm r,unc} + 0.0831(r - i), \tag{4.8}$$
$$m_{\rm i,corr} = m_{\rm i,unc} + 0.0005(g - i). \tag{4.9}$$

A few points have to be mentioned here: the magnitudes used to calculate the color term have to be the color corrected magnitudes, e.g. $g = m_{\mathrm{g,corr}}$. Thus, the above equations have to be rearranged such that the knowns (i.e. the measured, uncorrected magnitudes, m_{unc}) and the unknowns (i.e. the color calibrated magnitudes, m_{corr}) appear on separate sides, starting with Eqs. (4.3) and (4.5), and Eqs. (4.7) and (4.9), respectively, because these equations depend only on g and i. Thus, a color calibration can only be applied if g and i magnitudes are available simultaneously. Only in this case, the calibration of the r and u magnitudes can be achieved, assuming they are available. Also, note the zero-point corrections for the g and r bands and the negative dependence on $(g - i)$ in the i band in the fields 6, 7, and 12.

The matching of the different fields and the different bands yielded a catalog with 661 732 objects from all fields where each object occurs only once and has corrected u, g, r, and i magnitudes, if they were available and if a color correction was possible.

4.2 Compilation of the spectroscopic GC/UCD sample

4.2.1 Matching of all available data

The previously used spectroscopic GC/UCD sample in Chap. 3.1 is a compilation of many different studies (Hilker et al. 1999b; Drinkwater et al. 2000; Mieske et al. 2002, 2004; Bergond et al. 2007; Mieske et al. 2008; Hilker et al. 2007; Firth et al. 2007; Gregg et al. 2009; Schuberth et al. 2010; Chilingarian et al. 2011, and Puzia & Hilker, priv. comm.) and contains radial velocities of 947 of the brightest GCs/UCDs around NGC 1399. They have similar ages and thus comparable M/L-ratios, for which reason the brightest objects are also among the most massive in the central Fornax galaxy cluster. The spectroscopic sample therefore offers very robust number counts at the high-mass end of the GC/UCD mass function.

To increase the number of spectroscopically confirmed objects, the previous spectroscopic catalog was matched with the new spectroscopic VIMOS survey (Chap. 4.1.1). I obtained 1 238 objects in total from which 848 and 291 originated from the previous catalog and from the new survey, respectively, while 99 objects were contained in both. Note that among the matches, two objects from the previous catalog have been misclassified as GCs and turned out to be stars according to the new survey. After excluding them, 1 236 GCs/UCDs with measured radial velocities remained, giving the new spectroscopic sample.

The next step was to match these objects with the FDS survey (Chap. 4.1.2) based on coordinates to assign all GCs/UCDs photometric magnitudes in the g, r, i, and u bands. The vast majority of the objects, 1 219 in total, are simultaneously detected in the bands g, r, and i while 627 of them are additionally detected in u. The analysis is concentrated on the former three bands because of the almost full coverage there. However, if the magnitude in u-band for an object is available it is used as an additional selection criterion (see Chap. 4.2.2).

The advantage of this approach is that the two samples, the spectroscopic (this section) and the photometric (Chap. 4.3), are photometrically homogeneous which allows a consistent mass determination (Chap. 4.4) among them.

4.2.2 Selection of the final GC/UCD sample

The next main step is to identify possible outliers among the spectroscopically confirmed objects, examine them and decide whether or not to exclude these objects from the spectroscopic sample. For this exercise several diagnostic plots were used:

3D plot $g-r$ vs. $g-i$ vs. $r-i$
Since almost all objects have measured magnitudes in the g, r, and i bands, I consider all possible color combinations, namely $g-r$, $g-i$, and $r-i$, and plot them three-dimensionally (Fig. 4.2). It turned out that all data points lie within a tilted plane.

3D plot $u-g$ vs. $u-r$ vs. $u-i$
For those objects which also have a measured u magnitude, I plot all possible color combinations between u and all other bands, namely $u-g$, $u-r$, and $u-i$, three-dimensionally as well (Fig. 4.3). The distribution of data points has a tight, cigar-like shape.

Parameters FWHM and "class"
Moreover, it was checked how the objects are distributed in terms of their full-width-at-half-maximum (FWHM) and their stellarity index ("class") in the different bands as determined from the SExtractor photometry of the FDS data (see Chap. 4.1.2). GCs have typically rather low FWHM values and a high class value, meaning that they appear point-like in images. However, note that this does not

necessary apply to the most massive UCDs which might be slightly extended and exhibit a faint envelope (e.g., Wittmann et al. 2016).

In both 3D plots as well as in the plots showing the FWHM and the parameter "class", objects that lie at the edge or outside the main body of data points are categorized as possible outliers. For all these objects, it was first examined where they are lying in the other plots. It turned out that most of these objects – selected independently in the different plots – are the same. Objects for which this was the case were excluded from the sample. Then, I examined the remaining objects that were classified as possible outliers visually in images taken by the FDS (Chap. 4.1.2). Objects that show one or more of the following features are excluded from the sample as well:

- object on top of diffuse background
- object very faint and/or diffuse
- object has irregular outer shape
- object is extended

All objects that have been excluded from the initial sample are marked in green in Fig. 4.2 and Fig. 4.3.

As mentioned above, the data points in the 3D plot $g - r$ vs. $g - i$ vs. $r - i$ (Fig. 4.2) lie within a tilted plane. The data points (or equivalently, the three dimensional coordinate system) were rotated such that the plane lies in two dimensions. Thereafter, the x- and y-axis can be described by $g + 0.366r - 1.366i$ and $g - 1.366r + 0.366i$ and the corresponding distribution of the data points is shown in Fig. 4.4. The latter plot indicates a bit clearer than Fig. 4.2 that the distribution of data points could be described by two overlaying Gaussians, one maximum at higher and another maximum at lower y-values. This hypotheses was tested by applying a Gaussian Mixture Model (GMM) with two components from the scikit-learn package for python (Pedregosa et al. 2011) to the data.

It turned out that, indeed, the distribution of data points can be well described by two Gaussians (Fig. 4.4). Together, they form an elongated body with one narrower Gaussian at higher and a broader Gaussian at lower y-values. According to the colors in the color-color space, the narrower Gaussian at the top describes the distribution of red GCs/UCDs while the broader Gaussian at the bottom contains the blue GCs/UCDs. One useful method in the GMM package is

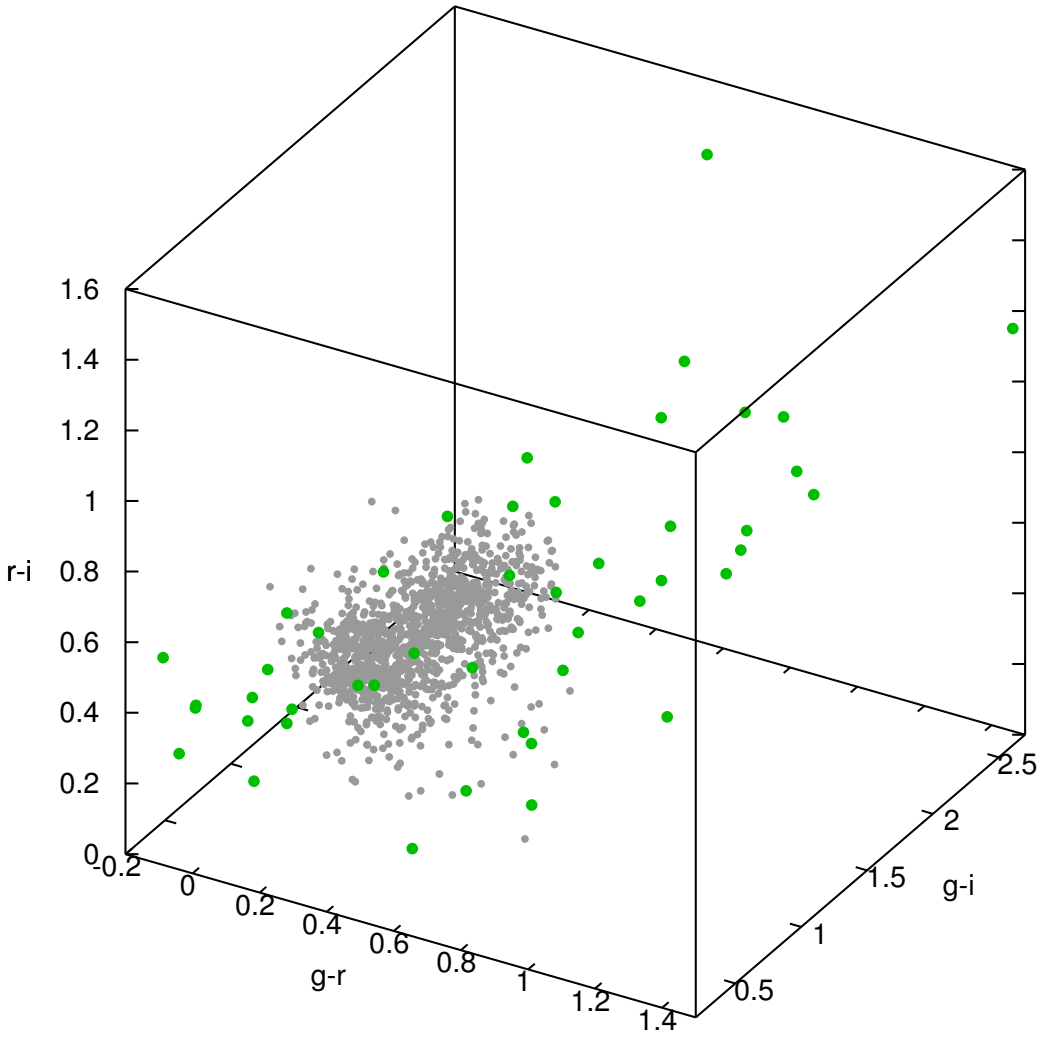

Figure 4.2: 3D plot $g-r$ vs. $g-i$ vs. $r-i$ for the spectroscopic GC/UCD sample (Chap. 4.2). The excluded objects are highlighted in green while all gray object are kept for the analysis. Note that all data points lie within a plane. Rotating the plane such that it lies in two dimensions gives a distribution of data points as shown in Fig. 4.4.

`predict_proba(X)` which predicts for each data point the probability of belonging to each of the Gaussians. Fig. 4.4 shows the probability of being a red GC/UCD (right color bar) according to which the data points have been colorized.

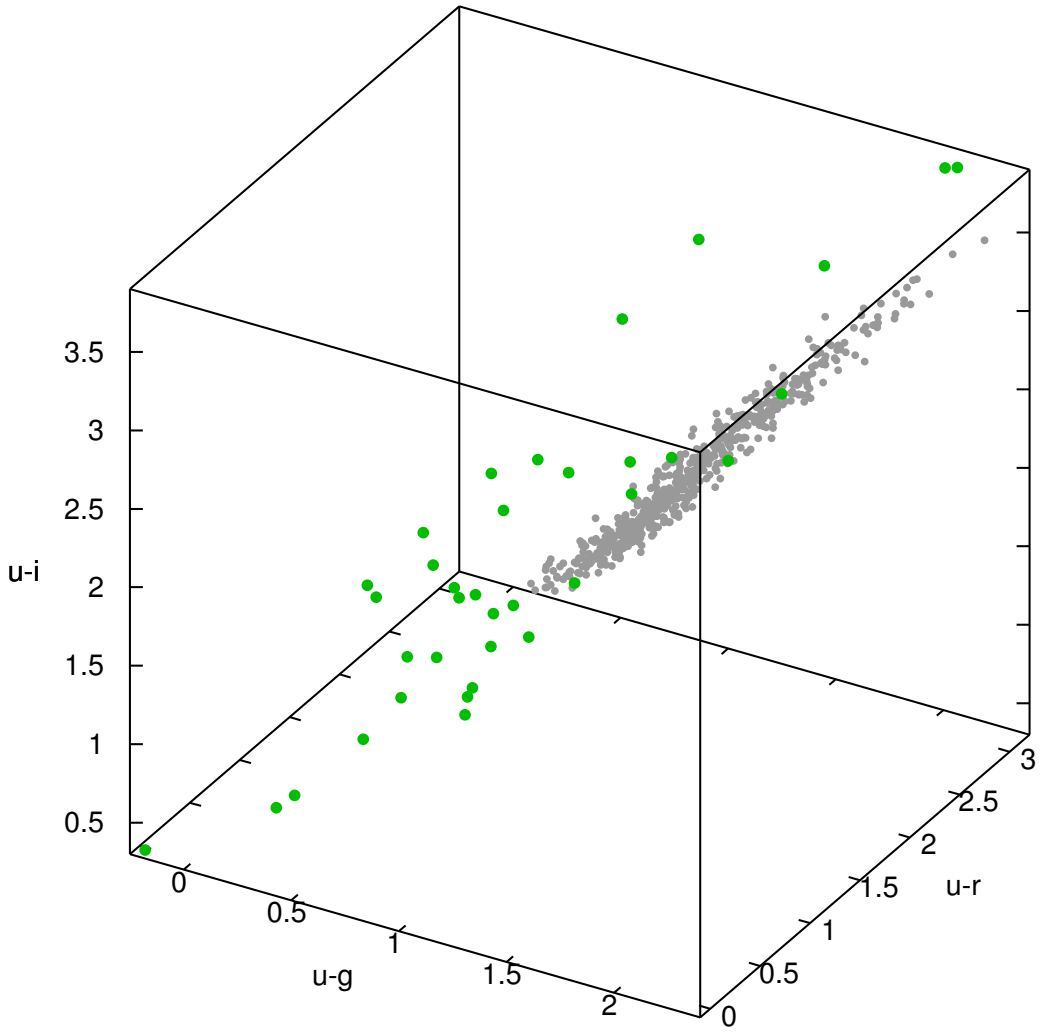

Figure 4.3: 3D plot $u-g$ vs. $u-r$ vs. $u-i$ for the spectroscopic GC/UCD sample (Chap. 4.2). The excluded objects are highlighted in green while all gray object are kept for the analysis. Note that the gray objects have a tight, cigar-like distribution.

Another available method is `score_samples(X)` which calculates for each point in the plot the weighted logarithmic probability, meaning the sum of the logarithmic probability to belong to one of the Gaussians and its logarithmic weight. This method is useful for the construction of the contours in Fig. 4.4 (left color bar, varying from green to yellow). As can be seen, in the transition region, the con-

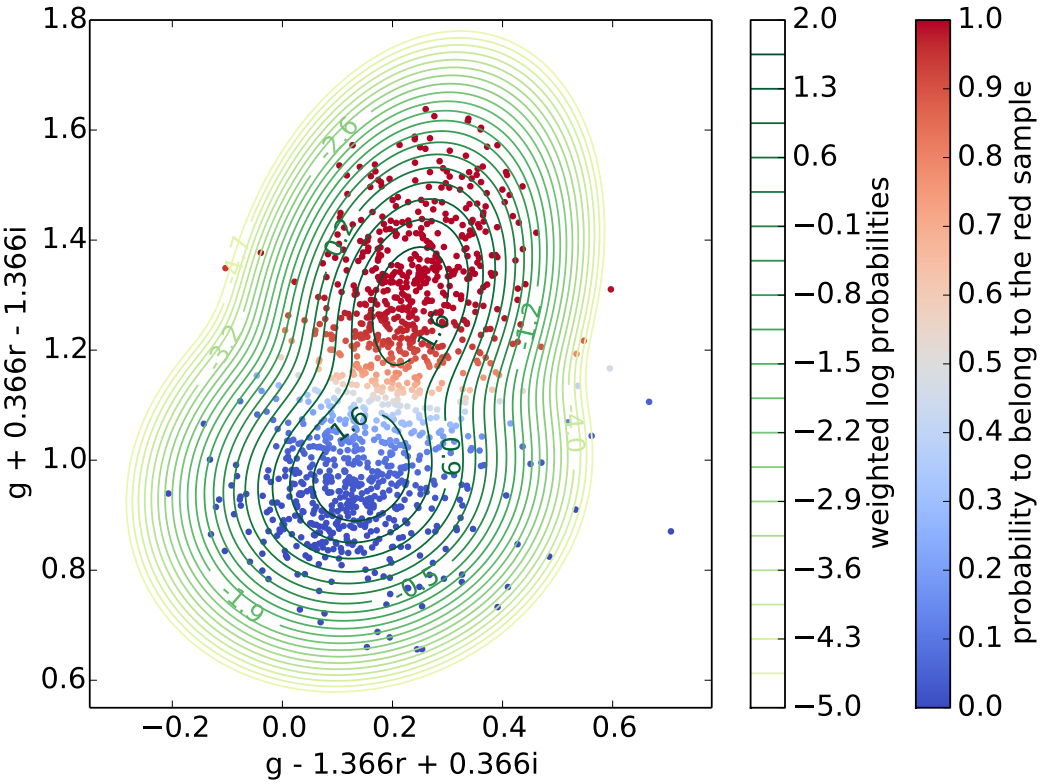

Figure 4.4: Distribution of GCs/UCDs in two dimensions after rotating the plane of data points from Fig. 4.2. The color of each data point depends on its probability of belonging to the red or blue sample as indicated by the right color bar and was calculated after applying a two component GMM to the data. The green to yellow contours indicate the shape of the two overlaying Gaussians. Note that blue GCs/UCDs are somewhat broader distributed as compared to the red ones.

tours become a bit tighter. Also, the contours trace nicely the somewhat narrower Gaussian of the red GCs/UCDs and the broader Gaussian of the blue GCs/UCDs and show that the same applies for the maxima of both Gaussians. I conclude from the shape of the contours that it is plausible to assume that the GCs/UCDs around NGC 1399 can be categorized into red and blue objects.

The last selection criterion for the spectroscopic GC/UCD sample is the spatial location in the center of the Fornax galaxy cluster. In Chap. 3.1, I included only GCs/UCDs which reside within 85 kpc around NGC 1399 since the observational coverage decreased quickly beyond that radius while here, a much larger area has

been covered by spectroscopy so that the same radius of 160 kpc is applied as for the photometric sample (see Chap. 4.3). This yielded 1 112 objects in total. These objects are marked with small red and blue filled points inside the circle with a radius of 160 kpc around NGC 1399 in Fig. 4.1. Note the extended distribution of GCs/UCDs from the spectroscopic sample, in particular blue ones, east and west of NGC 1399 while spectroscopically confirmed objects are almost absent north and south of NGC 1399. The color of each object has been determined based on the probability calculated with `predict_proba(X)`; for the sake of simplicity, the probability to separate red and blue objects is set to 0.5. All these objects have a measured magnitude in the *g*, *r*, and *i* bands and approximately half of them also in the *u* band. Based on the former three bands, the masses of all GCs/UCDs are determined as described in Chap. 4.4. For the mass determination, the above calculated probability regarding the membership to the red or blue GC/UCD sample for each object will also be used.

4.3 Compilation of the photometric GC/UCD sample

The photometric sample is intended to be the counterpart of the spectroscopic sample: While the latter comprises the most massive objects around NGC 1399 but has smaller number counts because of limited depth due to spectroscopy, the former still captures fainter objects. Since the mass-to-light ratio among the GCs is similar, fainter objects are generally less massive which is why the photometric sample offers robust number counts towards lower masses.

The photometric sample is compiled from the photometric catalog based on the FDS survey (Chap. 4.1.2) according to the following criteria:

Spatial location
Like in Chap. 3.1, only sources are selected from the FDS catalog within 160 kpc around NGC 1399.

Brightness
Only objects with $g > 20.5$ and $i > 19$ are considered since very bright objects are unlikely to be a GC anyway. In the photometric sample, it is not aimed for including the massive and bright GCs/UCDs since they are already covered by the spectroscopic sample.

Color
Here, two constraints were set based on the two 3D plots (Chap. 4.2.2):

- $g - r$ vs. $g - i$ vs. $r - i$: the object has to have a weighted logarithmic probability of more than -5 (computed from `score_samples(X)`). This means it has to lie inside the outermost contour in Fig. 4.4.

- $u - g$ vs. $u - r$ vs. $u - i$: if a magnitude in the u band is available, the object has to be located within the volume spanned by the data points from the spectroscopic sample.

FWHM and "class"
In the bands g, r, and i (and in u, if available), the object has to have a FWHM of less than 15 pixel (corresponding to about 3.2 arcsec) and the SExtractor stellarity index "class" has to be larger than 0.3.

Cross-check with the spectroscopic catalog
The object must not be classified as a star in the spectroscopic catalog (Chap. 4.1.1).

In total, 4 684 objects from the photometric catalog are matching the above constraints. Based on the GMM of the spectroscopic sample, I calculate for each object with `predict_proba(X)` how probable it is that this objects belongs to the red and blue sample, respectively. Setting the cut at $p = 0.5$, I obtain 2 369 red and 2 315 blue objects in the photometric sample. Their spatial distribution is shown in Fig. 4.1: The objects are marked with light-red and light-blue filled points inside the circle around NGC 1399, corresponding to a radius of 160 kpc. Based on their magnitudes in g, r, and i, their masses are determined in Chap. 4.4 in the same way as for the objects from the spectroscopic sample.

Additionally, I tested how these objects are distributed in the rotated color space ($g+0.366r-1.366i$ vs. $g-1.366r+0.366i$) in comparison to those ones from the spectroscopic sample by applying a two component GMM to these objects. The result can be viewed in Fig. 4.5: as in Fig. 4.4, all objects are colorized according to their probability of being red or blue while their two-dimensional distribution is traced by the black-gray contours. It is striking how similar the objects in the photometric and the spectroscopic sample are distributed: In both cases, red and blue GCs/UCDs build a main body of elongated shape on top of which a red and a blue maximum is located. As shown by the contours, the peaks of the red GCs/UCDs of the spectroscopic and the photometric sample are very

close to each other but do not agree as remarkably well as the peaks of the blue GCs/UCDs which lie almost exactly at the same place. This finding strengthens the argumentation that GCs/UCDs exist in two types: either as rather red or as rather blue objects. Also, it shows that the contamination by foreground stars and background galaxies is very low. Additionally, I included in Fig. 4.5 those objects in gray which match the above mentioned criteria except for the fact that they lie outside the outermost contour in Fig. 4.4.

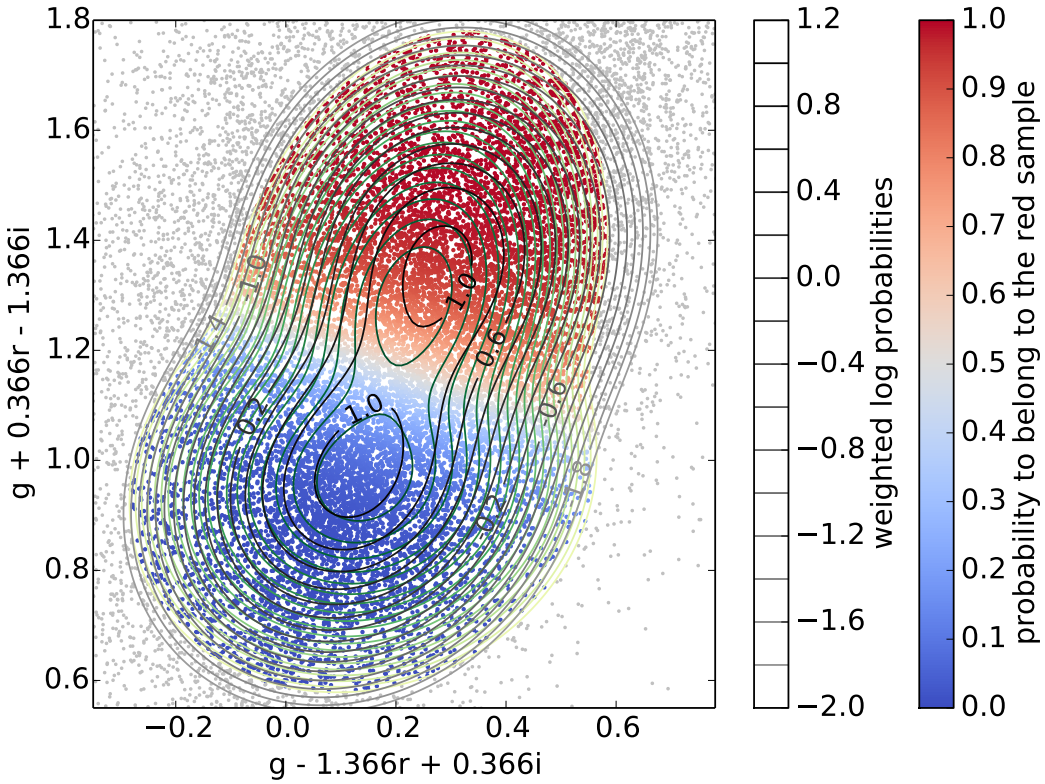

Figure 4.5: Same as Fig. 4.4 but for objects selected from the photometric catalog (Chap. 4.1.2) according the criteria listed in Chap. 4.3. These objects are marked in the color range from blue to red depending on their probability to belong to the blue or red sample. Their two component GMM is overplotted with gray contours; the green-yellow contours belong to the GMM of the spectroscopic GC/UCD sample and are taken from Fig. 4.4. Note that the contours match well, particularly for blue GCs/UCDs. For reference, all objects which match the criteria but lie outside the outermost contour in Fig. 4.4 are marked in gray.

4.4 Mass determination

As in Chap. 3, the masses of the objects from the spectroscopic and photometric sample are determined based on evolutionary population synthesis models by Maraston (2005). Assuming a Kroupa IMF (Kroupa 2001) and a 13 Gyr old simple stellar population (Misgeld & Hilker 2011; Mieske et al. 2013; Puzia et al. 2014) for the GCs/UCDs, their mass-to-light ratio, M/L_V, reads depending on whether they are red or blue:

$$\text{red:}\quad \frac{M}{L_V} = 4.383 + 1.763 \arctan\left(8.087\left((g-i)-1.178\right)\right), \tag{4.10}$$

$$\text{blue:}\quad \frac{M}{L_V} = 4.430 + 1.721 \arctan\left(8.227\left((g-i)-1.182\right)\right), \tag{4.11}$$

where the magnitudes have to be in the AB system (Oke & Gunn 1983). As mentioned in Chap. 4.1.2, OmegaCAM is equipped with broadband Sloan filters in the bands u, g, r, and i so that the measured magnitudes comply with the SDSS system. This is very convenient because the SDSS photometry is based on the AB system[1] which means that no conversion is necessary.

To determine the masses, the luminosity in the V band is used, L_V, which is obtained after applying the Lupton relations[2]:

$$V = g - 0.5784(g-r) - 0.0038, \tag{4.12}$$

based on which the absolute magnitude in the V band, M_V, is calculated using the distance modulus from NGC 1399, $(m-M)_{V,\,\mathrm{NGC1399}} = 31.39$ mag:

$$M_V = V - (m-M)_{V,\,\mathrm{NGC1399}}. \tag{4.13}$$

With M_V, I compute L_V:

$$L_V = 10^{-0.4(M_V-4.83)}, \tag{4.14}$$

and finally the mass of the object, M:

$$M = \frac{M}{L_V} \times L_V. \tag{4.15}$$

[1] https://www.sdss3.org/dr8/algorithms/fluxcal.php#SDSStoAB
[2] http://www.sdss3.org/dr8/algorithms/sdssUBVRITransform.php#Lupton2005

For the spectroscopic sample, the distinction between red and blue objects is carried out with a Monte Carlo simulation based on the probabilities determined in Chap. 4.2.2 to see how strongly the probabilities of the individual objects influence the final mass functions. Before starting with the mass determination, a random number r is generated for each object and compared with the probability p. For $r > p$, the object is added to the red sample and its M/L_V ratio is calculated with Eq. (4.10); for $r < p$, Eq. (4.11) is used and the object is assigned to the blue sample. This procedure is repeated 10 000 times for the whole spectroscopic sample. From this, 10 000 samples are obtained with the masses of red and blue objects. The masses of each sample are then ordered in decreasing manner. For the red and blue samples separately, I determine from all samples the maximum, median, and minimum for the most massive, second-most massive, third-most massive and so on object. The median mass function of the red and blue spectroscopic sample is plotted cumulatively with a yellow and cyan continuous line in the upper left and middle panel, respectively, of Fig. 4.6. The slightly lighter colored regions around the median mass functions show up to which masses the mass function reached at maximum/minimum in the 10 000 runs. As can be seen, toward lower masses the minimum and maximum mass functions quickly converge into the median mass function.

For the photometric sample, the procedure is essentially the same except for the fact that I did not run a Monte Carlo simulation to distinguish between red and blue objects but simply decided based on the probability p: for $p > 0.5$, the object is considered to be red while for $p < 0.5$, I assumed the object to be blue and calculated the masses accordingly. The mass function of the red and blue photometric sample is plotted cumulatively with a brown and dark-blue continuous line in the upper left and middle panel, respectively, of Fig. 4.6. The reason I relinquished from a Monte Carlo simulation here is that I am only interested in the medium- to low-mass part of the mass function where the difference between maximum, median, and minimum is expected to be small since the largest deviations are only observed at the high-mass end as became apparent in the case of the spectroscopic sample.

As in Chap. 3.1, an age of 13 Gyr was assumed for the GCs/UCDs (Misgeld & Hilker 2011; Mieske et al. 2013; Puzia et al. 2014). However, their age could be smaller, 11 Gyr for instance, or even less. Also, instead of using the evolutionary models by Maraston (2005), those ones by Bruzual & Charlot (2003) could be used. For all combinations of the different cases, I calculated the median present-day mass functions for the red and blue spectroscopic sample and show them in Fig. 4.7. The labels are as follows: “M” and “BC” denotes the considered

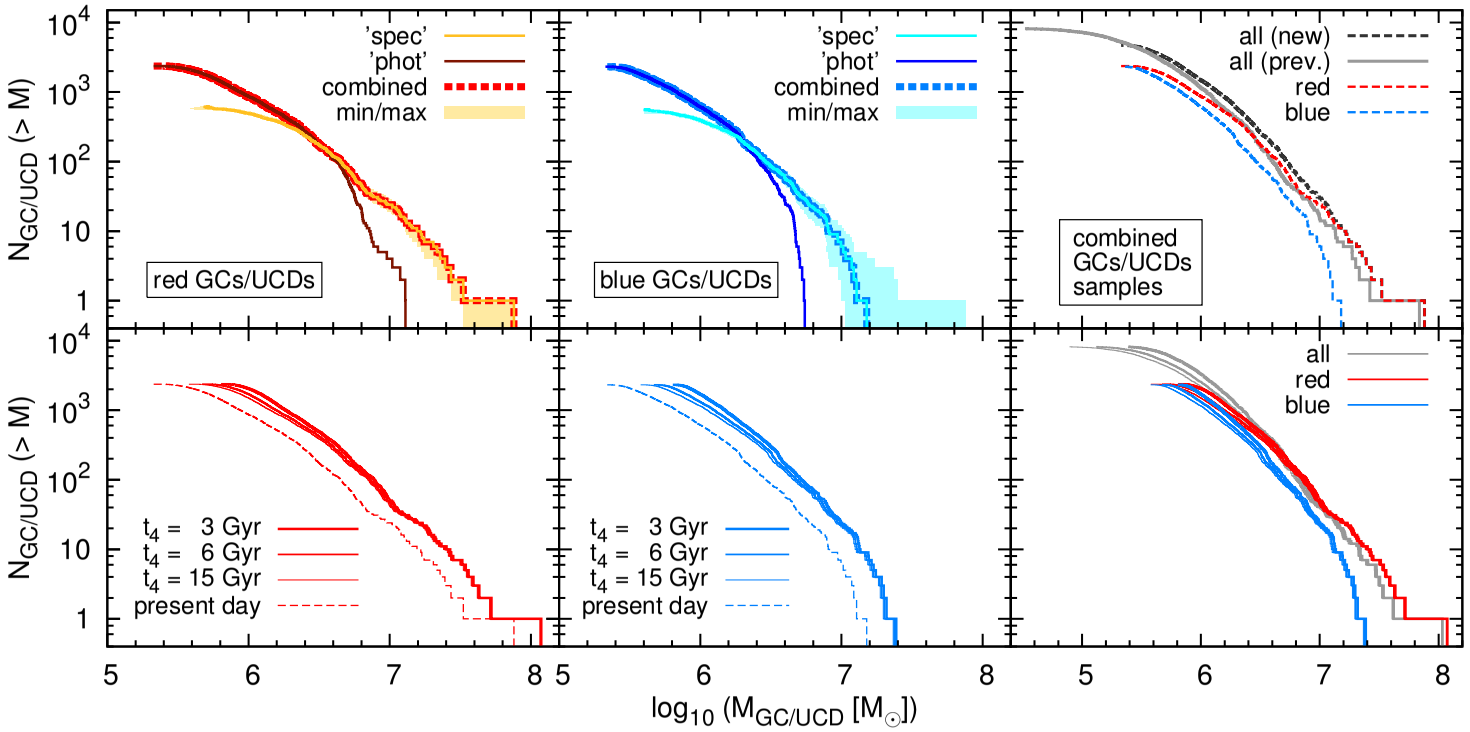

Figure 4.6: The cumulative mass functions of the red (left panels) and blue (middle panels) GC/UCD sample: in the upper panels, the observed mass functions of the spectroscopic ('spec' sample, yellow and cyan continuous lines) and the photometric sample ('phot' sample, brown and dark-blue continuous line) for the red and blue sample are shown. Note that these two mass functions intersect in both cases. The combined, present-day cumulative mass functions of the red and blue GCs/UCDs are underlaid by thick red and blue dashed lines, respectively, in the corresponding panels and are defined by the mass function of the spectroscopic sample from the high-mass end until the intersection and by the mass function of the photometric sample from the intersection until the low-mass end. The black dashed line in the upper right panel shows the cumulative mass function of red and blue GCs/UCDs together. In the lower panels, the cumulative mass functions corrected for mass loss (Chap. 4.6) are shown for different parameters t_4 (red and blue continuous lines; thick: t_4 = 3 Gyr, medium-thick: t_4 = 6 Gyr, thin: t_4 = 15 Gyr). In the right panels, the red and blue cumulative mass functions are drawn together for comparison. For reference, the present-day and corrected overall mass functions irrespective of the underlying color distribution from Fig. 3.1 (red dotted line there) and Fig. 3.2 (blue, purple, and orange continuous lines there), respectively, are shown in gray.

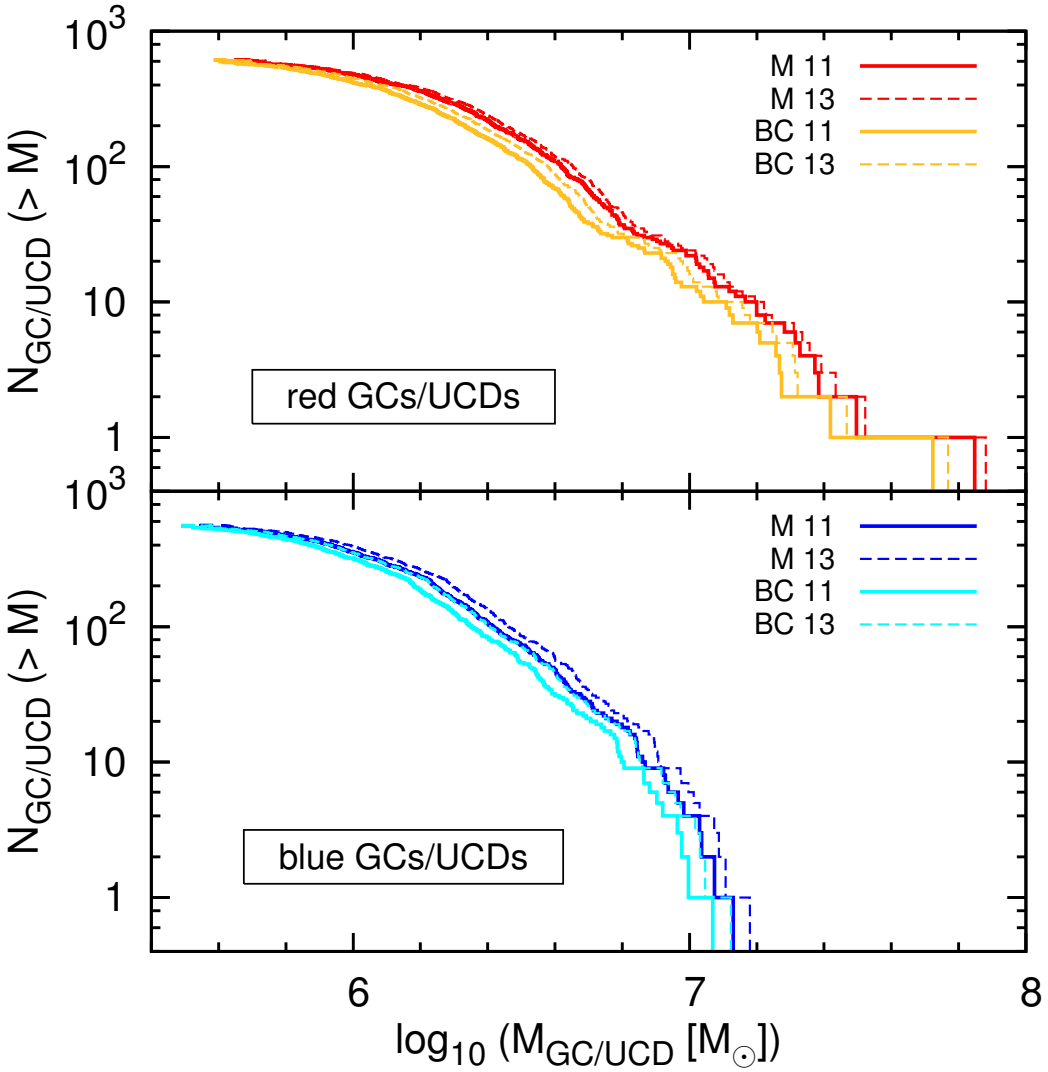

Figure 4.7: The cumulative present-day mass functions of red (top panel) and blue (bottom panel) GC/UCD based on the spectroscopic sample and on two different evolutionary models ("M": Maraston 2005; "BC": Bruzual & Charlot 2003) and assuming two different ages (11 and 13 Gyr).

model and "11" and "13" the assumed age of the GCs/UCDs. The assignment between the different models and the color of the lines can be taken from the legend. To guide the eye, mass functions where only the assumed age differs have the same color (13 Gyr: continuous lines; 11 Gyr: thin dashed lines). As can be

seen, younger ages cause generally the corresponding mass function to be slightly shifted toward lower masses. This is expected since an object with a younger age would have lost less mass and would therefore have a smaller initial mass as compared to an older object with the same present-day mass.

As can be seen, the general shape of the present-day mass functions is mostly preserved; the mass functions are mainly shifted toward higher or lower masses. The choice of the evolutionary models and the assumption of the age leads to a variation in mass of less than 0.2 dex or a factor of less than 2. Apparently, this influences the resulting mass functions much stronger than pure error propagation based on uncertainties in the measurement of the magnitudes. This needs to be taken into account when deriving the required SFR distributions from the mass functions and interpreting them (Chap. 3.5.2).

4.5 Combination of the photometric and spectroscopic sample

The aim is to construct for the red and blue GCs/UCDs around NGC 1399 an overall cumulative mass function based on the distribution of masses in their respective spectroscopic and photometric sample. As can be seen in Fig. 4.6, the latter two intersect each other; this applies to red and blue GCs/UCDs. Thus, I define the overall mass function such that it is described by the spectroscopic sample from the high-mass end until the intersection and by the photometric sample from the intersection until the low-mass end. This applies for red as well es blue GCs/UCDs. These overall cumulative mass functions are underlaid with a thick red and blue dashed line in the upper panels and are drawn by a thin red and blue dashed line in the lower panels of Fig. 4.6.

In comparison to the previous analysis of the GCs/UCDs around NGC 1399 in Chap. 3, three things become apparent. First, a scaling had been applied in Chap. 3.1: the photometric sample was shifted upward in order to match the number of objects in the spectroscopic sample at a certain mass. Apparently, this is not necessary here since the number of objects in the photometric sample outreach the number of objects in the spectroscopic sample. Interestingly, the mass at which the photometric and spectroscopic sample intersect (red: $\log_{10} M \approx 6.6$, blue: $\log_{10} M \approx 6.4$) is essentially the same as the scaling point in Chap. 3.1 which is $\log_{10} M = 6.6$. The reason is that the surroundings of NGC 1399 are now fully covered by spectroscopic and photometric observations (see Fig. 4.1). Second, in

the upper right panel of Fig. 4.6, the cumulative mass function for all GCs/UCDs irrespective of their color from Fig. 3.1 (red dotted line there) were included as a gray continuous line. Apparently, the mass function of red GCs/UCDs found here agrees almost perfectly with the latter over almost two orders of magnitude so that the mass functions of red and blue GCs/UCDs together (black dashed line) slightly outnumber the GC/UCD estimates from the previous analysis. Note that in particular toward the high-mass end this finding is robust since the objects there stem from the spectroscopic sample where all sources have been observed individually. That means, previously, the number of GCs/UCDs with masses of around and below 10^7 $M_\odot$ were slightly underestimated. Third, the overall mass function found previously (gray continuous line) has a lower low-mass limit as compared to the overall mass function found here (black dashed line). Since the mass of a GC/UCD is through its mass-to-light directly related to its brightness, this comparison shows clearly that the low-mass end is limited by the depth of the photometric observations. This is expected since deep HST photometry has been used before.

4.6 Correction of the mass functions of red and blue GCs/UCDs

After having obtained the present-day mass functions of red and blue GCs/UCDs, the two mass functions need to be corrected for mass loss during the lifetime of the GCs/UCDs. Following Chap. 3.2, the mass loss for each GC/UCD is calculated based on the model by Lamers et al. (2005a) which accounts for the mass loss due to stellar evolution and the disruption of SCs in tidal fields: Eq. (3.1) gives the initial mass of any SC, $M_{\rm initial}$, as a function of its present mass, $M_{\rm now}$, and its age, t, which is assumed to be $t = 13$ Gyr for the red and blue GCs/UCDs (Chap. 4.4). The function $\mu_{\rm ev}(t)$ carries the information about the mass loss due to stellar evolution (Eq. (3.2)). The parameters $a_{\rm ev}$, $b_{\rm ev}$, and $c_{\rm ev}$ in Eq. (3.2) depend on the metallicity, Z. The metallicity distribution of the metal-poor and the metal-rich GCs/UCDs peak at roughly -1.5 dex and -0.5 dex, respectively. This corresponds to a metallicity of $Z_{\rm red} \approx 0.005$ for the red and $Z_{\rm blue} \approx 0.0005$ for the blue GCs with $Z_\odot = 0.017$ (e.g., Grevesse & Sauval 1998). Using a newer estimate by Asplund et al. (2009, see also references therein), $Z_\odot = 0.0134$, I obtain metallicities of $Z_{\rm red} \approx 0.004$ and $Z_{\rm blue} \approx 0.0004$ for the red and blue GCs/UCDs, respectively.

Comparing to their Table 1 in Lamers et al. (2005a), the closest match is $Z = 0.0040$ for the red and $Z = 0.0004$ for the blue GCs/UCDs. The corresponding values of the parameters $a_{\rm ev}$, $b_{\rm ev}$, and $c_{\rm ev}$ for these two cases can be found in Table 4.1. Note that the differences in the individual parameters are very small so that the mass loss due to stellar evolution is also quite similar for the two samples.

Table 4.1: Parameters $a_{\rm ev}$, $b_{\rm ev}$, and $c_{\rm ev}$ for the red and blue GCs/UCDs.

	Z	$a_{\rm ev}$	$b_{\rm ev}$	$c_{\rm ev}$
red	0.0040	7.06	0.260	−1.80
blue	0.0004	7.06	0.265	−1.79

The parameters describing the mass loss in tidal fields are chosen the same as in Chap. 3.2: following Lamers et al. (2005a), $\gamma = 0.62$ is used and for the total disruption time of an SC with an initial mass of $10^4 M_\odot$, t_4, the values 3 Gyr, 6 Gyr, and 15 Gyr are assumed. This variation allows for testing how strongly the tidal field affects the overall mass functions. Since the values are the same as before, a direct comparison of the previous results and the outcome here is possible. Note that it appears reasonable to assume that blue GCs/UCDs have on average a larger t_4 since their spatial distribution is more extended as compared to red GCs/UCDs and thus, the influence of the tidal field is weaker for them.

After correcting the mass of each GC/UCD in the present-day mass functions (red and blue dashed lines in Fig. 4.6), the natal cumulative mass function are obtained for the red and blue GCs/UCDs as can be viewed in the lower left and middle panels, respectively, of Fig. 4.6. These mass functions are represented by red and blue thick, medium-thick, and thin continuous lines for t_4 of 3 Gyr, 6 Gyr, and 15 Gyr, respectively. As one can see, the natal cumulative mass functions are generally shifted to higher masses because SCs only lose mass in the course of time. Predominantly, this is caused by stellar evolution which influences all SCs in the same way since it is independent of the actual mass (cf. Eq. (3.2)). The different values for t_4 mainly affect the low-mass end of the cumulative mass functions because low-mass SCs are more susceptible for mass loss due to tidal forces than high-mass SCs are. For shorter t_4, every GC/UCD loses more mass in the course of time because short disruption times lead to higher mass loss. This trend was already seen in Fig. 3.2. Evidently, the mass loss is only a function of mass (cf. Eq. (3.1)) and therefore independent of the color of the GC. This is why for the same t_4, the influence on the low-mass end of the red and blue

GC mass function is the same as becomes clear from the bottom right panel in Fig. 4.6. Also, this panel includes the cumulative mass functions of all (i.e., red and blue) GCs/UCDs, marked with gray continuous lines, after correcting it for mass loss from Fig. 3.2 where the mass functions were drawn by blue, purple and orange continuous lines. As expected, it illustrates that the correction for mass loss only shifts the red, blue, and overall GC mass distribution in a particular way and preserves their relative positioning in the plot. As it has been mentioned in Chap. 4.5, the different low-mass limit is caused by the different depth of the photometric observations.

As discussed in Chap. 3.2, the mass functions corrected for stellar evolution and the influence of the tidal field (red and blue continuous lines in the lower panels of Fig. 4.6) surely do not represent the real natal mass functions of red and blue GCs/UCDs. While stellar evolution is well enough understood to account for, correcting for the influence of the gravitational potential is a challenging task: it does not only depend on the mass of the SC but also on the internal dynamical properties of the SC itself like the concentration or the orbit which is not known. Furthermore, the surrounding gravitational potential plays a crucial role. As mentioned above, blue GCs/UCDs are expected to be somewhat less influenced by the tidal field on average as compared to the red GCs/UCDs since the latter are more centrally concentrated on NGC 1399. Taking the color aside, dynamical evolution is least important for high-mass objects and they are also barely influenced by tidal forces (which is why the parameter t_4 has almost no effect), the corrected mass functions are most accurate at the high-mass end. At the low-mass end, the mass functions with $t_4 = 15$ Gyr (red and blue thin continuous lines in the lower panels of Fig. 4.6) represent the lower limit of the real natal mass functions because in this case, stellar and a minimum of dynamical evolution is accounted for. The slope at the low-mass end of the real natal mass functions is probably steeper than in the $t_4 = 15$ Gyr case since GCs/UCDs which are located closer to NGC 1399 will have a shorter t_4. Additionally, the method can only trace back the mass loss of GCs/UCDs that still exist but does not account for objects which have been destroyed in the course of time. Because of preferential disruption of low-mass SCs (e.g., Fall & Rees 1977; Okazaki & Tosa 1995; Elmegreen 2010), the number of low-mass objects is expected to be higher. And even if some of these SCs still exist it might not possible to observe them due to photometric completeness limits. This needs to be taken into account when interpreting results derived from the corrected mass functions which will be used for the analysis.

4.7 Decomposition of the red and blue GC/UCD mass functions into individual SC populations

The next step is to decompose the natal cumulative mass functions of red and blue GCs/UCDs into individual SC populations, each described by the ECMF (Eq. (2.15)). I proceed in the same way as in Chap. 3.3 and summarize the approach here briefly:

1. Select the (remaining) most massive SC, $M_{\rm ecl,max}$, in the mass distribution of red and blue GCs/UCDs and convert it into the theoretical upper mass limit, $M_{\rm max}$ (Eq. (2.24)). $M_{\rm max}$ determines:
   - the required SFR (Eq. (2.19)).
   - the ECMF (Eq. (2.15)) through normalization constant k (Eq. (2.10)). β is varied in the range from 1.7 to 2.5 and determines also the length of one SC formation epoch, δt (Chap. 2.5 and Table 2.1).
2. The derived ECMF is integrated downward to calculate the individual SC masses, M_i (Eqs. (2.6)–(2.7)), of the population formed during the same epoch as the most massive SC, $M_{\rm ecl,max}$.
3. All generated SCs (also from previous runs, if existing) are sorted according to their mass. Starting at the high-mass end, the masses of the most-massive, second most-massive, third most-massive, and so on, SC of the generated and observed distributions are compared pairwise to find that object in the generated sample which is less massive than its counterpart in the observed sample. This SC in the observed sample is regarded as the remaining most massive SC, $M_{\rm ecl,max}$. Thereafter the loop restarts.

As in Chap. 3.3, a deviation of up to five percent is allowed for when comparing the objects in the generated and the observed sample pairwise. With this, an overproduction of SCs that potentially do not have a counterpart in the observed sample is prevented since the aim is to reproduce the shape of the observed GC mass distribution and not to create exact matches between SCs in the generated and the observed sample.

The above method is applied to the natal cumulative mass functions of red and blue GCs/UCDs separately assuming that all objects in the two samples were formed in an SC formation process. Generally, the replicated mass functions look

essentially the same Fig. 3.4 apart from the fact that the mass functions here are separated into red and blue objects. Thus, the natal GC/UCD mass functions (blue and red continuous lines) as well as the replicated ones (light-blue and purple dotted lines) for the blue and red GC sample are only shown for $\beta = 2.0$ (green dashed lines) in the left and middle panel of Fig. 4.8. The results for the other β are almost the same apart from the fact that the low-mass tail of the replicated mass functions becomes steeper with increasing β.

It was argued in Chap. 3 that the most massive object of the entire sample, UCD3, has probably not formed in an SC formation process. Following this argumentation, the method was reapplied to red GC/UCD mass function after excluding UCD3 from it. The result is shown in the right panel of Fig. 4.8 where the natal GC/UCD mass functions are represented by yellow continuous lines while the replicated mass functions are drawn with brown dotted lines. In all cases, the thickness of the lines are a function of the parameter t_4 as introduced in Chap. 4.6.

As can be seen, the masses of SCs generated by the replication method match the mass distributions of the observed red and blue GCs/UCDs very well. However, there are two exceptions: first, at the low-mass end ($M < 10^6\ M_\odot$), there are more low-mass objects than are observed. The reason is that the observed mass functions flatten toward lower masses while the number of generated objects increases in the same way as the underlying ECMF does. At least a fraction of this deviation can be explained by the fact that low-mass objects which completely dissolved in the course of time are missing in the natal mass functions. This finding is independent of any parameter. Second, for the red GC/UCD sample including UCD3, the method generates at the high-mass end objects that are slightly more massive than actually observed. As was apparent from Fig. 3.4, this effect strengthens toward higher β because the underlying ECMF – parameterized by β – becomes steeper. This might be interpreted as a hint that UCD3 does not belong to the red GC/UCD sample since this discrepancy disappears completely as soon as UCD3 is excluded as can be seen in the right panel of Fig. 4.8. Both results were also observed in Chap. 3.

UCD3 might be not the only object that did not form in an SC formation process. In the dwarf galaxy threshing scenario, only the nucleus of a dwarf galaxy remains after its outer envelope was stripped. For this scenario, Pfeffer et al. (2016) estimated for a galaxy like NGC 1399 in the Fornax galaxy cluster the expected number of stripped nuclei and their mass. Their estimates were considered in Chap. 3 but are not taken into account here because it is not obvious how to divide the objects into red and blue sample to correct the red and blue mass functions separately. The consequences of this will be discussed in Chap. 4.9.2.

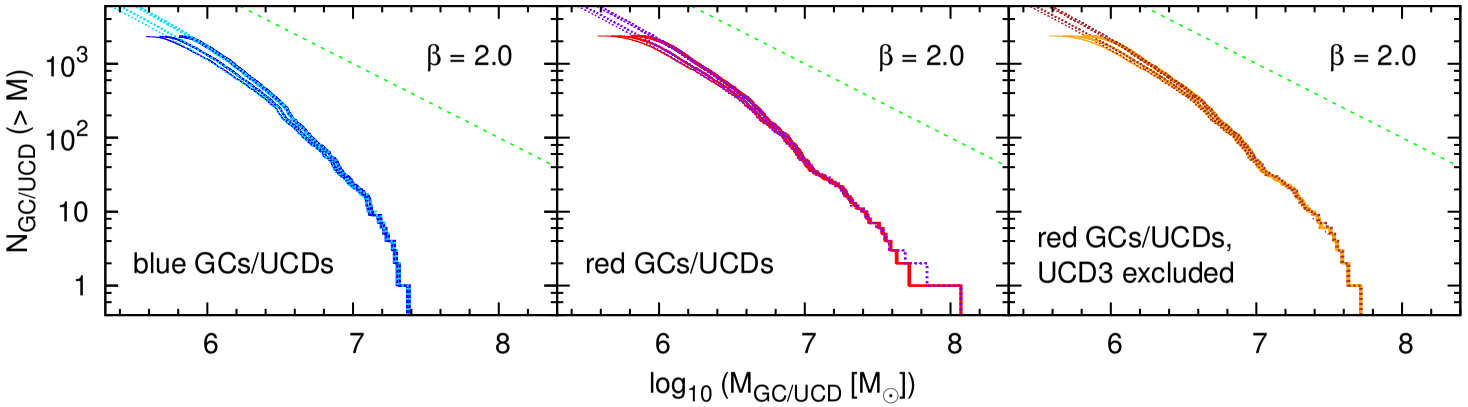

Figure 4.8: Corrected cumulative GC/UCD mass functions (blue, red, and yellow continuous lines) together with the replicated ones (light-blue, purple, and brown dotted lines) of the blue (left panel), the red (middle panel), and red sample without UCD3 (right panel) for $\beta = 2.0$ (green dashed lines). The thickness of the lines depend on the value of the parameter t_4 as in Fig. 4.6.

4.8 Distribution of necessary SFRs

During the decomposition of the observed mass functions into individual SC populations, the mass of the most massive object, $M_{\rm ecl,max}$, of each population was determined (first point in enumeration in Chap. 4.7). Converting this mass to an SFR (Eq. (2.25)) indicates which SFR was required to produce this SC and all other SCs of the same population. Taking the SFRs of all individual SC populations together reveals the distribution of necessary SFRs which is shown in Fig. 4.9 as a function of β: blue and red continuous lines represent the SFR distributions of the blue and red GC/UCD sample, respectively. The SFR distributions for the red GC/UCD sample but without UCD3 is shown in orange. For comparison, I plot the SFR distributions of the whole sample (but without UCD3) as shown in Fig. 3.6 (green lines there) in gray. Again, the thickness of the lines depend on the parameter t_4. For all cases, the key parameters (i.e. the total number of SC formation epochs (SCFEs), $N_{\rm SCFE,tot}$, the total SC formation time, $t_{\rm SCFE,tot}$, and the total stellar mass, $M_{\rm tot}$, formed during that time) are listed in Table 4.2.

Apparently, the distributions of required SFRs differ depending on β and the considered sample. My findings can be summarized as follows:

1. Considered sample:

    - The distribution of SFRs for the red GC/UCD sample is shifted to higher SFRs as compared to the one for the blue GC/UCD sample except for the highest β. If UCD3 is excluded from the red GC/UCD sample this is even valid for all β. This difference is expected because the blue GC/UCD sample is generally less massive than the red one (see bottom right panel of Fig. 4.6). The peak SFRs of the blue and the red GC/UCD sample without UCD3 are relatively similar and lie within $2.0 < \log_{10}(\mathrm{SFR}) < 4.0$ while the peak SFRs of the red GC/UCD sample including UCD3 are about half an order of magnitude higher and lie in the range between $2.7 < \log_{10}(\mathrm{SFR}) < 4.5$.
    - The number of formation epochs of the blue and red GC/UCD sample together gives approximately the SFR distributions of the whole GC/UCD sample (shown in gray in Fig. 4.9, taken from Fig. 3.6 for the case without UCD3, marked with green lines there). This also holds true in numbers: Adding the resulting values for $N_{\rm SCFE,tot}$, $t_{\rm SCFE,tot}$, or $M_{\rm tot}$ of the red and blue GC/UCD sample in Table 4.2 for a fixed β and t_4 gives a very similar value as determined in Table 3.2. The difference between the added values and the results from the previous work

amounts to about ±10% and increases with β. This confirms that the analyses in Chap. 3 and here are self-consistent.

2. UCD3: if UCD3 is excluded from the red GC/UCD sample the required SFR distributions change: since the highest-mass object is missing, the peak SFR decreases. Toward higher β, the distributions themselves change as well, in particular at the high-SFR end: if UCD3 is included the SFR drops about one order of magnitude or more after the highest SFR and decrease only slightly with increasing number of formation epochs. In contrast, if UCD3 is excluded the SFRs decrease gently while the number of formation epochs increase continuously. Toward the low-SFR end, the SFR distributions of the red GC/UCD sample with and without UCD3 become indistinguishable, except for the highest β. This is expected since only the high-mass end of the red GC/UCD mass function is changed while the low-mass part remains the same. While for the SFR distributions it is crucial whether UCD3 is included or not, the key parameters are only little influenced by UCD3 (cf. Table 4.2). This was already seen in Fig. 3.6 and in Table 3.2.

3. Dependence on β: with increasing β, the resulting SFRs increase generally from $\log_{10}(\mathrm{SFR}) \approx 0.5$ and 2.8 (between 3 and 600 $M_\odot \mathrm{yr}^{-1}$) for $\beta = 1.7$ to $\log_{10}(\mathrm{SFR}) \approx 2.0$ and 4.5 (between 100 and 30 000 $M_\odot \mathrm{yr}^{-1}$) for $\beta = 2.5$. At the same time, the number of formation epochs decreases (cf. Cols. 4, 7, and 10 in Table 4.2). This is valid independent of the considered sample. The reason for the former is the used relation between the SFR and the upper mass limit for SC, M_{max} (Eq. 2.19). As can be seen in Fig. 2.2, higher β lead to higher SFR for the same M_{max}. The reason for the latter is that with increasing β the underlying ECMFs become steeper so that every SC population contains more SCs which in turn means that fewer formation epochs are required. The same trend was observed in Fig. 3.6 and in Table 3.2.

4. Dependence on t_4: The SFR distributions develop into three different tails at the low-SFR end; the smaller t_4 the steeper the tail. Since smaller t_4 lead to higher masses in the low-mass tail of the red and blue GC/UCD mass functions (Fig. 4.6), this translates into higher SFRs and/or more formation epochs in the low-SFR tail of all distributions (cf. Table 4.2). Therefore, with increasing t_4, the values for $N_{\mathrm{SCFE,tot}}$, $t_{\mathrm{SCFE,tot}}$, and M_{tot} decrease. This was also found in Table 3.2.

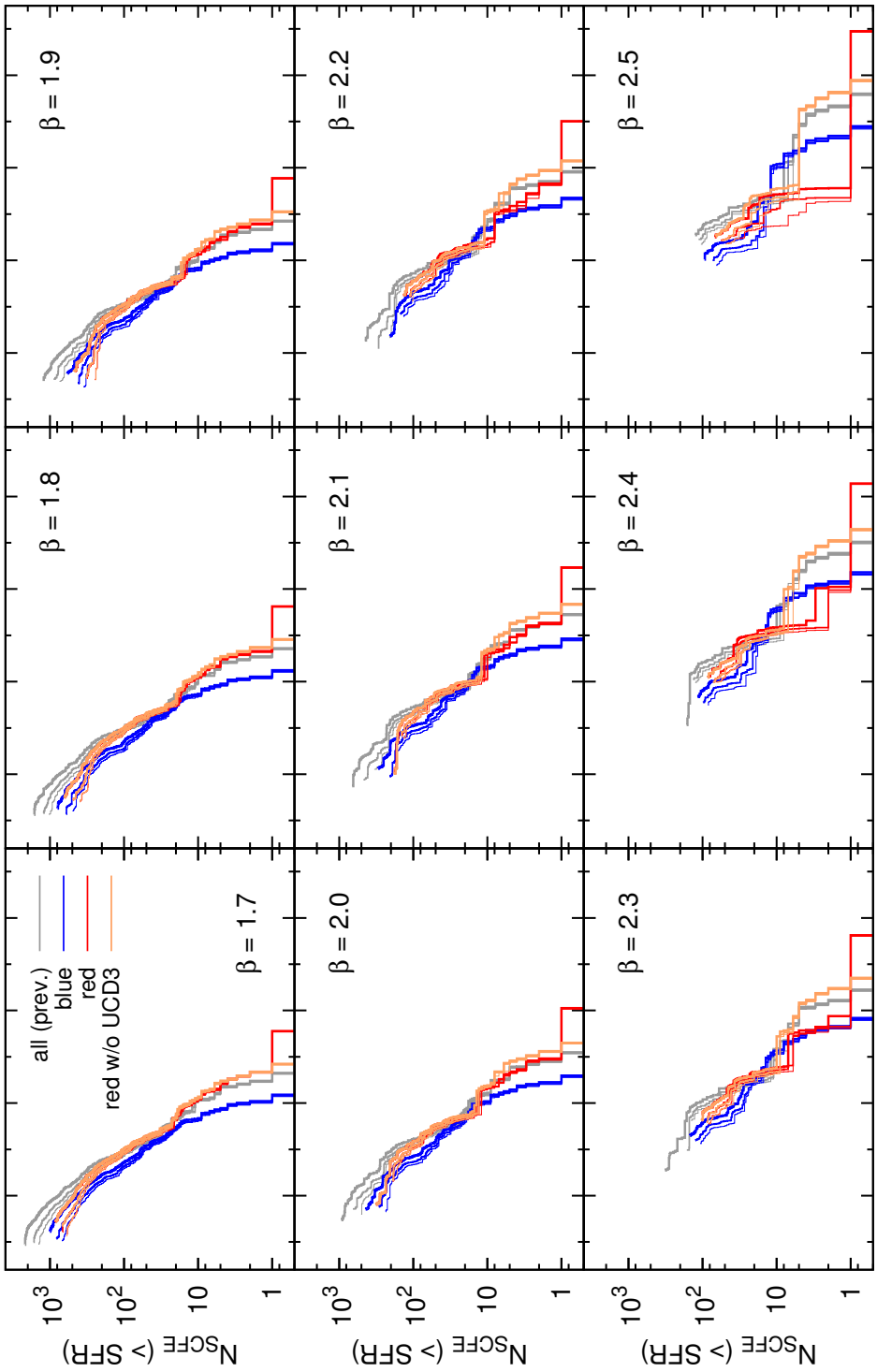

Figure 4.9: The cumulative number of SC formation epochs (SCFEs) as a function of the SFR for the blue, and red GCs/UCDs as well as the red GCs/UCDs after excluding UCD3 (blue, red, and orange continuous lines). For comparison, the same is plotted for the whole sample of GCs/UCDs but without UCD3 from Fig. 3.6 (green lines there) in gray. The thickness of the lines depend on the value of the parameter t_4 as in Fig. 4.6.

Following the argumentation in Chap. 3.3, UCD3 is not regarded as a genuine SC and thus, the results for the case when UCD3 is excluded from the red GC/UCD sample is considered as more reliable. Even though the differences in $N_{\mathrm{SCFE,tot}}$, $t_{\mathrm{SCFE,tot}}$, or M_{tot} are minor (Table 4.2), the SFR distributions change substantially, in particular at the high-SFR end (Fig. 4.9). This is also the reason why those resulting SFR distributions from Chap. 3.4 and Fig. 3.6 are shown where UCD3 has been excluded from the whole GC/UCD sample (gray continuous lines in Fig. 4.9). Taking this into account, the peak SFRs of the red GC/UCD sample range between 300 and 10 000 $M_{\odot}\mathrm{yr}^{-1}$ and are approximately half a magnitude higher than the peak SFRs of the blue GC/UCD sample which lie between 100 and 3 000 $M_{\odot}\mathrm{yr}^{-1}$. These numbers depend on the parameter β. For the most commonly observed β of around 2.0 in young SCs (e.g., Zhang & Fall 1999; Lada & Lada 2003; McCrady & Graham 2007; Chandar et al. 2011; Linden et al. 2017), the peak SFRs are about 200 and 400 $M_{\odot}\mathrm{yr}^{-1}$ for the blue and red GC/UCD sample, respectively.

Apart from the highest values of β, the SFR distributions flatten toward the low-SFR end, independent of the considered sample or the parameter t_4. SFRs at the low-SFR end lead to the formation of SCs lying at the low-mass end. As noted in Chap. 4.6, it is very likely that this part of the mass function is incomplete due to the preferential destruction of low-mass SCs which is why I suspect the SFR distributions to be steeper at the low-SFR end. If the real SFR distributions were indeed steeper, it is interesting to see that they can approximately be fitted by straight lines, meaning that the quantity SFR is roughly distributed according to a power law. It has been shown in Schulz et al. (2015) that such SFR distributions lead to a steepening of the overall mass functions of all GCs/UCDs at the high-mass end in a similar way as it is observed around NGC 1399. It would be an interesting finding if the SFRs during the formation of the GCs/UCDs around NGC 1399 were indeed distributed according to a power law since the parental distribution functions of the masses of SCs in a SC population (ECMF) as well as the masses of stars in SCs (initial mass function, IMF) are also described as power laws.

4.9 Discussion

Since this work is a follow-up of Chap. 3 all general aspects regarding the assumptions and uncertainties discussed there (Chap. 3.5.1) are applicable here as well. Thus, I concentrate the discussion on the consequences induced by the color

Table 4.2: The total number of SC formation epochs (SCFEs), $N_{\rm SCFE,tot}$, the total SC formation time, $t_{\rm SCFE,tot}$, and the total stellar mass, $M_{\rm tot}$, formed during that time for the three different approaches as a function of t_4 (Col. 1) and β (Col. 2). These quantities are listed for the blue GC/UCD sample in Cols. 4–6, for the red GC/UCD sample in Cols. 7–9, and for the red GC/UCD sample without UCD3 in Cols. 10–12. For reference, the length of one SC formation epoch, δt, is listed in Col. 3 as determined in Chap. 2.5 (see Table 2.1.

			blue GC/UCD sample			red GC/UCD sample			red GC/UCD sample without UCD3		
t_4	β	δt [Myr]	$N_{\rm SCFE,tot}$	$t_{\rm SCFE,tot}$ [Gyr]	$M_{\rm tot}$ [10^{10} $M_\odot$]	$N_{\rm SCFE,tot}$	$t_{\rm SCFE,tot}$ [Gyr]	$M_{\rm tot}$ [10^{10} $M_\odot$]	$N_{\rm SCFE,tot}$	$t_{\rm SCFE,tot}$ [Gyr]	$M_{\rm tot}$ [10^{10} $M_\odot$]
3 Gyr	1.7	0.77	1000	0.77	0.98	840	0.64	1.21	838	0.64	1.20
	1.8	1.11	792	0.88	1.27	634	0.70	1.54	637	0.71	1.53
	1.9	1.70	583	0.99	1.80	463	0.79	2.17	477	0.81	2.17
	2.0	2.80	439	1.23	2.95	319	0.89	3.52	320	0.90	3.51
	2.1	4.94	299	1.48	5.58	178	0.88	6.61	183	0.90	6.61
	2.2	9.31	205	1.91	12.34	137	1.27	16.08	135	1.26	15.95
	2.3	18.57	147	2.73	32.11	100	1.86	43.29	104	1.93	43.64
	2.4	38.77	117	4.54	92.65	85	3.30	133.40	85	3.30	133.11
	2.5	83.77	94	7.87	285.52	68	5.70	430.23	67	5.61	427.35
6 Gyr	1.7	0.77	821	0.63	0.78	678	0.52	1.00	684	0.52	1.00
	1.8	1.11	606	0.67	1.00	489	0.54	1.26	488	0.54	1.25
	1.9	1.70	415	0.71	1.38	321	0.55	1.74	325	0.55	1.73
	2.0	2.80	291	0.81	2.24	190	0.53	2.80	190	0.53	2.78
	2.1	4.94	210	1.04	4.31	145	0.72	5.67	146	0.72	5.66
	2.2	9.31	150	1.40	9.89	112	1.04	13.62	113	1.05	13.60
	2.3	18.57	125	2.32	26.50	86	1.60	37.25	88	1.63	37.35
	2.4	38.77	98	3.80	75.96	69	2.67	112.82	72	2.79	113.78
	2.5	83.77	73	6.12	229.07	56	4.69	365.28	55	4.61	363.47
15 Gyr	1.7	0.77	690	0.53	0.68	590	0.45	0.90	594	0.45	0.89
	1.8	1.11	492	0.55	0.85	394	0.44	1.11	398	0.44	1.10
	1.9	1.70	351	0.60	1.20	247	0.42	1.53	246	0.42	1.52
	2.0	2.80	236	0.66	1.93	167	0.47	2.53	168	0.47	2.52
	2.1	4.94	163	0.80	3.72	134	0.66	5.21	137	0.68	5.22
	2.2	9.31	136	1.27	8.82	100	0.93	12.38	104	0.97	12.48
	2.3	18.57	107	1.99	23.20	83	1.54	34.54	81	1.50	34.22
	2.4	38.77	84	3.26	66.71	65	2.52	103.79	63	2.44	102.83
	2.5	83.77	65	5.45	203.35	48	4.02	328.87	48	4.02	329.13

selection I applied to the spectroscopic and photometric sample to obtain a separate red and blue GC/UCD sample. The additional assumptions are discussed in Chap. 4.9.1, the plausibility of the results in Chap. 4.9.2 and their implications for the assembly of NGC 1399 in Chap. 4.9.3.

4.9.1 Assumptions

The selection of the spectroscopic sample was mainly based on the location of each object in color space (see Figs. 4.2 and 4.3). Objects which were located further away from the main body of data points were examined individually and excluded if they had unreasonable values for the parameters FWHM and "class", and/or suspicious appearance in optical images.

For the selection of the photometric sample, it was assumed explicitly that GC candidates will lie in the same color space as the objects in the spectroscopic sample and have reasonable FWHM and "class" values. However, in particular for the bands g, r, and i, the distinction is rather sharp: I included only objects with a weighted logarithmic probability above -5 which corresponds to the outermost greenish contour in Fig. 4.5. Considering how densely the objects are populated at the edge, it appears feasible that some of the GC candidates may lie outside the adopted boundaries, in particular since a few objects from the spectroscopic sample are also lying outside (Fig. 4.4). Thus, some of the objects marked in gray in Fig. 4.5 could be GCs. However, if for the photometric sample the relative amount of objects lying outside is similar to the spectroscopic sample, their relative fraction should be low which is why they should not influence the results too much. On the other hand, objects in the photometric sample that match the selection criteria do not have to be necessarily GCs but could be contaminating foreground stars or background objects instead.

The color selection relied on the assumption that the GCs/UCDs around NGC 1399 have a bimodal color distribution and are thus separable into two samples. I would argue that this is well justified since a bimodality is clearly seen in the spectroscopic as well as the photometric sample as shown by the contours in the Figs. 4.4 and 4.5. Still, it should be taken into account that in terms of color, referring to red and blue GCs/UCDs as two detached samples would not be accurate because they are continuously distributed in color space and the two Gaussians profiles overlap significantly even though there is a dip between the red and blue peak. However, if taking the kinematical properties of the GCs into account, Schuberth et al. (2010) showed in their Fig. 20 that the velocity dispersion changes significantly as a function of color which justifies the classification in two physically different samples (see Chap. 4.9.3 for more details).

It is generally believed that the fluent transition between red and blue objects is accompanied with a change in metallicity. Often, a linear relation between color and metallicity is implicitly presumed which would translate a continuous distribution into color space in a continuous distribution in metallicity. However, there is growing evidence for a color-metallicity nonlinearity (e.g., Richtler 2006; Yoon et al. 2006; Blakeslee et al. 2012; Chung et al. 2016). Nevertheless, it is known that in the central Fornax galaxy cluster, red GCs/UCDs are more metal-rich as compared to blue GCs/UCDs on average (Chap. 4.6). Even though metallicity and age could be related to each other, a spread in color and metallicity does not have to be accompanied by a spread in age. Naively, one could assume that red GCs/UCDs are younger than blue GCs/UCDs since it took some time to enrich the gas with metals. On the other hand, the opposite may be true in a scenario where the red GCs/UCDs are associated with the very early and rapid starburst which formed the central spheroid of NGC 1399 and led to quick self-enrichment, while the blue GCs/UCDs formed later from infalling and interacting gas-rich but metal-poor young galaxies. However, there is no need to invoke an age difference between the red and blue GCs/UCDs because they could have formed simultaneously but spatially separated, for instance like in the previous scenario with the difference that the blue GCs/UCDs formed at the same time as the red ones and were later accreted together with their host galaxies. This is the reason why I did not presume any age difference and took an age of 13 Gyr for both samples.

Also, it needs to be taken into account that due to the distance cut of 160 kpc the GC/UCD sample comprises the GCs/UCDs of close neighboring galaxies like NGC 1404 or NGC 1387. These two galaxies are much smaller and have by far less GCs/UCDs than NGC 1399 which is why they have relatively low specific frequencies between 2 and 4 while the specific frequency of NGC 1399 is around 12 (e.g., Richtler et al. 1992; Kissler-Patig et al. 1997). It is likely that these galaxies lost some of their GCs/UCDs that led to the build-up of the halo of GCs/UCDs around NGC 1399. This process is not restricted to these two galaxies only. Most probably, the reason for the GC/UCD system around NGC 1399 being so rich is that in the past, many other galaxies contributed their GCs/UCDs in the same way. In that respect, the GC/UCD system around NGC 1399 is an accumulation of many individual GC/UCD populations to which NGC 1404 or NGC 1387 will eventually dispense all their GCs/UCD.

4.9.2 Results

The main findings of this investigation are the resulting SFR distributions for the red and blue GC/UCD sample shown in Fig. 4.9. They appear to be reasonable

since they are very similar to the SFRs found in Chap. 3.4 and Fig. 3.6 which were in agreement with estimates from the literature. Thus, all aspects discussed there should be valid here as well. In addition, more recent investigations confirmed that SFRs of up to several thousands $M_{\odot}\mathrm{yr}^{-1}$ are reasonable for galaxies undergoing a violent starburst at high redshifts (e.g., Riechers et al. 2013, 2017; Kriek et al. 2016; Ma et al. 2016). Observing massive, quiescent galaxies at somewhat later epochs gives essentially the same estimates for the SFR at the time of their formation (e.g., Glazebrook et al. 2017, their Fig. 2) while submm galaxies have slightly lower SFR of up to thousand $M_{\odot}\mathrm{yr}^{-1}$ (e.g., Michałowski et al. 2017, their Fig. 2). This fits well into the general picture of the cosmic star formation history in which the SFR increases with redshift, reaching 10^2 $M_{\odot}\mathrm{yr}^{-1}$ at $z \approx 2$ and about 10^4 $M_{\odot}\mathrm{yr}^{-1}$ for $z > 6$ (e.g., Madau & Dickinson 2014, their Fig. 1).

As noted in Chap. 4.4, the mass determination of the red and blue GCs/UCDs depends strongly on the considered evolutionary model, the used filters and the assumed age. They were chosen such that they are consistent with the previous investigations in Chap. 3.1. Since the relation between mass and SFR is roughly linear (Eq. 2.19) a variation of 0.4 dex in mass (Chap. 4.4) leads to approximately the same variation in SFR. As can be seen in Fig. 4.7, the age of the red and blue GCs/UCDs has the least impact on the mass functions. Thus, the SFR distributions will not depend much on the exact age of the red and blue GCs/UCDs – as long as they are assumed to be old. Consequently, more precise age measurements as well as the knowledge in which order they formed would barely change the SFR estimates even though they would certainly help to assess different formation scenarios. In this respect it is important to note that any formation scenario should be able to explain why the mass functions – and hence the SFR distributions – for the red and blue GCs/UCDs are offset to each other.

As mentioned in Chap. 4.7, I did not consider that other objects apart from UCD3 which did not form in an SC formation process might contaminate the red and blue GC/UCD sample. The expected number of objects stemming from the dwarf galaxy threshing scenario by Pfeffer et al. (2016) was not taken into account because it is not straight-forward to divide their sample of stripped nuclei into red and blue objects. Since the contribution of stripped nuclei is expected to be most important at the high-mass end, some of the high-mass GCs/UCDs might be unrecognized nuclei of dwarf galaxies. Excluding them from the red and blue GC/UCD sample would result in slightly lower peak SFRs while the distributions of SFR as a whole would not be influenced much since only the high-mass part of the mass function is changed. However, my investigations in Chap. 3.4 where the stripped nuclei sample was taken into account showed that the resulting distribution of SFRs were quite similar to the SFR distribution where

only UCD3 was excluded (see Fig. 3.6). Thus, the influence on the examination here is not expected to be major apart from lower peak SFRs by a factor of less than 2 since the maximum difference in the SFR was less than 0.3 dex.

Along with the SFR distributions, the total number of SC formation epochs, $N_{\mathrm{SCFE,tot}}$, the total SC formation time, $t_{\mathrm{SCFE,tot}}$, and the total stellar mass, M_{tot}, formed during that time, were determined for each sample (Table 4.2). As mentioned in Chap. 4.8, adding the individual values obtained for the red and blue GC/UCD sample for a fixed t_4 and β gives approximately the same as found in Table 3.2, proving that new and previous results are consistent. In terms of $t_{\mathrm{SCFE,tot}}$ and M_{tot}, the findings have to be in agreement with the constrains set by the age and the total mass of NGC 1399 and the surrounding GCs/UCDs. Note that the sum of M_{tot} for the red and blue GCs/UCDs represents a lower limit for the total mass of the whole system while the total SC formation time might be shorter than the sum of $t_{\mathrm{SCFE,tot}}$ for red and blue GCs/UCDs because the two samples might have formed simultaneously at different places (e.g., red and blue GCs/UCDs formed concurrently but spatially separated).

NGC 1399 has a total stellar mass of at least $6 \cdot 10^{11}\ M_{\odot}$ (Richtler et al. 2008; Iodice et al. 2016) while the GCs/UCDs have an age of more than 8 Gyr (see Chap. 3.1). These two constraints put an upper limit on the total mass and the total SC formation time of the overall GC/UCD sample: adding the values for M_{tot} and $t_{\mathrm{SCFE,tot}}$ of the red and blue sample, respectively, shows that only $\beta \lesssim 2.2$ is allowed mostly independent of t_4. As mentioned in Chap. 4.8, it almost does not play a role whether the results for the red sample with or without UCD3 are used (apart from the highest β, see Table 4.2). Higher values of β would only be possible if the corresponding value for δt would be lower and/or a fraction of the SC formation events occurred simultaneously but at different places, and not in a consecutive manner as presumed. However, both approaches would only shorten the total formation time but would not reduce the total mass. One possible solution to circumvent the excess in the mass would be an adjustment of the lower mass limit for a SC, M_{min}, which was assumed to be 5 $M_{\odot}$. If this mass would be higher, less stellar mass would be produced in each formation epoch when populating the ECMF (Eq. (2.17)). Since less stellar mass would be formed in this case, the required SFRs would be lower (cf. Eq. (2.19)).

However, there is no strong necessity for $\beta \gtrsim 2.2$ to be valid since in young SCs, $\beta \approx 2.0$ is usually found in observations (e.g., Zhang & Fall 1999; Lada & Lada 2003; McCrady & Graham 2007; Chandar et al. 2011; Linden et al. 2017). Furthermore, in their simulations of GC formation, Kravtsov & Gnedin (2005) found that the mass function of GCs at their birth can be approximated by a power

law with $\beta \approx 2.0$. The highest and lowest β are rarely observed and were here only considered to avoid any restrictions in β and to see independently which values are favored by the analysis. It turned out that favorite values for β match nicely what is observed in young massive SCs.

4.9.3 Formation of NGC 1399 and its red and blue GC/UCD system

Many studies in the past tackled the question of the formation of elliptical galaxies (e.g., Gott 1975; Larson 1975; Kormendy 1989) and the formation of GCs (e.g., Fall & Rees 1985; Murray & Lin 1992; Brown et al. 1995). Ellipticals may form in a monolithic collapse (e.g., Eggen et al. 1962) or in a merger of two (gas-rich spiral) galaxies (e.g., Lilly et al. 1999; Kilerci Eser et al. 2014). During the latter, at least part of a GC system might be formed (Ashman & Zepf 1992). However, it has been pointed out early that this formation scenario does not apply to central cluster galaxies like NGC 1399 (Ostrov et al. 1993; see also Forbes et al. 1997). Still, even though the merger model by Ashman & Zepf (1992) does not offer an adequate description for the formation of red and blue GCs/UCDs, there are signs hinting at an interaction of NGC 1399 and its GC/UCD system with nearby galaxies: Bassino et al. (2006a) detected two tails of blue GCs from NGC 1399 to NGC 1404 and NGC 1387, respectively. This finding was confirmed by Kim et al. (2013); later, D'Abrusco et al. (2016) reported about an even bigger asymmetric density enhancement of GCs along the W−E direction from which the authors followed that the core of the Fornax cluster experienced a lively history of interactions. Moreover, Iodice et al. (2016) detected a faint stellar bridge in the intracluster region on the west side of NGC 1399. Also, the center of the inner GC distribution and the optical center of NGC 1399 are offset by about 0.5 arcmin (corresponding to almost 3 kpc) indicating that NGC 1399 is not yet virialized (Kim et al. 2013). However, NGC 1399 itself does not show any signatures of a (recent) merger event (Tal et al. 2009).

So, the question remains how giant ellipticals acquire their GC system. The work by Forbes et al. (1997) and Côté et al. (1998) focused on this aspect which is why I discuss their models in more detail. Forbes et al. (1997) suggested that the vast majority of GCs around gE and cD galaxies have formed in situ and speculated that the formation occurred in two distinct phases with gas of differing metallicity, explaining thereby the bimodal GC metallicity distribution. The metal-poor GCs are formed first during the collapse of the protogalactic cloud,

while the metal-rich GCs formed from enriched gas and at roughly the same time as the stars of the galactic spheroid. Moreover, tidally stripped GCs from nearby galaxies might contribute to the GC system in the outer parts of the host galaxy. Côté et al. (1998) argued that metal-rich GCs represent the galaxy's intrinsic GC system, while the metal-poor GCs are captured from other galaxies through mergers or tidal stripping. Hilker et al. (1999a) investigated under which circumstances this is possible for the case of the Fornax galaxy cluster.

The model by Forbes et al. (1997) is appealing because it naturally explains where the enriched material comes from, out of which the metal-rich GCs form, but it does not explain why the GC formation occurred in exactly two phases. Forbes et al. (1997) assumed that if only a small fraction of the available gas is consumed during the first SC formation episode, this allows a further collapse of the remaining, now metal-enriched gas. This might be counted as a hint why the necessary SFRs to form blue GCs/UCDs are generally lower than the ones for the red GCs/UCDs (cf. Fig. 4.9). From the observational point of view, it stands out that the formation of the metal-rich GCs is closely related to the formation of the stars in NGC 1399: the radial number density profile of red GCs can be scaled in such a way that it is virtually identical to the surface brightness profile of NGC 1399 (Schuberth et al. 2010, their Fig. 15; see also their Sect. 11.1.1.), hinting at a common formation process. Indeed, according to my analysis it is completely conceivable that from all the SCs formed during the metal-rich star burst only the most massive survived – today observable as GCs and UCDs – while all the lower-mass ones dissolved and contributed their stars to the stellar body of NGC 1399. This is in line with Forbes et al. (1997), who assumed that the vast majority of field stars and the metal-rich GCs form simultaneously and would naturally explain – at least qualitatively – why the radial profiles of red GCs and NGC 1399 are so similar, why the present-day GC/UCD mass function is a Gaussian (see e.g., Hilker 2009a, their Figs. 4 and 5; Mieske et al. 2012) and why only a tiny fraction of less than 1% of the stellar mass of NGC 1399 is retained in GCs/UCD.

Still, the origin of the blue GCs/UCDs is not entirely clear. Côté et al. (1998) pointed out that generally, the metal-poor GCs show only weak correlations with the host galaxy. Schuberth et al. (2010, see also Richtler et al. 2004) carried out a detailed analysis to determine different properties of the red and blue GCs. The red GCs are well-behaved in many ways: Their velocity distribution can be described by a Gaussian, the radial velocity dispersion profile is smooth and they show only a marginal rotation (if at all) which is in agreement with a weak rotation of the stellar body of NGC 1399 (Saglia et al. 2000). In contrast to that, the blue

GCs have a more complex velocity structure: some of them have very high/low (line-of-sight) velocities suggesting very large apogalactic distances. Also, the blue GCs sample as a whole tends to avoid the systemic velocity of NGC 1399 which is why its velocity distribution does not resemble a Gaussian. Moreover, blue GCs exhibit a systematically higher velocity dispersion than the red GCs and the radial velocity dispersion profile is not really smooth. At radii between 22 and 44 kpc, blue GCs show a significant rotational signal. Not only these peculiarities of the blue GCs were the reason why many studies suggested that NGC 1399 acquired its blue GCs/UCDs through stripping or accretion (e.g., Hilker et al. 1999b; Bassino et al. 2006a,b; Schuberth et al. 2010; D'Abrusco et al. 2016). As mentioned above, there are several hints of interactions of NGC 1399 with its close-by neighboring galaxies. However, it is not obvious whether NGC 1399 stripped blue GCs from the neighboring galaxies or whether the neighboring galaxies accreted blue GCs from the outer region of NGC 1399 (cf. Bassino et al. 2006b vs. Kim et al. 2013). From a theoretical perspective, the deeper potential of central giant elliptical should strip GCs from the surrounding satellites as shown by Bekki et al. (2003b) when simulating the infall of NGC 1404 onto NGC 1399. In that respect, it is interesting to note that the Gaussian color distribution of the red GCs/UCDs is narrower than the one of the blue GCs/UCDs (Fig. 4.4). This could be interpreted such that the formation conditions of the blue GCs/UCDs varied more strongly than for the red GCs/UCDs.

Regarding the formation timescale, things appear to be more well-arranged: giant ellipticals like NGC 1399 are expected to have formed early on in a relatively short timescale, as suggested by the "downsizing" picture in which the most massive systems require the shortest formation time (e.g., Cowie et al. 1996; Thomas et al. 1999; Juneau et al. 2005; Recchi et al. 2009; Citro et al. 2016; Pacifici et al. 2016; Glazebrook et al. 2017) while low-mass galaxies which are more metal-poor formed with lower SFRs over a longer timescale. Furthermore, in simulations by Kravtsov & Gnedin (2005) GC formation happens within the first few Gyr, that means essentially at the same time. This is in agreement with the stellar age of NGC 1399 which is about 11.5 ± 2.4 Gyr (Trager et al. 2000) as well as the age between 8 and 13.4 Gyr of the GCs/UCDs (Forbes et al. 2001; Kundu et al. 2005; Hempel et al. 2007; Firth et al. 2009; Chilingarian et al. 2011; Francis et al. 2012). Even though the age estimates of the GCs/UCDs are too uncertain to deduce in which order the objects formed or to constrain how the GC/UCD system assembled, for the analysis, the exact ages of the GCs/UCDs have only little influence on the SFR distribution as long as they are assumed to be very old.

I can definitively say that the red GCs/UCDs require generally higher SFRs as compared to the blue GCs/UCDs. The peak SFRs for both samples lie between several hundreds and several thousands $M_{\odot}\mathrm{yr}^{-1}$ while the difference between the red and blue sample is between 30% and half of an order of magnitude (i.e. a factor of about 3). It is also known that red GCs/UCDs around NGC 1399 have an approximately ten times higher metallicity content than the blue GCs/UCDs (Chap. 4.6). This raises the question whether the found difference in the SFRs is enough to explain the difference in metallicity since the SFRs are generally very high for both, red and blue GCs/UCDs. Furthermore, any conceivable formation scenario has to be able to explain this circumstance.

As mentioned in Chap. 4.9.1, it is not evident in which order the GCs/UCDs formed: red and blue sample could have formed simultaneously or one after the other. Likewise, it is also not obvious where they formed. However, based on the above mentioned observations, it seems reasonable to assume that the red GCs/UCDs formed together with the stellar body of NGC 1399 while the formation of the blue GCs/UCDs is not necessarily related to the central spheroid of the giant elliptical. A feasible formation scenario could be that blue GCs/UCDs formed in or around much smaller, metal-poor galaxies with shallow potential wells that were not able to keep much of the enriched material and therefore stayed metal-poor. This could have happened as they fell into the forming galaxy cluster while or after the initial major star burst which formed NGC 1399 and its associated red GCs/UCDs. It could also be that the blue GCs/UCDs were accreted or stripped off by NGC 1399 at later epochs. Even though the SFR distributions deduced here cannot reveal the formation process as a function of time, they uncover the conditions during the formation.

Chapter 5

Conclusions and Outlook

In this final chapter, I first summarize the approach and the resulting SFR distributions, and discuss based on them the implications for the formation of NGC 1399 and its GC/UCD system in Chap. 5.1. Then, I focus on the presented methods used for the analysis by reviewing their strengths in Chap. 5.2 and discussing possible improvements in Chap. 5.3. Finally, I close my thesis with an outlook and future prospects in Chap. 5.4.

5.1 Findings regarding the red and blue GCs/UCDs around NGC 1399

In the present thesis, a method was introduced with which it is possible to reconstruct under which conditions in terms of SFRs a sample of GCs/UCDs formed based on their mass function. For this, the present-day GC/UCD mass function has to be corrected for mass loss since their birth for which a model by Lamers et al. (2005a) was used. This model considers the mass loss due to stellar evolution and due to the variable strength of the tidal field, parameterized with t_4 (Chap. 3.2). Applying the corrections to the present-day mass function yields the natal GC/UCD mass function which was then decomposed into individual SC populations. Each of these SC populations is described by a power-law ECMF with a truncation beyond the most massive SC of the population, $M_{\rm ecl,max}$ (Chap. 2.2). To obtain all required SFRs, $M_{\rm ecl,max}$ of each SC population was converted to an SFR using the SFR–$M_{\rm ecl,max}$ relation (Chap. 2.5).

This method was applied to the rich GC/UCD system around NGC 1399 to unravel their formation conditions and gain insights into how the host galaxy it-

self formed. The analysis was carried out in two different ways: in Chap. 3, I first considered already available data on the GC/UCD system and calculated the required SFR distributions based on three different assumptions: (a) all objects in the GC/UCD sample are the result of an SC formation process, (b) the most massive object in the sample, UCD3, is not a genuine SC and is therefore excluded from the GC/UCD sample, and (c) the expected contribution of stripped nuclei as estimated by Pfeffer et al. (2014) is excluded from the GC/UCD sample. Second, in Chap. 4, I used new data to update the mass function of the GCs/UCDs around NGC 1399. With that, luminosities in the g, r, i, and u band became available allowing me to separate all GCs/UCDs into a red and a blue sample. The two color samples were then analyzed separately to determine their individual SFR distributions. In the second analysis, one extra case was considered: again, it was assumed that UCD3 did not form in an SC formation process and was excluded from the red GC/UCD sample. Thus, in total I analyzed three cases: (a) whole blue GC/UCD sample, (b) whole red GC/UCD sample, and (c) whole red GC/UCD sample but without UCD3. Here, the estimated number of stripped nuclei by Pfeffer et al. (2014) was not used in an additional case because the colors of the simulated stripped nuclei are not known per se. However, in combination with the first analysis, I will discuss below to which extent the exclusion of the stripped nuclei would change the required SFRs and thus alter the results for red and blue GCs/UCDs.

My results can be summarized as follows:

1. The resulting SFR distributions are remarkably similar among the two approaches and depend predominantly on the index β of the underlying ECMF (Eq. (2.15)). Generally, larger β lead to higher SFRs. The second most important influence whether and which objects are excluded from the samples at the high-mass end. This alters the high-SFRs end of the SFR distributions. The parameter t_4 affects the SFR distributions least and causes only changes at the low-SFR end.

2. If considering all GCs/UCDs irrespective of their color, the required peak SFRs lie within $2.0 < \log_{10}(\mathrm{SFR}) < 4.5$, corresponding to an SFR range from 100 to 30 000 $M_{\odot}\mathrm{yr}^{-1}$, and depend highly on β (Fig. 3.6).

3. After dividing the GCs/UCDs into a red and a blue sample, the peak SFRs of the red sample are essentially the same as for the case with all GCs/UCDs. Since blue GCs/UCDs are less massive than red ones, blue GCs/UCDs re-

quire generally lower peak SFRs. They lie within $2.0 < \log_{10}(\mathrm{SFR}) < 3.5$, corresponding to an SFR range from 100 to 3 000 $M_{\odot}\mathrm{yr}^{-1}$ (Fig. 4.9).

4. For each of the above cases, the total time of SC formation, $t_{\mathrm{SCFE,tot}}$, and the total stellar mass, M_{tot}, was derived from the analysis (Tables 3.2 and 4.2). The age of the GCs/UCDs (certainly above 8 Gyr, likely above 10 Gyr) as well as the present-day stellar mass of NGC 1399 (at least $6 \cdot 10^{11}$ $M_{\odot}$) set constraints on $t_{\mathrm{SCFE,tot}}$ and M_{tot}. This allows only cases with $\beta < 2.3$.

I would like to discuss these findings in terms of their reliability and how the stripped nuclei sample would influence them.

How reliable are the resulting SFR distributions (Figs. 3.6 and 4.9)?
This question comprises two aspects: the reliability of the SFRs (x-axis) and the number of formation epochs (y-axis). First, the uncertainty in the derived SFRs comes on one hand from the uncertainty in the mass determination of around 20% (Chap. 3.5.2) which rises up to a factor of less than 2 if also an uncertainty in age is considered (Chap. 4.4, Fig. 4.7). On the other hand, there is an uncertainty in the conversion from a mass into an SFR which is roughly half an order of magnitude (Fig. 2.2), corresponding to a factor of about 3. So, at most, the determined SFRs could be incorrect by a factor of 6 but they are certainly of the right order of magnitude. As discussed in Chaps. 3.5.2 and 4.9.2, the values themselves appear very reasonable.

Second, the number of formation epochs can be considered to be robust at the high-SFR end since it corresponds to the high-mass end of the GC/UCD mass function which is reliable because the objects there have been individually confirmed as GCs by radial velocity measurements. Toward the low-SFR end, the number of SC formation epochs represents a lower limit because it is likely that toward the low-mass end, the GC/UCD mass function becomes incomplete. One reason is the photometric completeness limit which might not allow for observations of GCs/UCDs of lower masses. Another reason is that less massive GCs have higher disruption probabilities so that a fraction of them have been destroyed in the meanwhile. It is expected that the relative number of disrupted GCs increases with decreasing GC mass. Thus, an increasing number of GCs is missing toward the low-mass end of the present-day mass function. When correcting for mass loss, only objects were considered that survived until today but there is no measure for how many objects were destroyed in the course of time. Consequently,

it is feasible that at the low-SFR end more formation epochs are necessary than actually determined.

How would the subtraction of the stripped nuclei sample influence the SFR distributions of red and blue GCs/UCDs?
As mentioned above, the sample of stripped nuclei by Pfeffer et al. (2014) was not considered in the second analysis (Chap. 4) because it is not known which colors they would have. Still, the impact of this sample can be estimated for the second approach based on the results of the first analysis (Chap. 3): as can be seen in Fig. 3.6, if the stripped nuclei are excluded, the resulting SFR distributions (drawn in red) are still similar to the case where only UCD3 was excluded (drawn in green). The main difference between these two cases is that the peak SFRs are lower by at most 0.3 dex which corresponds to a factor of less than 2. However, only the highest SFRs in the SFR distribution are somewhat lower; toward lower SFRs, the two cases become indistinguishable.

I suspect the influence of the stripped nuclei sample on the SFR distributions of red and blue GCs/UCDs to be similar. For the following consideration, I presume that the most massive stripped nuclei are contaminating the red GC/UCD mass function since only that mass function contains equally massive objects. The less massive stripped nuclei could contaminate either the red or the blue GC/UCD mass function. If the stripped nuclei only account for red GCs/UCDs, their SFR distributions will be similar to the SFR distributions as determined from the red GC/UCDs sample without UCD3 (orange lines in Fig. 4.9) but with peak SFRs that are lower by a factor of 2 and with generally somewhat lower SFRs at the high-SFR end. The SFR distributions of the blue GCs/UCDs will stay unchanged in this case. If instead some of the stripped nuclei are contaminating the blue GC/UCD sample, some of their highest SFRs will decrease as well, depending on the actual mass of the objects. Since most of the stripped nuclei are still contaminating the red GC/UCD sample, their SFR distributions will probably be altered in a similar way as described before.

Considering all above findings, I can finally discuss two fundamental questions arising from this thesis:

What is the most probable distribution of SFRs during the formation of GCs/UCDs around NGC 1399?
The SFR distributions depend mostly on the index β of the underlying ECMF. The most probable value for the slope of the ECMF is $\beta \approx 2.0$ based on observational

evidence (e.g., Zhang & Fall 1999; Lada & Lada 2003; McCrady & Graham 2007; Chandar et al. 2011). This agrees nicely with the above finding that only values of $\beta < 2.3$ are allowed according to the constraints set by the age of the GCs/UCDs and the present-day total stellar mass of NGC 1399 on the total formation time of the whole GC/UCD system, $t_{\mathrm{SCFE,tot}}$, and the total stellar mass in the GC/UCD system, M_{tot}, as determined in the analysis.

In particular the high-SFR end depends crucially on the high-mass end of the considered GC/UCD sample and the question whether the objects there are compatible with being very massive SCs. It appears likely that UCD3 did not form in an SC formation process – and it is probably not the only one. Assuming that the sample of stripped nuclei as found by Pfeffer et al. (2014) represents a realistic distribution of masses that needs to be excluded from the overall sample of GCs/UCDs, then the most probable SFR distributions are the ones for $1.8 \lesssim \beta \lesssim 2.2$, drawn by red lines in Fig. 3.6. They are characterized by peak SFRs of around $\log_{10}(\mathrm{SFR}) \approx 2.5$, corresponding to roughly 300 $M_{\odot}\mathrm{yr}^{-1}$. The lowest required SFRs lie at $\log_{10}(\mathrm{SFR}) < 1.0$ which corresponds to SFRs of a few $M_{\odot}\mathrm{yr}^{-1}$. The number of SC formation epochs, $N_{\mathrm{SCFE,tot}}$, and thus the time to build up the entire GC/UCD system, $t_{\mathrm{SCFE,tot}}$, depends on t_4 as can be seen in Fig. 3.6 and in Table 3.2. Given that a very low t_4 is unlikely (Chap. 3.2), between a couple of hundreds up to around thousand SC formation epochs with a total duration of roughly 2 Gyr are necessary if the GCs/UCDs formed consecutively. However, if parts of the GC/UCD system formed simultaneously, a shorter timescale would be sufficient. During this time, a stellar mass of less than about 10^{11} $M_{\odot}$ was formed which would correspond to less than 20% (probably even less than 10%) of the present-day stellar mass of NGC 1399.

Applying the same considerations as before to the results of the separate analysis of red and blue GCs/UCDs, the interpretation stays essentially the same. Assuming again $1.8 \lesssim \beta \lesssim 2.2$, the distributions of SFRs are described by orange and blue lines in Fig. 4.9. However, the highest SFRs of the red GC/UCD sample need to be reduced by a factor of about 2 to account for objects in the stripped nuclei sample. The same might also apply to the highest SFRs of the blue GC/UCD sample since at least some of the lower-mass stripped nuclei could contaminate the blue GC/UCD sample. This leads to peak SFRs of $\log_{10}(\mathrm{SFR}) \approx 2.5$ and ≈ 2.0 for the red and blue GCs/UCDs which correspond to about 300 and 100 $M_{\odot}\mathrm{yr}^{-1}$, respectively. Again, assuming that a very low t_4 is not likely, each of the samples need several hundreds SC formation epochs corresponding to a formation timescale of 0.5 to 1 Gyr during which a total stellar mass of up to $5 \cdot 10^{10}$ $M_{\odot}$ for each sample is created. Interestingly, the produced stellar mass for red GCs/UCDs

is between 20% and 30% larger than for blue ones while the estimated formation duration is between 20% and 40% shorter. This might be taken as an indication for the downsizing effect which describes the circumstance that more massive stellar systems require shorter formation times (e.g., Cowie et al. 1996; Thomas et al. 1999; Juneau et al. 2005; Recchi et al. 2009). These findings are in agreement with the estimates for all GCs/UCDs but there is one additional thought: the red and blue GC/UCD sample could have formed consecutively but it is also conceivable that the two samples formed simultaneously but spatially separated. This would reduce the required time to build up the whole GC/UCD system to about 1 Gyr. Even shorter formation timescales are possible if the GCs/UCDs within each sample formed at the same time at different places.

What can be said about the formation of NGC 1399 and its GC system?
The essential findings of this thesis are the required SFRs and the number of SC formation epochs: Figs. 3.6 and 4.9 show clearly how many formation epochs at which SFRs are needed. However, there is no information about the order in which all these SFRs occurred. Thus, the star formation history (SFH) – meaning the evolution of the SFR with time – cannot be deduced from the outcome of the analysis. Consequently, it is not known which of the red and blue GC/UCD samples formed first, if they formed consecutively, or whether they formed simultaneously. Depending on the chronology of sample formation and bearing in mind the above considerations of the formation timescale, the whole process lasted for roughly 2 Gyr or about 1 Gyr. The ages of the GCs/UCDs themselves do not allow to draw a definitive conclusion about exactly when and the order in which they formed. It is only clear that most of them have ages above 8 Gyr but the exact value is very difficult to determine with certainty.

Based on Chap. 3 and in particular on the determined peak SFRs, it is safe to say that NGC 1399 might have originated from an intense starburst similar to those observed in massive sub-millimeter galaxies in the distant Universe. During that starburst, in particular the most massive GCs/UCDs were formed along with many lower mass GCs within a few Gyr. The dissolution and tidal disruption of a part of the GCs/UCDs probably contributed to the assembly of the stellar body and the halo of NGC 1399, while a part of the GCs/UCDs was able to survive and can be observed today. The results of Chap. 4 indicate that because of their higher masses, red GCs/UCDs require higher SFRs than blue GCs/UCDs. However, this finding alone does not help to distinguish between the two classical formation scenarios by Forbes et al. (1997) and Côté et al. (1998). Forbes et al. (1997) suggested

that the majority of GCs have formed in situ in two distinct phases out of gas with different metallicities, causing the bimodal GC metallicity distribution. Instead, Côté et al. (1998) argued that metal-rich GCs represent the galaxy's intrinsic GC system, while the metal-poor GCs are captured from other galaxies through mergers or tidal stripping. As discussed in Chap. 4.9.3, the outcome is in agreement with both formation scenarios. However, red GCs and the stellar spheroid of NGC 1399 share many similarities, while the properties of blue GCs, in particular their distribution in phase space, are more chaotic and do not resemble the spheroid of NGC 1399 as has been found by various different studies (see Chap. 4.9.3). Thus, there is some evidence that NGC 1399 acquired its blue GCs through stripping or accretion as suggested by Côté et al. (1998). In conclusion, it seems likely that the red GCs/UCDs formed together with the spheroid of NGC 1399 in a relatively short, intense starburst early on, while the blue GCs/UCDs require less high SFRs and could have formed independent of NGC 1399, probably tracing the halo build-up by accretion and stripping of infalling galaxies. Essentially the same formation scenario has been suggested for the central giant elliptical M87 in the Virgo galaxy cluster by Brodie et al. (2011).

5.2 Strenghts of the presented approach

Usefulness of the presented method to determine the required SFRs
It appears that the presented method to determine the distribution of required SFRs based on the mass function of GC around a galaxy leads to reasonable results. Moreover, since it was applied twice – once to the whole sample, once to the color-separated samples – this allows to confirm the reliability and the self-consistency of the method. Even though the application of this method can only determine the necessary SFRs but not their evolution with time – given that GCs are used as tracers whose old ages cannot be determined exactly – it still provides valuable insights into the conditions at the time of GC formation in a particularly dense environment of a central galaxy in a galaxy cluster. Thus, it is a helpful approach – along with other studies of the GC/UCD properties – to obtain a full picture of GC and galaxy formation.

Advantage of using multiple colors
Another important outcome of this thesis is the reliability of the method used to separate GCs/UCDs based on their color into a red and a blue sample as has been done in Chap. 4.2.2 and Chap. 4.3. Typically, the distinction is based on one

color, meaning the difference between the magnitudes in two bands (e.g., Bassino et al. 2006a; Masters et al. 2010; Schuberth et al. 2010; Liu et al. 2011) because often only these bands are available. Here, I used the Fornax Deep Survey (FDS, Chap. 4.1.2) in which the central region of the Fornax galaxy cluster was observed in the u, g, r, and i bands. It therefore appeared straightforward to use all available bands to calculate all possible colors, namely $g-r$, $g-i$, $r-i$, $u-g$, $u-r$, and $u-i$, and investigate their correlations.

For this task, I took the spectroscopic sample of GCs/UCDs with more than 1000 objects and matched it with the photometry from the FDS. By doing this, luminosities in the g, r, and i bands were obtained for the vast majority of the objects while u magnitudes were only available for about half of the objects. When examining the color correlations, I used interactive three-dimensional plots to be able to perceive the full content of the data. Two findings were striking: first, when using colors from only three band, the resulting distribution of data points is a flat two-dimensional plane within the three-dimensional volume. Second, the 3D plot with the colors $u-g$, $u-r$, and $u-i$ on the axes resulted in the narrowest distribution of data points with a very low spread resembling a cigar-like shape (see Fig. 4.3). These two findings were very fortunate: the complementary plot of the latter would be one with the colors $g-r$, $g-i$, and $r-i$ on the axes – since only three bands are involved, the distribution of data points is two-dimensional and the plot contains almost all objects as the u band is not included. Upon further examination, this plot yielded additional information: when rotating the plot back and forth, it appeared like the distribution of data points could be described by two almost round clusters of data points that were overlapping a considerable amount. However, this is not very well visible in the two-dimensional representation of the 3D plot in Fig. 4.2. After rotating the plane such that it lies in two dimensions (or equally, determine two axes in the plane that are perpendicular), it becomes more apparent. After the application of a two component Gaussian Mixture Model (GMM) to the rotated data, the contours show clearly that the distribution of colors can be described by two Gaussians (Fig. 4.4) and confirms quantitatively the bimodal color distribution of the bright – and therefore massive – GCs/UCDs. Thus, if a carefully selected sample of GCs/UCDs is available so that the level of contamination with fore- or background objects can be considered very low, the 3D plot $g-r$ vs. $g-i$ vs. $r-i$ is particularly suitable to quantify a color bimodality.

To obtain a robust sample of lower mass objects for the FDS photometry, I explicitly assumed that they have similar colors as compared to the more massive GCs/UCDs. The objects were selected by testing for each object from the FDS

whether its colors $g - r$, $g - i$, and $r - i$ are within the outermost contour in Fig. 4.4. If an u magnitude was available, it was also tested whether its colors $u - g$, $u - r$, and $u - i$ lie within the volume of the cigar-like distribution of data points in Fig. 4.3. Apart from that, additional constraints were applied regarding the spatial location, the value of the FWHM or the stellarity index. It turned out that this photometrically selected sample of GC-like objects exhibits a bimodal color distribution in a very similar way to the spectroscopic sample which was confirmed by the application of a two component GMM to the photometric sample – even the location of the peaks was very similar (Fig. 4.5). It cannot be excluded that there are contaminants in this photometric selection but the similarity of the Gaussian contours (Fig. 4.5) shows that the presented approach of distinguishing objects based on multiple colors appears to yield robust results and relatively clean samples.

5.3 Possible improvements of the presented method

Even though the introduced methods – the determination of necessary SFRs as well as the division of all GCs/UCDs into a red and a blue sample – gives very reasonable results there is – as usual – room for improvements.

Further constraints on the high-mass end of the GC/UCD mass function
The high-mass end of the GC/UCD mass function can be regarded as robust since all objects have been observed spectroscopically from which their membership was confirmed. Still, some bright GCs/UCDs might have been missed in the spectroscopic surveys since the contamination by foreground stars is large. For this analysis, only objects that formed in an SC formation process are of interest and in particular the high-mass end is subject to contamination by stripped nuclei. Even though an expected number of stripped nuclei was taken into account when analyzing the whole GC/UCD sample (Chap. 3), this sample was not considered as soon as all GCs/UCD were divided into a red and a blue sample because the color distribution of the stripped nuclei is not known. Indeed, the mass function of the red GCs/UCDs looks suspicious because of a bump at the high-mass end (red lines in Fig. 4.6, particularly visible in top left panel).

One possibility to deal with this issue would be to estimate the colors of the simulated stripped nuclei from Pfeffer et al. (2014), divide them into red and blue objects and subtract them from the corresponding sample. Apart from this statistical approach, another possibility might allow a more accurate treatment of

the high-mass end in near future: while observations in the past were often focused mainly on the detections of GCs/UCDs, nowadays, more and more studies concentrate on the investigation and characterization of individual objects. For instance, Richtler et al. (2005) and Voggel et al. (2016) surveyed UCDs that exhibit extended surface brightness profiles or even tidal features while Wittmann et al. (2016) found asymmetric or elongated UCDs. From this alone an unambiguous distinction between a galaxian and an SC origin is not possible. A better discrimination would be the detection of a super-massive black hole or an extended SFH which would point toward a galaxy as the progenitor. Thus, even though it still remains difficult to draw definitive conclusions about the origin it can be expected that upcoming studies will gain deeper insights into the nature of individual UCDs.

Further constraints on the low-mass end of the GC/UCD mass function

As compared to the high-mass end, the low-mass end appears to be even more likely to be subject to contamination: none of the GCs there have been observed individually but they have purely been selected based on the criteria color, luminosity, FWHM, and stellarity index in the different bands. Thus, it cannot be excluded that some of them are either fore- or background objects that happen to match the constraints. However, it can be suspected that number of contaminants is relatively low because their distribution in color space (Fig. 4.5) can be described by almost the same two Gaussians that are characterizing the color distribution of the spectroscopic sample. Whether this is indeed the case could have been shown by the following statistical analysis: to estimate the level of contamination, the same selection criteria have to be applied to a region of sky that has the same spatial size but preferably far away from any larger galaxy. This way the number of fore- or background objects can be estimated statistically since only a small number of GCs is expected in such an environment. Still, Fig. 4.5 might hint at the fact that in particular red objects are contaminating the photometric sample: first, the peaks of the two Gaussians describing the red objects of the spectroscopic and the photometric sample are offset to each other. Second, red objects of the photometric sample are dispersed more widely in color space than red objects of the spectroscopic sample. In order to better separate fore- and background objects from GCs, photometric observations in additional bands would be helpful. Since the visual and UV wavelength range are covered, complementary infrared magnitudes, for instance in the K band, would be ideal. This way, GCs can be accurately separated from other objects in the uiK plane as has been shown by

Muñoz et al. (2014) in the Next Generation Virgo Cluster Survey in the infrared. Fortunately, the Next Generation Fornax Cluster Survey will provide observations in the K band. Moreover, a visual inspection of the GC candidates would be useful to reduce the number of contaminants.

Influence of the lower mass limit for an SC, $M_{\rm min}$

In Chap. 2, the lower mass limit for an SC was assumed to be $M_{\rm min} = 5\ M_\odot$. The question is whether such a low value is justified since the formation of very high-mass SCs is considered. Thus, I examined how larger values for $M_{\rm min}$ would change the determined SFRs. $M_{\rm min}$ is a fundamental parameter since it is the lower integration limit of the ECMF (Eqs. (2.15)–(2.17)) and thus occurs in almost all equations implicitly, in particular in the ones regarding the formation of SCs. A change in $M_{\rm min}$ alters therefore many other quantities.

First, and most importantly, the total mass of an SC population decreases if $M_{\rm min}$ is increased (Eq. (2.17)). Second, this influences through Eq. (2.18) the SFR–$M_{\rm ecl,max}$ relation which has to be reevaluated by fitting Eq. (2.25) to the data points in Fig. 2.2. The fitting parameter δt, the length of one SC formation epoch, changes such that it becomes smaller, the larger the chosen value of $M_{\rm min}$. For instance, if $M_{\rm min} = 1\,000\ M_\odot$ is assumed, δt decreases from 2.8 Myr to 1 Myr. The change is stronger for larger β. Note that these values are lower than the canonical value of 10 Myr. Third, the influence on the SFRs: interestingly, the SFRs do not change much. The reason is that predominantly the low-mass end of the SFR–$M_{\rm ecl,max}$ relation in Fig. 2.2 is affected since only the lower mass limit is changed. At the high-mass end and thus at the high-SFR regime, the fitted lines are only mildly influenced as the data points are fixed. In relative terms, the impact is stronger at low-mass end because the fitting lines in Fig. 2.2 are shifted upward due to the larger $M_{\rm min}$. However, the SFRs themselves are very small there so that the change is negligible in absolute terms. Thus, a change in $M_{\rm min}$ mostly influences the total mass of an SC population, $M_{\rm tot}$, and thus the mass of the galaxy, as well as the length of an SC formation epoch, δt, while the SFRs stay almost the same. However, there is no necessity to change the lower mass limit, $M_{\rm min}$, when analyzing the GCs/UCDs around NGC 1399 since the resulting SFRs, the formation timescale and the produced mass are reasonable.

Overall, it can be concluded that even without the additional improvements at the high- and low-mass end of the GC/UCD mass function, the analysis is self-consistent and leads to solid results.

5.4 Outlook

As the presented method determines the required SFRs reliably, it appears straightforward to apply it to other GC/UCD samples:

Application to GCs/UCDs of other galaxies
Because of the statistical nature of the method, rich GC systems around other central galaxies of galaxy clusters would be ideal targets to investigate their required distributions of SFRs. M87, the central cluster galaxy in the Virgo galaxy cluster, would be particularly suitable: it is relatively close with a distance of about 16.5 Mpc which is why it has been observed in many surveys to allow data on its GC/UCD systems to be readily available. It would be interesting to have the direct comparison of the required SFRs between the central galaxies of Fornax and Virgo since Virgo is considerably larger, has much more member galaxies than Fornax, and is also more massive. If the peak SFRs scale with the size or the mass of the system, it would appear reasonable to assume that GCs/UCDs around Virgo require generally higher SFRs.

Apart from Virgo, the GC/UCD systems of other central galaxies in galaxy clusters like Centaurus, Coma, Hydra, Perseus and Antlia could be examined. The brightest – and thus, the most massive – GC/UCD have already been observed but data on the fainter and thus less-massive GCs might not be available yet. The fact that these galaxy clusters are further away than Virgo or Fornax places higher requirements on the observations since either longer integration times or more sensitive instruments are needed. This is a crucial constraint since the acquisition of observational data that allows to compile a complete and homogeneous GC/UCD sample is essential to obtain meaningful results. The benefit of this would be the opportunity to study the correlation between the required SFR distributions and environmental properties, such as richness of the GC/UCD system, or the mass of the host galaxy. Further insights could be gained if the GCs/UCDs could be divided into a red and a blue sample and analyzed separately.

Not only central galaxies of galaxy clusters exhibit numerous GCs. This applies also for less massive galaxies in the outskirts of galaxy clusters or even galaxies located in groups. For instance, if the method is applied to the GC systems of two galaxies of similar mass and type but with one located in a group and the other one in a galaxy cluster, the required SFRs as a function of environment could be studied. It would be interesting to find out whether, and to which extent, the GCs around a galaxy “know” about the environment of their host galaxy. The required SFRs could possibly reflect this environmental dependence.

Going to lower galaxy masses and focusing on group environments, particularly interesting target galaxies would of course be the MW or M31. The MW has a mass of about 10^{11} $M_{\odot}$ and roughly 150 GCs, while M31 has a mass of about $1.5 \cdot 10^{11}$ $M_{\odot}$ and roughly 480 GCs. Their unique advantage is that both GC systems are known in great detail since a significant fraction of their GCs have been observed individually. For a large number of GCs around the MW, structural and dynamical parameters, as well as luminosities, colors, and metallicities are known (Harris 1996). A similar type of catalog exists also for M31 (Galleti et al. 2004). The difference in the required SFRs for these two galaxies could then be related to the fact that M31 is probably a few times more massive and has three times as many GCs.

It would be conceivable to apply this method to even smaller and less massive galaxies with lower number of associated GCs. The galactic low-mass end is dominated by dwarf galaxies with masses of 10^{8} $M_{\odot}$ and above, which seldom have their own small GC system. One example is the Fornax dwarf spheroidal galaxy which hosts five GCs. Below, I determine the required SFRs for these GCs and discuss the caveats when applying the method to such a poor GC system.

Overall, this approach could be targeted at GC systems around different galaxies in different environments. It appears natural to assume that smaller and less-massive galaxies host less rich GC systems that contain less massive objects so that generally fewer and lower SFRs would be expected during their formation. However, it would be helpful to describe this effect not only qualitatively but also quantitatively, in particular by tracking how the shape of the SFR distributions change in comparison to the ones in Figs. 3.6 or 4.9 for the GCs/UCDs around NGC 1399. I expect the SFR distributions to become shallower in particular at the high-SFR end for less massive galaxies and thus less rich GC systems. However, while it seems natural that fewer and lower SFRs would be necessary, it is not obvious how the number of formation epochs would change: one interesting finding from the separate analysis of red and blue GCs/UCDs was that red GCs/UCDs around the central cluster galaxy required less formation epochs and therefore a shorter formation timescale than blue GCs/UCDs even though that the red GCs/UCDs are more massive and need higher SFRs. It would thus be feasible that less massive GC systems require more formation epochs and thus longer formation timescales. Particular attention could also be paid to the environmental dependence by comparing how the SFRs differ between a central cluster galaxy, a galaxy in the outskirts of a galaxy cluster, or a field galaxy.

Application to the Fornax dwarf spheroidal galaxy

The Fornax dwarf spheroidal galaxy is a very interesting case since the dwarf has a mass of only $1.6 \cdot 10^8\ M_\odot$ (Łokas 2009) but hosts in total five GCs. These five GCs have masses between $3.7 \cdot 10^4\ M_\odot$ and $3.6 \cdot 10^5\ M_\odot$ (Mackey & Gilmore 2003) which sum up to a total mass of $8.9 \cdot 10^5\ M_\odot$. I applied the same method to these five GCs but did not include the correction for mass loss and used their present-day masses instead. Thus, the masses of the generated SCs and all inferred total stellar masses have to be considered as present-day masses as well. Consequently, it has to be taken into account that these masses are only lower limits since all SCs must have been formed with higher initial masses. The reason for this approach is that below I will compare the masses of the generated SC with the mass of stars in the dwarf galaxy. The latter are present-day masses for which a correction for mass loss is not obvious. Generally, the initial masses of the GCs and the generated SCs are expected to be higher by about 50% since stellar evolution reduces the initial mass by about one third. The dynamical mass loss due to the orbit of the objects in the gravitational potential is likely to be negligible since the mass of the dwarf galaxy is low. However, the SFR estimates were calculated based on GC masses which were corrected for stellar evolution.

I calculated the required SFRs for these GCs for $1.7 \leq \beta \leq 2.5$: the highest SFRs lie between almost 3 $M_\odot \mathrm{yr}^{-1}$ and 9 $M_\odot \mathrm{yr}^{-1}$, with higher SFRs for larger β. For $\beta \leq 1.8$, three formation epochs are needed, for $1.9 \leq \beta \leq 2.1$ two, and $\beta \geq 2.2$ requires only one formation epoch. During this formation time a total mass of $2.7 \cdot 10^6\ M_\odot$, $8.1 \cdot 10^6\ M_\odot$, and $4.2 \cdot 10^8\ M_\odot$ is created in the form of SCs with masses down to $M_{\mathrm{min}} = 5\ M_\odot$ for a β of 1.7, 2.0, and 2.5. Generally, it is believed that lower-mass SCs dissolve and contribute their stars to either the host galaxy or the surrounding halo. Given the total mass of the five GCs of $8.9 \cdot 10^5\ M_\odot$, this implies for $\beta = 2.0$ that only about 10% of the stellar mass is still bound in GCs while the remaining 90% of the stellar mass in SCs must have been dissolved.

However, the situation of the GCs around Fornax is slightly more complicated: the second least massive GC, F4, has a metallicity of [Fe/H] = −1.4 and is therefore significantly more metal-rich than the other four GCs which have metallicities in the range −2.5 < [Fe/H] < −2 (Letarte et al. 2006; Larsen et al. 2012a,b). Thus, F4 cannot have formed out of the same giant molecular cloud together with the other four GCs. Also, it is not clear whether the four metal-poor GCs could have formed together since they do not have exactly the same metallicities. Assuming that the latter is possible, I applied the method to only the four metal-poor GCs.

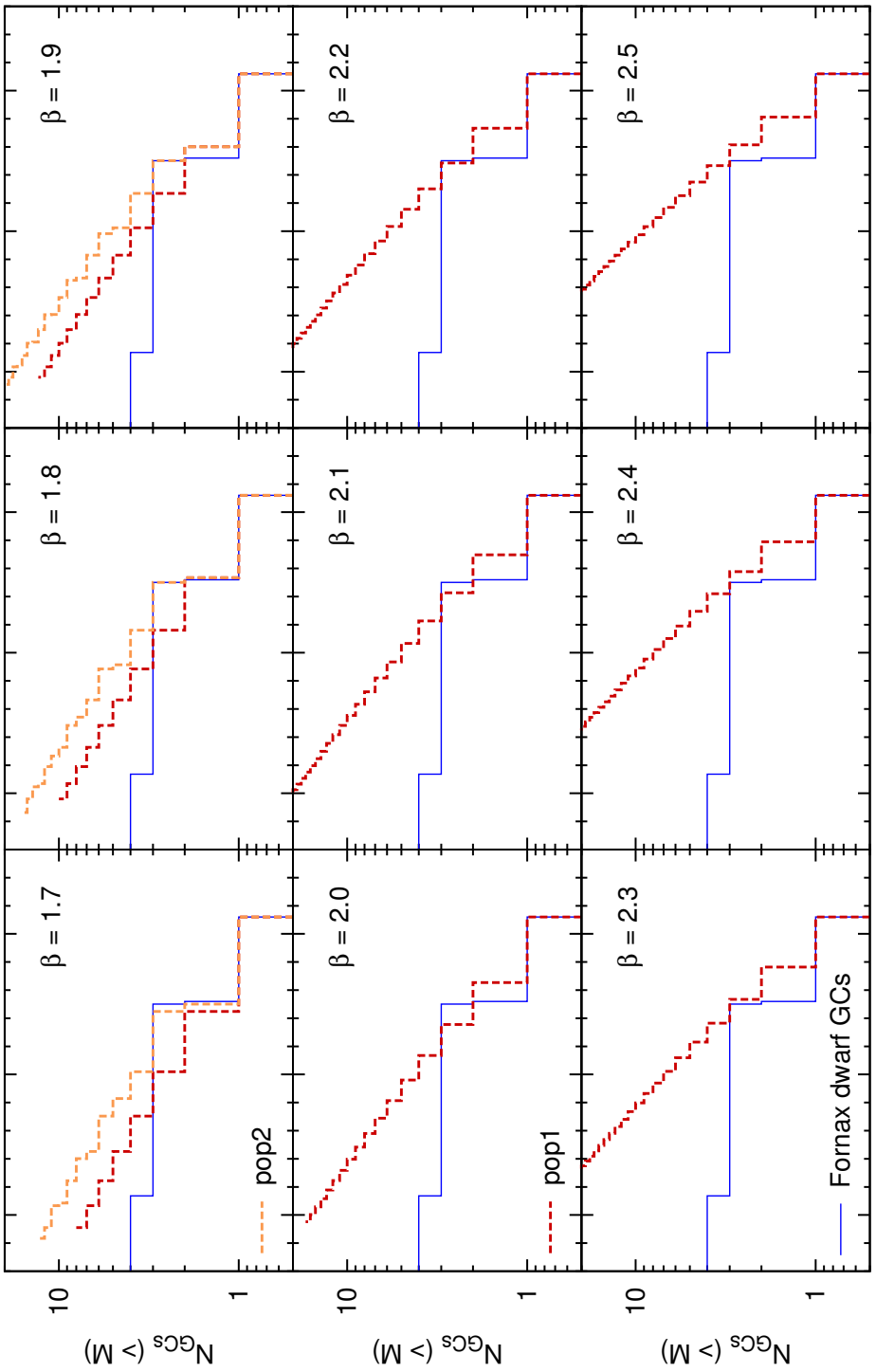

Figure 5.1: The cumulative present-day mass function of the four metal-poor GCs around the Fornax dwarf spheroidal galaxy (blue continuous lines) is shown together with the replicated mass functions (red and orange dashed lines for the first and second SC population, respectively) as a function of β.

Table 5.1: The total stellar mass, $M_{\rm tot}$, and the stellar mass of the first and second SC population, $M_{\rm pop1}$ and $M_{\rm pop2}$, generated to match the mass distribution of the four metal-poor GCs around the Fornax dwarf as a function of β.

β	$M_{\rm tot}$ [$10^6\ M_\odot$]	$M_{\rm pop1}$ [$10^6\ M_\odot$]	$M_{\rm pop2}$ [$10^6\ M_\odot$]
1.7	2.04	1.37	0.67
1.8	3.05	2.06	0.99
1.9	4.95	3.36	1.59
2.0	6.05	6.05	-
2.1	12.09	12.09	-
2.2	26.61	26.61	-
2.3	63.40	63.40	-
2.4	160.52	160.52	-
2.5	424.73	424.73	-

While the SFRs stay the same, the other quantities change partly: now, the cases $\beta \leq 1.9$, need two formation epochs, while $\beta \geq 2.0$ requires only one formation epoch. This can be viewed in Fig. 5.1 where the mass distribution of the four metal-poor GCs is drawn with a blue continuous line while the mass distribution of the first and second generated SC population are drawn with red and orange dashed lines. Also, it becomes apparent from the figure that toward the low-mass end more SCs are created than actually observed. As compared to the previous case, the created total stellar mass changes for $\beta \leq 2.1$. The new total masses are somewhat lower as can be seen in Table 5.1. Taking again the case $\beta = 2.0$ where $6 \cdot 10^6\ M_\odot$ are formed and comparing it to the total present-day mass of the four metal-poor GCs of $7.6 \cdot 10^5\ M_\odot$, implies that about 10% of the created stellar mass is still bound in GCs while the remaining 90% of the mass formed in SCs, about $5.2 \cdot 10^6\ M_\odot$, must have been dispersed.

Here, the question arises where the metal-poor stars are that constituted the lower mass SCs which formed together with the GCs. A simple calculation might be helpful, assuming that these stars are now part of the dwarf galaxy's field population: Coleman & de Jong (2008) determined the total stellar mass that formed in Fornax to be $6.1 \cdot 10^7\ M_\odot$ from which roughly $4 \cdot 10^7\ M_\odot$ should be present in Fornax today, accounting for the fact that one third of the initial mass was lost due to stellar evolution. Larsen et al. (2012b) estimated that around 5% of the stars in the dwarf have metallicities of [Fe/H] < -2 which gives a total stellar mass of

$2 \cdot 10^6\ M_\odot$ in metal-poor stars. However, according to the above estimate, metal-poor stars with a mass of roughly $7 \cdot 10^6\ M_\odot$ should be enclosed by Fornax for a realistic β of 2.0. Apparently, this estimate exceeds clearly the actually available mass in metal-poor stars.

One possible way to overcome the issue regarding the mass budget is to change the lower mass limit for SCs, $M_{\rm min}$, as described in Chap. 5.3. For instance, changing $M_{\rm min}$ to 1 000 $M_\odot$, but keeping all other assumptions as in the previous example leads to a total stellar mass of $3.3 \cdot 10^6\ M_\odot$ for $\beta = 2.0$ meaning only about half of the mass as compared to the case with $M_{\rm min} = 5\ M_\odot$. Subtracting the stellar mass of the four metal-poor GCs leaves a mass of $2.5 \cdot 10^6\ M_\odot$ in metal-poor stars which is much closer to the estimate of metal-poor stars in Fornax. Thus, for a even larger $M_{\rm min}$ the two estimates could be brought into accordance but this presumes that the four metal-poor GCs did not lose any stars in the course of time which is rather unlikely. In fact, Larsen et al. (2012b) suggested that the metal-poor stars in Fornax originally belonged to the four metal-poor GCs and estimated from this that these GCs might have been four to five times more massive initially. However, using a series of N-body simulations, Khalaj & Baumgardt (2016) pointed out that under certain circumstances the initial masses of these GCs might be even higher if allowing for the loss of stars into the intergalactic medium.

Either way it is evident that the formation conditions of the GCs around the Fornax dwarf galaxy cannot be easily deduced from the GCs alone even if stellar properties of Fornax are taken into account. It might even be that the GCs did not have formed together with a larger population of now disrupted SCs with an initial power-law mass distribution as speculated by Larsen et al. (2012b). In particular the existence of F4, the more metal-rich GC, gives rise to such an interpretation unless it is the only surviving object of a larger population. Nevertheless, applying the presented method to the GCs around Fornax highlights that small GC systems place on one hand, much stricter constraints on their formation conditions but leave on the other hand, room for interpretations since observational data is always limited.

Bibliography

Adamo, A., Östlin, G., & Zackrisson, E. 2011, MNRAS, 417, 1904

Alaghband-Zadeh, S., Chapman, S. C., Swinbank, A. M., et al. 2012, MNRAS, 424, 2232

Alexander, P. E. R. & Gieles, M. 2012, MNRAS, 422, 3415

Alexander, P. E. R., Gieles, M., Lamers, H. J. G. L. M., & Baumgardt, H. 2014, MNRAS, 442, 1265

Andrade-Santos, F., Nulsen, P. E. J., Kraft, R. P., et al. 2013, ApJ, 766, 107

Ashman, K. M. & Zepf, S. E. 1992, ApJ, 384, 50

Asplund, M., Grevesse, N., Sauval, A. J., & Scott, P. 2009, ARA&A, 47, 481

Bassino, L. P., Faifer, F. R., Forte, J. C., et al. 2006a, A&A, 451, 789

Bassino, L. P., Richtler, T., & Dirsch, B. 2006b, MNRAS, 367, 156

Bastian, N. 2008, MNRAS, 390, 759

Bastian, N. 2016, in EAS Publications Series, Vol. 80, EAS Publications Series, ed. E. Moraux, Y. Lebreton, & C. Charbonnel, 5–37

Bastian, N., Adamo, A., Gieles, M., et al. 2012a, MNRAS, 419, 2606

Bastian, N., Konstantopoulos, I. S., Trancho, G., et al. 2012b, A&A, 541, A25

Bastian, N., Saglia, R. P., Goudfrooij, P., et al. 2006, A&A, 448, 881

Baumgardt, H. & Makino, J. 2003, MNRAS, 340, 227

Behroozi, P. S., Wechsler, R. H., & Conroy, C. 2013, ApJ, 770, 57

Bekki, K., Couch, W. J., & Drinkwater, M. J. 2001, ApJ, 552, L105

Bekki, K., Couch, W. J., Drinkwater, M. J., & Shioya, Y. 2003a, MNRAS, 344, 399

Bekki, K., Forbes, D. A., Beasley, M. A., & Couch, W. J. 2003b, MNRAS, 344, 1334

Bekki, K. & Mackey, A. D. 2009, MNRAS, 394, 124

Bergond, G., Athanassoula, E., Leon, S., et al. 2007, A&A, 464, L21

Béthermin, M., Wang, L., Doré, O., et al. 2013, A&A, 557, A66

Bik, A., Lamers, H. J. G. L. M., Bastian, N., Panagia, N., & Romaniello, M. 2003, A&A, 397, 473

Billett, O. H., Hunter, D. A., & Elmegreen, B. G. 2002, AJ, 123, 1454

Blakeslee, J. P., Cho, H., Peng, E. W., et al. 2012, ApJ, 746, 88

Blakeslee, J. P., Jordán, A., Mei, S., et al. 2009, ApJ, 694, 556

Bonatto, C. & Bica, E. 2012, MNRAS, 2898

Bonnell, I. A., Dobbs, C. L., Robitaille, T. P., & Pringle, J. E. 2006, MNRAS, 365, 37

Bridges, T. J., Hanes, D. A., & Harris, W. E. 1991, AJ, 101, 469

Brockamp, M., Küpper, A. H. W., Thies, I., Baumgardt, H., & Kroupa, P. 2014, MNRAS, 441, 150

Brodie, J. P., Romanowsky, A. J., Strader, J., & Forbes, D. A. 2011, AJ, 142, 199

Brown, J. H., Burkert, A., & Truran, J. W. 1995, ApJ, 440, 666

Brüns, R. C. & Kroupa, P. 2012, A&A, 547, A65

Brüns, R. C., Kroupa, P., Fellhauer, M., Metz, M., & Assmann, P. 2011, A&A, 529, A138

Bruzual, G. & Charlot, S. 2003, MNRAS, 344, 1000

Carico, D. P., Sanders, D. B., Soifer, B. T., Matthews, K., & Neugebauer, G. 1990, AJ, 100, 70

Casey, C. M., Narayanan, D., & Cooray, A. 2014, Phys. Rep., 541, 45

Caso, J. P., Bassino, L. P., Richtler, T., Smith Castelli, A. V., & Faifer, F. R. 2013, MNRAS, 430, 1088

Chabrier, G. 2003, PASP, 115, 763

Chandar, R., Whitmore, B. C., Calzetti, D., et al. 2011, ApJ, 727, 88

Chandar, R., Whitmore, B. C., Kim, H., et al. 2010, ApJ, 719, 966

Chiboucas, K., Tully, R. B., Marzke, R. O., et al. 2011, ApJ, 737, 86

Chilingarian, I. V., Cayatte, V., & Bergond, G. 2008, MNRAS, 390, 906

Chilingarian, I. V., Mieske, S., Hilker, M., & Infante, L. 2011, MNRAS, 412, 1627

Chomiuk, L. & Povich, M. S. 2011, AJ, 142, 197

Chung, C., Yoon, S.-J., Lee, S.-Y., & Lee, Y.-W. 2016, ApJ, 818, 201

Citro, A., Pozzetti, L., Moresco, M., & Cimatti, A. 2016, A&A, 592, A19

Coleman, M. G. & de Jong, J. T. A. 2008, ApJ, 685, 933

Condon, J. J., Huang, Z.-P., Yin, Q. F., & Thuan, T. X. 1991, ApJ, 378, 65

Côté, P., Marzke, R. O., & West, M. J. 1998, ApJ, 501, 554

Cowie, L. L., Songaila, A., Hu, E. M., & Cohen, J. G. 1996, AJ, 112, 839

da Cunha, E., Walter, F., Smail, I. R., et al. 2015, ApJ, 806, 110

Da Rocha, C., Mieske, S., Georgiev, I. Y., et al. 2011, A&A, 525, A86

Dabringhausen, J., Fellhauer, M., & Kroupa, P. 2010, MNRAS, 403, 1054

Dabringhausen, J., Kroupa, P., & Baumgardt, H. 2009, MNRAS, 394, 1529

Dabringhausen, J., Kroupa, P., Pflamm-Altenburg, J., & Mieske, S. 2012, ApJ, 747, 72

D'Abrusco, R., Cantiello, M., Paolillo, M., et al. 2016, ApJ, 819, L31

Dawe, J. A. & Dickens, R. J. 1976, Nature, 263, 395

de Grijs, R. & Anders, P. 2006, MNRAS, 366, 295

de Grijs, R., Anders, P., Bastian, N., et al. 2003, MNRAS, 343, 1285

de Grijs, R. & Goodwin, S. P. 2008, MNRAS, 383, 1000

de Grijs, R., O'Connell, R. W., & Gallagher, III, J. S. 2001, AJ, 121, 768

Dirsch, B., Richtler, T., Geisler, D., et al. 2003, AJ, 125, 1908

Dirsch, B., Richtler, T., Geisler, D., et al. 2004, AJ, 127, 2114

Dowell, J. D., Buckalew, B. A., & Tan, J. C. 2008, AJ, 135, 823

Drinkwater, M. J., Gregg, M. D., Hilker, M., et al. 2003, Nature, 423, 519

Drinkwater, M. J., Jones, J. B., Gregg, M. D., & Phillipps, S. 2000, PASA, 17, 227

Eggen, O. J., Lynden-Bell, D., & Sandage, A. R. 1962, ApJ, 136, 748

Egusa, F., Kohno, K., Sofue, Y., Nakanishi, H., & Komugi, S. 2009, ApJ, 697, 1870

Egusa, F., Sofue, Y., & Nakanishi, H. 2004, PASJ, 56, L45

Elmegreen, B. G. 1999, Ap&SS, 269, 469

Elmegreen, B. G. 2010, ApJ, 712, L184

Evstigneeva, E. A., Drinkwater, M. J., Jurek, R., et al. 2007a, MNRAS, 378, 1036

Evstigneeva, E. A., Drinkwater, M. J., Peng, C. Y., et al. 2008, AJ, 136, 461

Evstigneeva, E. A., Gregg, M. D., Drinkwater, M. J., & Hilker, M. 2007b, AJ, 133, 1722

Faifer, F. R., Escudero, C. G., Scalia, M. C., et al. 2017, A&A, 599, L8

Fall, S. M. 2004, in Astronomical Society of the Pacific Conference Series, Vol. 322, The Formation and Evolution of Massive Young Star Clusters, ed. H. J. G. L. M. Lamers, L. J. Smith, & A. Nota, 399

Fall, S. M. & Rees, M. J. 1977, MNRAS, 181, 37P

Fall, S. M. & Rees, M. J. 1985, ApJ, 298, 18

Fall, S. M. & Zhang, Q. 2001, ApJ, 561, 751

Famaey, B. & McGaugh, S. S. 2012, Living Reviews in Relativity, 15

Farrah, D., Serjeant, S., Efstathiou, A., Rowan-Robinson, M., & Verma, A. 2002, MNRAS, 335, 1163

Fellhauer, M. & Kroupa, P. 2002, MNRAS, 330, 642

Fellhauer, M. & Kroupa, P. 2005, MNRAS, 359, 223

Ferrarese, L., Mould, J. R., Kennicutt, Jr., R. C., et al. 2000, ApJ, 529, 745

Firth, P., Drinkwater, M. J., Evstigneeva, E. A., et al. 2007, MNRAS, 382, 1342

Firth, P., Evstigneeva, E. A., & Drinkwater, M. J. 2009, MNRAS, 394, 1801

Forbes, D. A., Beasley, M. A., Brodie, J. P., & Kissler-Patig, M. 2001, ApJ, 563, L143

Forbes, D. A., Brodie, J. P., & Grillmair, C. J. 1997, AJ, 113, 1652

Forbes, D. A., Grillmair, C. J., Williger, G. M., Elson, R. A. W., & Brodie, J. P. 1998, MNRAS, 293, 325

Francis, K. J., Drinkwater, M. J., Chilingarian, I. V., Bolt, A. M., & Firth, P. 2012, MNRAS, 425, 325

Frank, M. J., Hilker, M., Mieske, S., et al. 2011, MNRAS, 414, L70

Fukui, Y., Mizuno, N., Yamaguchi, R., et al. 1999, PASJ, 51, 745

Galleti, S., Federici, L., Bellazzini, M., Fusi Pecci, F., & Macrina, S. 2004, A&A, 416, 917

Gebhardt, K., Lauer, T. R., Pinkney, J., et al. 2007, ApJ, 671, 1321

Genzel, R. & Cesarsky, C. J. 2000, ARA&A, 38, 761

Genzel, R., Tacconi, L. J., Rigopoulou, D., Lutz, D., & Tecza, M. 2001, ApJ, 563, 527

Gieles, M., Larsen, S. S., Bastian, N., & Stein, I. T. 2006a, A&A, 450, 129

Gieles, M., Larsen, S. S., Scheepmaker, R. A., et al. 2006b, A&A, 446, L9

Glazebrook, K., Schreiber, C., Labbé, I., et al. 2017, Nature, 544, 71

Goerdt, T., Moore, B., Kazantzidis, S., et al. 2008, MNRAS, 385, 2136

Gott, III, J. R. 1975, ApJ, 201, 296

Gregg, M. D., Drinkwater, M. J., Evstigneeva, E., et al. 2009, AJ, 137, 498

Grevesse, N. & Sauval, A. J. 1998, Space Sci. Rev., 85, 161

Grillmair, C. J., Freeman, K. C., Bicknell, G. V., et al. 1994, ApJ, 422, L9

Gunawardhana, M. L. P., Hopkins, A. M., Sharp, R. G., et al. 2011, MNRAS, 415, 1647

Haas, M. R. & Anders, P. 2010, A&A, 512, A79

Haşegan, M., Jordán, A., Côté, P., et al. 2005, ApJ, 627, 203

Hainline, L. J., Blain, A. W., Smail, I., et al. 2011, ApJ, 740, 96

Harris, W. E. 1991, ARA&A, 29, 543

Harris, W. E. 1996, AJ, 112, 1487

Hau, G. K. T., Spitler, L. R., Forbes, D. A., et al. 2009, MNRAS, 394, L97

Hempel, M., Kissler-Patig, M., Puzia, T. H., & Hilker, M. 2007, A&A, 463, 493

Hickox, R. C., Wardlow, J. L., Smail, I., et al. 2012, MNRAS, 421, 284

Hilker, M. 2009a, in Reviews in Modern Astronomy, Vol. 21, Reviews in Modern Astronomy, ed. S. Röser, 199–213

Hilker, M. 2009b, UCDs - A Mixed Bag of Objects, ed. T. Richtler & S. Larsen, 51

Hilker, M., Baumgardt, H., Infante, L., et al. 2007, A&A, 463, 119

Hilker, M., Infante, L., & Richtler, T. 1999a, A&AS, 138, 55

Hilker, M., Infante, L., Vieira, G., Kissler-Patig, M., & Richtler, T. 1999b, A&AS, 134, 75

Hunter, D. A., Elmegreen, B. G., Dupuy, T. J., & Mortonson, M. 2003, AJ, 126, 1836

Hunter, D. A., Elmegreen, B. G., & Ludka, B. C. 2010, AJ, 139, 447

Iodice, E., Capaccioli, M., Grado, A., et al. 2016, ApJ, 820, 42

Iodice, E., Spavone, M., Capaccioli, M., et al. 2017, ApJ, 839, 21

Jones, J. B., Drinkwater, M. J., Jurek, R., et al. 2006, AJ, 131, 312

Jordán, A., Blakeslee, J. P., Côté, P., et al. 2007, ApJS, 169, 213

Jordán, A., Côté, P., Blakeslee, J. P., et al. 2005, ApJ, 634, 1002

Juneau, S., Glazebrook, K., Crampton, D., et al. 2005, ApJ, 619, L135

Khalaj, P. & Baumgardt, H. 2016, MNRAS, 457, 479

Kilerci Eser, E., Goto, T., & Doi, Y. 2014, ApJ, 797, 54

Kim, H.-S., Yoon, S.-J., Sohn, S. T., et al. 2013, ApJ, 763, 40

Kissler-Patig, M., Brodie, J. P., Schroder, L. L., et al. 1998, AJ, 115, 105

Kissler-Patig, M., Grillmair, C. J., Meylan, G., et al. 1999, AJ, 117, 1206

Kissler-Patig, M., Jordán, A., & Bastian, N. 2006, A&A, 448, 1031

Kissler-Patig, M., Kohle, S., Hilker, M., et al. 1997, A&A, 319, 470

Kormendy, J. 1989, ApJ, 342, L63

Kormendy, J. & Sanders, D. B. 1992, ApJ, 390, L53

Kravtsov, A. V. & Gnedin, O. Y. 2005, ApJ, 623, 650

Kriek, M., Conroy, C., van Dokkum, P. G., et al. 2016, Nature, 540, 248

Kroupa, P. 1998, MNRAS, 300, 200

Kroupa, P. 2001, MNRAS, 322, 231

Kroupa, P. 2015, Canadian Journal of Physics, 93, 169

Kroupa, P. & Boily, C. M. 2002, MNRAS, 336, 1188

Kroupa, P., Weidner, C., Pflamm-Altenburg, J., et al. 2013, The Stellar and Sub-Stellar Initial Mass Function of Simple and Composite Populations (Oswalt, T. D. and Gilmore, G.), 115

Kruijssen, J. M. D. 2014, Classical and Quantum Gravity, 31, 244006

Kuijken, K. 2011, The Messenger, 146, 8

Kundu, A., Zepf, S. E., Hempel, M., et al. 2005, ApJ, 634, L41

Lada, C. J. & Lada, E. A. 2003, ARA&A, 41, 57

Lamers, H. J. G. L. M., Baumgardt, H., & Gieles, M. 2010, MNRAS, 409, 305

Lamers, H. J. G. L. M., Baumgardt, H., & Gieles, M. 2013, MNRAS, 433, 1378

Lamers, H. J. G. L. M., Gieles, M., Bastian, N., et al. 2005a, A&A, 441, 117

Lamers, H. J. G. L. M., Gieles, M., & Portegies Zwart, S. F. 2005b, A&A, 429, 173

Larsen, S. S. 2002, AJ, 124, 1393

Larsen, S. S. 2009, A&A, 494, 539

Larsen, S. S., Brodie, J. P., & Strader, J. 2012a, A&A, 546, A53

Larsen, S. S., Strader, J., & Brodie, J. P. 2012b, A&A, 544, L14

Larson, R. B. 1975, MNRAS, 173, 671

Le Fèvre, O., Saisse, M., Mancini, D., et al. 2003, in Proc. SPIE, Vol. 4841, Instrument Design and Performance for Optical/Infrared Ground-based Telescopes, ed. M. Iye & A. F. M. Moorwood, 1670–1681

Le Floc'h, E., Papovich, C., Dole, H., et al. 2005, ApJ, 632, 169

Letarte, B., Hill, V., Jablonka, P., et al. 2006, A&A, 453, 547

Lilly, S. J., Eales, S. A., Gear, W. K. P., et al. 1999, ApJ, 518, 641

Linden, S. T., Evans, A. S., Rich, J., et al. 2017, ArXiv e-prints

Liu, C., Peng, E. W., Côté, P., et al. 2015a, ApJ, 812, 34

Liu, C., Peng, E. W., Jordán, A., et al. 2011, ApJ, 728, 116

Liu, C., Peng, E. W., Toloba, E., et al. 2015b, ApJ, 812, L2

Łokas, E. L. 2009, MNRAS, 394, L102

Longmore, S. N., Kruijssen, J. M. D., Bastian, N., et al. 2014, Protostars and Planets VI, 291

Lüghausen, F., Famaey, B., & Kroupa, P. 2015, Canadian Journal of Physics, 93, 232

Ma, J., Gonzalez, A. H., Vieira, J. D., et al. 2016, ApJ, 832, 114

Mackey, A. D. & Gilmore, G. F. 2003, MNRAS, 340, 175

Madau, P. & Dickinson, M. 2014, ARA&A, 52, 415

Madrid, J. P. 2011, ApJ, 737, L13

Madrid, J. P. & Donzelli, C. J. 2013, ApJ, 770, 158

Madrid, J. P., Graham, A. W., Harris, W. E., et al. 2010, ApJ, 722, 1707

Mancuso, C., Lapi, A., Shi, J., et al. 2016, ApJ, 823, 128

Maraston, C. 2005, MNRAS, 362, 799

Marks, M., Kroupa, P., Dabringhausen, J., & Pawlowski, M. S. 2012, MNRAS, 422, 2246

Marsan, Z. C., Marchesini, D., Brammer, G. B., et al. 2015, ApJ, 801, 133

Maschberger, T. & Kroupa, P. 2007, MNRAS, 379, 34

Masters, K. L., Jordán, A., Côté, P., et al. 2010, ApJ, 715, 1419

McCrady, N. & Graham, J. R. 2007, ApJ, 663, 844

Michałowski, M., Hjorth, J., & Watson, D. 2010, A&A, 514, A67

Michałowski, M. J., Dunlop, J. S., Koprowski, M. P., et al. 2017, MNRAS, 469, 492

Mieske, S., Frank, M. J., Baumgardt, H., et al. 2013, A&A, 558, A14

Mieske, S., Hilker, M., & Infante, L. 2002, A&A, 383, 823

Mieske, S., Hilker, M., & Infante, L. 2004, A&A, 418, 445

Mieske, S., Hilker, M., Infante, L., & Jordán, A. 2006, AJ, 131, 2442

Mieske, S., Hilker, M., Jordán, A., et al. 2008, A&A, 487, 921

Mieske, S., Hilker, M., & Misgeld, I. 2012, A&A, 537, A3

Mieske, S., Jordán, A., Côté, P., et al. 2010, ApJ, 710, 1672

Miller, T. B., Hayward, C. C., Chapman, S. C., & Behroozi, P. S. 2015, MNRAS, 452, 878

Minniti, D., Kissler-Patig, M., Goudfrooij, P., & Meylan, G. 1998, AJ, 115, 121

Misgeld, I. & Hilker, M. 2011, MNRAS, 414, 3699

Misgeld, I., Mieske, S., Hilker, M., et al. 2011, A&A, 531, A4

Mittal, R., McDonald, M., Whelan, J. T., & Bruzual, G. 2017, MNRAS, 465, 3143

Muñoz, R. P., Puzia, T. H., Lançon, A., et al. 2014, ApJS, 210, 4

Murray, N. 2009, ApJ, 691, 946

Murray, S. D. & Lin, D. N. C. 1992, ApJ, 400, 265

Narayanan, D. & Davé, R. 2013, MNRAS, 436, 2892

Narayanan, D., Turk, M., Feldmann, R., et al. 2015, Nature, 525, 496

Nardini, E., Risaliti, G., Watabe, Y., Salvati, M., & Sani, E. 2010, MNRAS, 405, 2505

Norris, M. A., Escudero, C. G., Faifer, F. R., et al. 2015, MNRAS, 451, 3615

Norris, M. A., Gebhardt, K., Sharples, R. M., et al. 2012, MNRAS, 421, 1485

Norris, M. A. & Kannappan, S. J. 2011, MNRAS, 414, 739

Okabe, N., Okura, Y., & Futamase, T. 2010, ApJ, 713, 291

Okazaki, T. & Tosa, M. 1995, MNRAS, 274, 48

Oke, J. B. & Gunn, J. E. 1983, ApJ, 266, 713

Ostrov, P., Geisler, D., & Forte, J. C. 1993, AJ, 105, 1762

Pacifici, C., Kassin, S. A., Weiner, B. J., et al. 2016, ApJ, 832, 79

Pedregosa, F., Varoquaux, G., Gramfort, A., et al. 2011, Journal of Machine Learning Research, 12, 2825

Peng, E. W., Côté, P., Jordán, A., et al. 2006, ApJ, 639, 838

Penny, S. J., Forbes, D. A., & Conselice, C. J. 2012, MNRAS, 422, 885

Penny, S. J., Forbes, D. A., Strader, J., et al. 2014, MNRAS, 439, 3808

Pfeffer, J. & Baumgardt, H. 2013, MNRAS, 433, 1997

Pfeffer, J., Griffen, B. F., Baumgardt, H., & Hilker, M. 2014, MNRAS, 444, 3670

Pfeffer, J., Hilker, M., Baumgardt, H., & Griffen, B. F. 2016, MNRAS, 458, 2492

Pflamm-Altenburg, J., González-Lópezlira, R. A., & Kroupa, P. 2013, MNRAS, 435, 2604

Pflamm-Altenburg, J. & Kroupa, P. 2006, MNRAS, 373, 295

Pflamm-Altenburg, J. & Kroupa, P. 2009, MNRAS, 397, 488

Phillipps, S., Drinkwater, M. J., Gregg, M. D., & Jones, J. B. 2001, ApJ, 560, 201

Planck Collaboration, Ade, P. A. R., Aghanim, N., et al. 2014, A&A, 571, A1

Portegies Zwart, S. F., Hut, P., Makino, J., & McMillan, S. L. W. 1998, A&A, 337, 363

Portegies Zwart, S. F., Makino, J., McMillan, S. L. W., & Hut, P. 2002, ApJ, 565, 265

Puzia, T. H., Kissler-Patig, M., Thomas, D., et al. 2005, A&A, 439, 997

Puzia, T. H., Paolillo, M., Goudfrooij, P., et al. 2014, ApJ, 786, 78

Randriamanakoto, Z., Escala, A., Väisänen, P., et al. 2013, ApJ, 775, L38

Recchi, S., Calura, F., & Kroupa, P. 2009, A&A, 499, 711

Richtler, T. 2006, Bulletin of the Astronomical Society of India, 34, 83

Richtler, T., Dirsch, B., Gebhardt, K., et al. 2004, AJ, 127, 2094

Richtler, T., Dirsch, B., Larsen, S., Hilker, M., & Infante, L. 2005, A&A, 439, 533

Richtler, T., Grebel, E. K., Domgoergen, H., Hilker, M., & Kissler, M. 1992, A&A, 264, 25

Richtler, T., Schuberth, Y., Hilker, M., et al. 2008, A&A, 478, L23

Riechers, D. A., Bradford, C. M., Clements, D. L., et al. 2013, Nature, 496, 329

Riechers, D. A., Leung, T. K. D., Ivison, R. J., et al. 2017, ArXiv e-prints

Rosenberg, J. L., Wu, Y., Le Floc'h, E., et al. 2008, ApJ, 674, 814

Rosolowsky, E., Keto, E., Matsushita, S., & Willner, S. P. 2007, ApJ, 661, 830

Rossa, J. & Dettmar, R.-J. 2003, A&A, 406, 493

Rowan-Robinson, M. 2000, MNRAS, 316, 885

Ruiz, A., Risaliti, G., Nardini, E., Panessa, F., & Carrera, F. J. 2013, A&A, 549, A125

Saglia, R. P., Kronawitter, A., Gerhard, O., & Bender, R. 2000, AJ, 119, 153

Sargsyan, L. A. & Weedman, D. W. 2009, ApJ, 701, 1398

Schiminovich, D., Ilbert, O., Arnouts, S., et al. 2005, ApJ, 619, L47

Schuberth, Y., Richtler, T., Hilker, M., et al. 2010, A&A, 513, A52

Schulz, C., Hilker, M., Kroupa, P., & Pflamm-Altenburg, J. 2016, A&A, 594, A119

Schulz, C., Pflamm-Altenburg, J., & Kroupa, P. 2015, A&A, 582, A93

Seth, A. C., van den Bosch, R., Mieske, S., et al. 2014, Nature, 513, 398

Simpson, J. M., Smail, I., Swinbank, A. M., et al. 2015, ApJ, 807, 128

Speagle, J. S., Steinhardt, C. L., Capak, P. L., & Silverman, J. D. 2014, ApJS, 214, 15

Strader, J., Seth, A. C., Forbes, D. A., et al. 2013, ApJ, 775, L6

Swinbank, A. M., Chapman, S. C., Smail, I., et al. 2006, MNRAS, 371, 465

Swinbank, A. M., Simpson, J. M., Smail, I., et al. 2014, MNRAS, 438, 1267

Takata, T., Sekiguchi, K., Smail, I., et al. 2006, ApJ, 651, 713

Tal, T., van Dokkum, P. G., Nelan, J., & Bezanson, R. 2009, AJ, 138, 1417

Tamburro, D., Rix, H.-W., Walter, F., et al. 2008, AJ, 136, 2872

Thomas, D., Greggio, L., & Bender, R. 1999, MNRAS, 302, 537

Thomas, P. A., Drinkwater, M. J., & Evstigneeva, E. 2008, MNRAS, 389, 102

Trager, S. C., Faber, S. M., Worthey, G., & González, J. J. 2000, AJ, 120, 165

Veilleux, S., Kim, D.-C., & Sanders, D. B. 1999, ApJ, 522, 113

Voggel, K., Hilker, M., & Richtler, T. 2016, A&A, 586, A102

Wang, L., Farrah, D., Oliver, S. J., et al. 2013, MNRAS, 431, 648

Wehner, E. M. H. & Harris, W. E. 2007, ApJ, 668, L35

Weidner, C., Bonnell, I. A., & Zinnecker, H. 2010, ApJ, 724, 1503

Weidner, C., Kroupa, P., & Larsen, S. S. 2004, MNRAS, 350, 1503

Weidner, C., Kroupa, P., & Pflamm-Altenburg, J. 2011, MNRAS, 412, 979

Whitmore, B. C., Chandar, R., & Fall, S. M. 2007, AJ, 133, 1067

Whitmore, B. C., Chandar, R., Schweizer, F., et al. 2010, AJ, 140, 75

Wittmann, C., Lisker, T., Pasquali, A., Hilker, M., & Grebel, E. K. 2016, MNRAS, 459, 4450

Yamaguchi, R., Mizuno, N., Mizuno, A., et al. 2001, PASJ, 53, 985

Yoon, S.-J., Yi, S. K., & Lee, Y.-W. 2006, Science, 311, 1129

Zhang, Q. & Fall, S. M. 1999, ApJ, 527, L81

Acknowledgments

First of all, I would like to thank my adviser, Michael Hilker, for encouraging me to apply for a PhD position at ESO and afterward, for being a supportive mentor during the last three years. You were always available to give me advice or for an useful discussion and provided me with the freedom to develop my own ideas. Special thanks to Andreas Burkert for many interesting discussions and the supervision of this thesis.

Thank you to all my colleagues at ESO and IMPRS, especially our lunch group, who quickly became close friends after various dinners, cocktail parties, and hikes. I hope that some of you will stay in Munich. Many thanks to my previous and current office mates, I had an incredible time with you! The fun we had in 4.24 manifested itself in the unique decorations which will hopefully be as inspirational to the coming generations of astronomers as they were for us. Also, sorry to all the neighbors we distracted from work while thinking about new quirks for the party office....

Last, and most importantly, I would like to wholeheartedly say thank you to my family and my closest friends. Without your support and encouragement my achievements would not have been possible. Ganz lieben Dank!